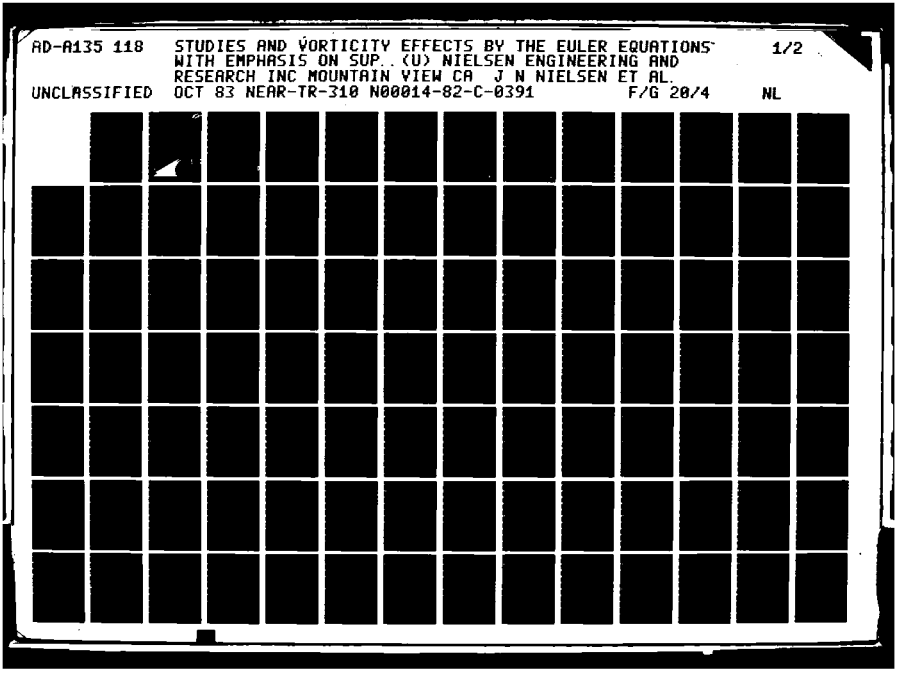
AD-A135 118 STUDIES AND VORTICITY EFFECTS BY THE EULER EQUATIONS WITH EMPHASIS ON SUP..(U) NIELSEN ENGINEERING AND RESEARCH INC MOUNTAIN VIEW CA J N NIELSEN ET AL.
1/2
UNCLASSIFIED OCT 83 NEAR-TR-310 N00014-82-C-0391 F/G 20/4 NL

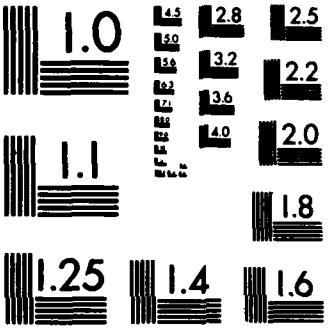

AD-A135 118

STUDIES OF VORTICITY EFFECTS BY THE EULER EQUATIONS WITH EMPHASIS ON SUPERSONIC FLOW FIELDS

by

J. N. Nielsen and G. D. Kuhn

NIELSEN ENGINEERING
AND RESEARCH, INC.

OFFICES: 510 CLYDE AVENUE / MOUNTAIN VIEW, CALIFORNIA 94043 / TELEPHONE (415) 968-9457

(12)

STUDIES OF VORTICITY EFFECTS BY THE EULER EQUATIONS WITH EMPHASIS ON SUPERSONIC FLOW FIELDS

by

J. N. Nielsen and G. D. Kuhn

NEAR TR 310
October 1983

Prepared Under Contract No. N00014-82-C-0391

for

OFFICE OF NAVAL RESEARCH
Arlington, VA 22217

by

NIELSEN ENGINEERING & RESEARCH, INC.
510 Clyde Avenue, Mountain View, CA 94043
Telephone (415) 968-9457

UNCLASSIFIED

SECURITY CLASSIFICATION OF THIS PAGE (When Data Entered)

REPORT DOCUMENTATION PAGE	READ INSTRUCTIONS BEFORE COMPLETING FORM
1. REPORT NUMBER	2. GOVT ACCESSION NO. AD-A135118 / 3. RECIPIENT'S CATALOG NUMBER
4. TITLE (and Subtitle) Studies and Vorticity Effects by the Euler Equations with Emphasis on Supersonic Flow Fields	5. TYPE OF REPORT & PERIOD COVERED Final Report 6. PERFORMING ORG. REPORT NUMBER NEAR TR 310
7. AUTHOR(s) J. N. Nielsen and G. D. Kuhn	8. CONTRACT OR GRANT NUMBER(s) N00014-82-C-0391
9. PERFORMING ORGANIZATION NAME AND ADDRESS Nielsen Engineering & Research, Inc. 510 Clyde Avenue Mountain View, CA 94043	10. PROGRAM ELEMENT, PROJECT, TASK AREA & WORK UNIT NUMBERS
11. CONTROLLING OFFICE NAME AND ADDRESS Office of Naval Research Department of the Navy Arlington, VA 22217	12. REPORT DATE October 1983 13. NUMBER OF PAGES 115
14. MONITORING AGENCY NAME & ADDRESS (if different from Controlling Office)	15. SECURITY CLASS. (of this report) Unclassified 15a. DECLASSIFICATION/DOWNGRADING SCHEDULE

16. DISTRIBUTION STATEMENT (of this Report)

Approved for public release;
Distribution unlimited.

17. DISTRIBUTION STATEMENT (of the abstract entered in Block 20, if different from Report)

18. SUPPLEMENTARY NOTES

19. KEY WORDS (Continue on reverse side if necessary and identify by block number)

Euler Equations
Supersonic Flow
Missile Aerodynamics
Cruciform Missiles
Wakes
Flow Fields

20. ABSTRACT (Continue on reverse side if necessary and identify by block number)

The primary purpose of the present report is to demonstrate how well the Euler equations in a supersonic marching program (SWINT) can predict the flow fields of bodies, wings, and wing-body combinations. The motivation was to see if the Euler equations will predict the fin loads in highly vortical flow fields for cruciform missiles. Body-alone and wing-body flow fields were measured in the Bumblebee Program at a position where a tail might be placed.

(Continued reverse side)

DD FORM 1 JAN 73 1473 EDITION OF 1 NOV 65 IS OBSOLETE

UNCLASSIFIED

SECURITY CLASSIFICATION OF THIS PAGE (When Data Entered)

(block 20 continued)

cont

Those data, compared with the predictions of the Euler code, showed problems in both data and predictions. The data sometimes exhibited lack of repeatability which prevented critical comparison of data and theory in many instances. Also the lack of a sufficient number of nodes in the reverse flow regions of the flow made it difficult to get good predictions in this area. Some improvements were obtained by clustering. Generally the flow quantities on the windward side of the body and wing-body were predicted and measured more accurately than on the leeward side of the body.

Study of a rectangular wing model of AR = 2 at M_∞ = 2.86 showed that both the Euler code and a supersonic panel method modified for nonlinearities by shock-expansion theory predicted the measured pressure distribution well. Computer studies of the flow field behind the wing showed that wing thickness effects had only a small effect on the calculated flow field. Also, imposition of a Kutta condition at the wing side edge had a small effect on the calculated flow field. This is attributed to the fact that the Euler code imposes a pseudo Kutta condition of its own since vorticity is shed from the side edge in the calculation. It was, however, essential to include a Kutta-like condition on the body at its primary separation line.

A calculative example of a wing-body-tail was carried out using the Euler code wherein strong canard vortex effects on the tail were present. No data to verify the calculation are available.

SUMMARY

The primary purpose of the present report is to demonstrate how well the Euler equations in a supersonic marching program (SWINT) can predict the flow fields of bodies, wings, and wing-body combinations. The motivation is to see if the Euler equations will predict the fin loads in highly vortical flow fields for cruciform missiles. Body-alone and wing-body flow fields were measured in the Bumblebee Program at a position where a tail might be placed. Those data, compared with the predictions of the Euler code, showed problems in both data and predictions. The data sometimes exhibited lack of repeatability which prevented critical comparison of data and theory in many instances. Also the lack of a sufficient number of nodes in the reverse flow regions of the flow made it difficult to get good predictions in this area. Some improvements were obtained by clustering. Generally the flow quantities on the windward side of the body and wing-body were predicted and measured more accurately than on the leeward side of the body.

Study of a rectangular wing model of AR = 2 at M_∞ = 2.86 showed that both the Euler code and a supersonic panel method modified for nonlinearities by shock-expansion theory predicted and measured pressure distribution well. Computer studies of the flow field behind the wing showed that wing thickness effects had only a small effect on the calculated flow field. Also, imposition of a Kutta condition at the wing side edge had a small effect on the calculated flow field. This is attributed to the fact that the Euler code imposes a pseudo Kutta condition of its own since vorticity is shed from the side edge in the calculation. It was, however, essential to include a Kutta-like condition on the body at its primary separation line.

A calculative example of a wing-body-tail was carried out using the Euler code wherein strong canard vortex effects on the tail were present. No data to verify the calculation are available.

TABLE OF CONTENTS

1. INTRODUCTION

For the past several years, Nielsen Engineering & Research, Inc. (NEAR) has been engaged in studying means of incorporating vortex effects into the Euler equations so that a prediction method for handling both compressibility and viscous effects can be developed without recourse to the more complicated Navier-Stokes equations. This approach is based on the knowledge that many high angle of attack vortical phenomena encountered by missiles and airplanes are dominated by convection rather than diffusion of vorticity. The work has significance in several ways. First, the feasibility of using Euler codes for complete vehicles is of interest in itself since problems of missiles and airplanes at high angles of attack can now be treated only by approximate engineering methods. Secondly, such Euler codes can provide bench-mark cases for evaluating the approximate engineering methods now used in the preliminary design of airplanes and missiles.

The compressibility nonlinearities associated with shock waves and expansions are well-handled by the Euler equations in their capturing mode, but the viscous nonlinearities require special treatment. The viscous nonlinearties of interest include:

a. Vortex formation at subsonic leading edges and side edges of wings and fins.

b. Separation of symmetrical body vortices at moderate to high angles of attack ($\alpha \geq 10°$).

c. Interactions of fins with vortices.

The results of investigations for items a, b, and c have been published in References 1-3, respectively.

Each of the investigations described in References 1-3 has examined a particular aspect of the problem of introducing viscous effects into the Euler code. For application of a supersonic marching Euler code to complete configurations, such as a wing-body-tail combination, further investigation and verification is needed. In particular, the rolling up of fin vortices, their interaction with the afterbody vortices, and their subsequent effect on the empennage need to be investigated. This area is the subject of the present report. In addition, results of investigation of the strong interaction between a vortex and a fin as occurs when the vortex passes close to or is bisected by the fin itself are presented.

2. PREVIOUS WORK

The previous work accomplished under ONR Contract N00014-78-C-0490 reported in References 1, 2, and 3 will now be reviewed since this work has bearing on the presently reported research.

In Reference 1 the general treatment of the Euler equations with separation at a sharp subsonic leading edge was developed including the application of the Kutta condition to the leading edge. As an application of the theory, the pressure loading was calculated on an $AR = 1$ delta wing at $M_\infty = 2.86$ and $\alpha = 10°$. No wing thickness effects were included. The pressure loading, the difference in pressure coefficient between lower and upper surfaces, was compared with data taken from Reference 4. The agreement was quite good. The method was then applied to a special delta wing-body combination with rounded wing-body junctures on both surfaces to avoid singularities at these points. No data were available for comparing pressure loadings on the wing, but the overall fin normal force exhibited large adverse effects of wing-body interference shown by fins of the same planform ($AR = 1$) but without faired wing-body junctures.

The second year of work reported in Reference 2 was concerned principally with separated flow over bodies of revolution. The Kutta condition for a sharp subsonic leading edge was modified to apply to a specified primary separation line on a body of revolution. Five conditions must be specified. A parametric study of these conditions showed that the separation location is the principal condition, and the separated flow is insensitive to the other conditions. The Euler code with the body of revolution Kutta condition was applied to an ogive-nose cylinder for which data were available for $M_\infty = 3.0$ and $\alpha = 15°$ for the flow field. Comparisons between the predicted and measured flow fields showed generally good agreement except above the body where the upwash was overpredicted. It is thought this result may be due to the neglect of secondary separation. The predicted circulation about an experimental contour containing most of the vorticity compared well with the data.

In the third year's work, several tasks were undertaken. First, the locations of the primary separation lines on cones and cylinders at high angles of attack were correlated as a function of cone half-angle, angle of attack, and free-stream Mach number. These correlations provide data for specifying the positions of separation lines which are required in using the Kutta condition.

The Euler equations were applied to a cone at high angle of attack, above the half angle, using the Kutta condition, and the predicted pressure distributions compared well with the measured pressure distribution on the cone.

A second calculative example was run of a wing-body combination consisting of a cone of length 3D, a cylindrical afterbody of length 5D, and a winged section of length 2D with an aspect ratio 2 delta wing. The conditions were $M_\infty = 3.0$ and $\alpha = 25°$. The pressure distribution on the cone and cylinder compared well with data. Since only primary separation was included in the model, it is clear that secondary separation need not be

taken into account to obtain good body loading distributions. Calculations were made for $M_\infty = 3.0$ and $\alpha = 10°$ with no wing thickness, and no body Kutta-condition applied over the winged part of the configuration. However, the body separation lines over the winged section were found in the calculative solution as a result of the persistence of vorticity. Comparisons were made between the vortex induced velocity normal to the fins as calculated from the Euler solution and from the Biot-Savart law with the Euler solution giving slightly more downwash. Using the downwash distribution due to the Euler solution, a supersonic panel method (Ref. 5) was used to calculate the fin pressure distribution associated with the vorticity. Fair agreement was obtained between this quantity and that for the Euler solution except in the wing-body juncture.

3. OUTLINE OF RESULTS OF PRESENT WORK

3.1 Preliminary Considerations

A primary purpose of the work presented herein is to evaluate the ability of the Euler equations to predict the flow fields behind wings and fins of a wing-body combination. If such predictions can be made with engineering accuracy, then the interference on the empennage of the body and forward lifting surfaces can be calculated. The Euler code can then be applied to wing-body-tail combinations.

There are few data available which are suitable for checking the ability of the Euler equations to predict wing-body flow fields. It is important that any data be for a combination which does not produce pockets of subsonic flow parallel to the body axis, otherwise the supersonic marching code being used fails. For the set of data used herein, it was necessary to eliminate wing thickness effects on downwash for this reason. A check was made on the importance of thickness

on the downstream flow field using a rectangular wing at $M_\infty = 2.86$. The effect of the Kutta condition at the side edge on the flow field was also investigated.

3.2 Rectangular Wing Alone

While no flow-field data behind a rectangular wing alone were avilable, such data were available for a rectangular wing-body combination (Refs. 6-9). Pressure distributions were obtained for a rectangular wing alone. They will be discussed in Section 4 prior to discussing the wing-body combination. The wing-alone case provides an opportunity to study the effec of wing thickness and the Kutta condition on the wing wake. In addition, pressure distributions will be compared as calcul by the Euler equations and by a supersonic panel method (Ref. . The wing alone given in Figure 1 is an $AR = 2$ rectangular wing for which pressure distributions are given in Reference 4.

3.3 Rectangular Wing and Body Combinations

The rectangular wing and body combination (Fig. 13) for which data are available (Refs. 6-9) has a body consisting of a 15° half-angle cone followed by 4.70 diameters of cylindrical body. An aspect ratio 2 wing is mounted on the cylindrical body with a radius/semispan ratio of .255. The survey station is 2.92 body diameters behind the wing trailing edge. Comparisons will be made in Section 5 between the data and Euler code predictions for local Mach number, local dynamic pressure, and local angle of attack normal to a fin at various roll orientations. These are the basic data needed to perform a strip theory integration to obtain fin normal force.

3.4 Body-Canard Combinations with Interdigitated Tails

This example is an hypothetical case for which no data are available. It is presented to illustrate the application of the Euler code for a zero roll case and to study a vortex field in close proximity to the tail fins. The horizontal canard fins develop strong vortices which tend to rise above the body. The interdigitated tail fins were placed close to the angular position of the canard vortices in the survey plane. In this way the tail fins are subject to interference from vortices in close proximity.

4. RECTANGULAR WING EXAMPLE

4.1 Preliminary Considerations

The example rectangular wing taken from Reference 4 has an aspect ratio of 2 and is shown in Figure 1. All edges are beveled with 15° half angles normal to the edges. The calculations will be made for a Mach number of 2.86 and an angle of attack of 10°. The shock detachment angle is about 33° for $M_\infty = 2.86$. The leading-edge shock is attached in the Euler solution at $\alpha = 10°$ since the wedge angle of 15° produces a local angle of attack change of 25° at the leading edge.

The calculations were made using the Euler code of Reference 10. Calculations extending into the wake region were made with and without the Kutta-condition and with and without wing thickness to investigate the influence of these parameters on the wake velocity profiles. Also, some calculations were made with program LRCDM, a supersonic paneling program, for comparison with the Euler results and with data.

With regard to the initial conditions, a special procedure was required to start the calculations for the wing alone because the grid system of the computer program is a polar system. Such a system centered on the root chord would have a singularity there. The flow was started by considering a large, rectangular, hollow fuselage aligned with the flow which acts as a reflection plane.* The grid system used was a nonorthogonal polar system centered on the fuselage longitudinal axis with unequal angular increments clustered about the wing plane and with variable radial increments. See Figure 2. The

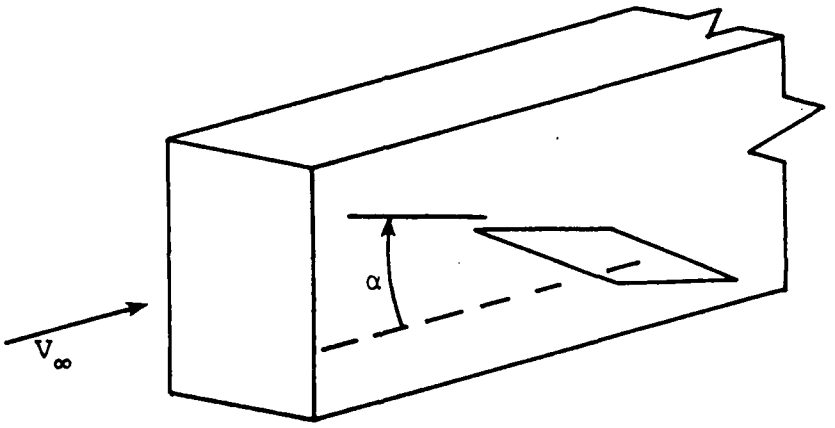

radial spacing was one-thirtieth of the distance between the fuselage and a circular boundary containing it. The wing boundary conditions were applied in the wing chord plane.

Consider the nodal points along the radial line on which the wing boundary conditions are specified. Let n be the index of the nodal point on the wing closest to the wing tip. (Generally the wing tip is not a nodal point.) A

*We are indebted to the authors of Reference 10 for this idea.

predictor-corrector relationship was used to determine the pressure and density at point n as follows:

$$\left.\begin{aligned} p_n(n) &= \tfrac{1}{2}\,[p(n-1) + p_p(n)] \\ \rho_n(n) &= \tfrac{1}{2}\,[\rho(n-1) + \rho_p(n)] \end{aligned}\right\} \qquad (1)$$

p_p, ρ_p = predicted values

p_n, ρ_n = new value

The fluid velocity V_n follows from p_n and ρ_n. Let θ_n be the flow angle at node n interpolated between the leading-edge angle and the flow angle in the plane of the wing at n - 1. Then the velocity components at node n are given by

$$\left.\begin{aligned} u_n &= V_n \sin\theta_n; \text{ radial speed} \\ v_n &= 0; \text{ circumferential speed} \\ w_n &= V_n \cos\theta_n; \text{ axial speed} \end{aligned}\right\} \qquad (2)$$

The essential condition is that $v_n = 0$ at the wing tip.

4.2 Pressure Distribution Comparisons

It is of interest to examine how well the Euler code predicts the pressure distribution on a rectangular wing in order to interpret the ability of the Euler code to predict the wake properties. For instance, the span loading affects the initial distribution of vorticity leaving the trailing edge of the wing panel, and this loading depends in turn on the accuracy of the pressure distribution predictions. Thus, pressure distributions, span loading, and wake properties will be examined in that order.

The first comparisons to be discussed are concerned with pressure distribution data as measured and as calculated by a panel code corrected for the difference between supersonic linear theory and shock-expansion theory since these results illustrate certain physical phenomena. The panel method and its nonlinear shock-expansion correction procedure are described in Reference 11 on which figure 3 is based. Comparisons are made between prediction and experiment for a chordwise strip near the midspan [Fig. 3(a)] and a spanwise strip at the mid-chord [Fig. 3(b)].

Examining first the comparison for the near midspan position, $y/s = 0.53$, it is seen that the pressure coefficients on the leading wedges and the midsection are well predicted by the theory. With regard to the lower surface, the pressure falls going from the midsection to the trailing wedge, undergoing a considerable expansion which is fairly well predicted. The shoulder of the trailing wedge has some small forward influence onto the midsection which should be at constant pressure. The flow on the top surface going onto the trailing wedge shows little or no change in pressure coefficient even though an expansion is predicted. Clearly, the flow has separated at the shoulder. Near the trailing edge an oblique shock must straighten out the flow nearly parallel to the free-stream direction, but no evidence of this shock appears in the data which goes up to the 0.95 chord position. The separation will affect the span loading and thereby the wake downwash and sidewash.

Next, the comparison between prediction and experiment for the spanwise pressure distribution acting at the midchord station as shown in Figure 3(b) is examined. The pressures do not vary significantly with spanwise distance until about the 65 percent semispan location. Near the wing tip on the top surface more suction pressure is predicted than

measured. On the bottom surface more positive pressure is predicted than measured. Also, the influence of the wing tip extends more inboard than predicted. This is probably the result of the difference between a tip Mach cone based on $M_\infty = 2.86$ in the predictions and one based on a lower Mach number in the data. The point is, however, that the span loading predicted on the tip is greater than that measured, a fact that can influence the trailing vorticity.

Next, the measured pressure coefficients are compared with those predicted by the Euler code. First, the chordwise pressure distributions at $y/s = 0.53$ for $M_\infty = 2.86$ and $\alpha = 10°$ are examined (Fig. 4). In the Euler code no Kutta condition was introduced. A grid of 31×31 was used. Separation is seen again at the shoulder of the trailing-edge wedge, but is not accounted for in the Euler code. It could be accounted for by assuming the flow separates parallel to the midsection and alters the effective wing thickness distribution. The Euler code exhibits uniform pressure on the leading-edge wedge. The slightly falling pressure on the midsection is predicted by the Euler equations.

Turning now to comparison of experiment and prediction for the pressure coefficients measured along the midchord line, Figure 5 presents the comparisons. The pressure distribution on the lower surface is well-predicted except near the wing tip where the Euler code underpredicts the pressure by a considerable amount. The pressure distribution on the upper surface is predicted fairly well inboard but predicts too much suction pressure at the wing tip. If this behavior is typical of other constant chordline positions, the span loading at the wing tip would be overpredicted by the Euler code. The basic behavior of the Euler code at the wing tip is the result of the way in which the code handles the vortex shed by the sharp wing tip. Imposing a Kutta condition at the wing tip will ensure shedding of the vorticity at the tip. What the Euler code really does

at a subsonic edge without a Kutta condition is not clear, although there is evidence it yields some vortex shedding there.

To investigate the effect of imposing the Kutta condition at the tip, the calculations were re-run with the conditions specified in Equations (1) and (2). Figure 6 compares the midchord pressure distributions on the outer half of the wing calculated with and without the Kutta condition imposed. The Kutta condition does not affect the comparison between experiment and prediction on the windward side, but improves it on the leeward side. The difference between the two solutions does not represent the difference due to a true Kutta condition since, as noted above, the Euler code without a Kutta condition imposed a quasi-Kutta condition of its own.

4.3 Span Loading Comparisons

In classical lifting-line theory (Ref. 12) the span-loading distribution, $cc_n(y)$, gives the distribution of trailing vorticity at the wing trailing edge. The local trailing vortex strength is given by $d/(cc_n)/dy$. Thus, anything that infuences the span-loading distribution will influence the wake downwash and sidewash. For this reason the various span loading predictions are compared with the data. The first comparison is of the span loadings obtained by experiment and calculated by the nonlinear panel code as shown in Figure 7. While the results on the inboard stations compare favorably, the results near the wing tip show that the panel method predicts too much wing-tip loading.

With respect to the span loading calculated by the Euler code two cases must be distinguished; one with the Kutta condition and one without it. In Figure 8 the comparisons are made between the data and the Euler code predictions. It is seen that the Euler code gives better agreement with the data than the nonlinear panel method. The difference between the span

loadings with and without the Kutta condition is not large and should not be significant in the wake calculations.

Another factor in span loading, which is of some interest, is the effect of wing thickness on the span-loading distribution. For the rectangular wing, which has a half-wedge angle at the leading edge, side edge, and trailing edge of 15 degrees, it might be expected that some span loading effect is due to wing thickness. The Euler code was used to determine the spanwise distributions of c_n for the rectangular wing with and without thickness. These distributions are compared with the experimental distribution (shown as a curve) in Figure 9. Over the inboard stations of the wing, which are uninfluenced by the wing tip, a significant reduction in normal-force coefficient occurs for the no-thickness case. Application of shock-expansion theory to the thickness and no-thickness cases clearly indicates the reason for this difference. At $\alpha = 10°$ with no thickness the shock deflection angle on the lower surface is 10° but with thickness it is 25°. The more than linear increase in pressure coefficient with shock deflection angle causes a large increase in the contribution of the front wedge section to the local normal-force coefficient compared to the no thickness case. Omitting wing thickness at the tip causes an increase in the tip normal-force coefficient as calculated by the Euler code using a Kutta condition. It appears that neglecting thickness in the Euler code modifies the wing span loading and thus may influence the calculated wake flow field. A direct evaluation of this effect will be shown in the following section.

The only reason to neglect the wing thickness distribution in the wing flow-field calculation is if the leading-edge wedge angle causes shock detachment so that calculation by

supersonic marching is no longer possible. The data for the flow field behind the wing of a wing-body combination, with which the Euler code predictions will be compared in a subsequent section, falls into this category.

4.4 Comparisons of Flow Angles in the Wake

In order to determine how wing thickness and the Kutta condition influence the flow angles in the wake, a series of Euler code calculations were made for the rectangular wing of aspect ratio 2 at $M_\infty = 2.86$ and 10° angle of attack. The flow angle convention in the Euler code is illustrated in Figure 10. The calculations were made for a half-model mounted on a hollow rectangular fuselage aligned with the flow so as to produce no disturbance velocities except for reflections of the wing waves from the corners of the fuselage. The flow-field calculations cover an area generally unaffected by the presence of the fuselage. The flow is calculated in a plane normal to the extended chord plane at three chord lengths behind the trailing edge. In this plane a polar coordinate system (R,ϕ) is set up around the fuselage centerline. The flow is calculated external to the fuselage whose vertical wall is a distance 20.0 units from the centerline and extends vertically outside the region of influence of the wing. The velocity components in the Z, R, and ϕ direction are designated as W, U, and V, respectively. The flow angle normal to the radius vector is designated α_f and that radially outward along the radius vector is designated β_f. Thus,

$$\alpha_f = \arctan\ (V/W) \tag{3}$$

$$\beta_f = \arctan\ (U/W) \tag{4}$$

It is noted that β_f is not zero on the vertical wall of the fuselage which represents the vertical plane of symmetry of the wing.

Values of α_f and β_f on the extended chord plane of the wing are given in Figure 11(a). The value of R at the root chord is 20 and at the wing tip it is 30.78. The effects of the Kutta condition on the flow angles for no thickness, are minor, while the effects with thickness are somewhat greater. The difference in α_f can be as large as 0.5° or slightly larger. The effects on β_f are generally much less. Thus, it appears that the imposition of the Kutta condition does not change the flow angles significantly either with or without thickness. A similar conclusion is reached regarding the effect of thickness on the calculated flow angles. It appears that the effect of thickness on β_f is generally much less than 1.0°. In a few cases the effect of thickness on β_f exceeds 1° slightly. Thus, the effect of thickness is not large on α_f or β_f.

The second region considered is the vertical plane of symmetry for which the results are shown in Figure 11(b). The leading-edge Mach wave is at a distance Y = 25 above the extended chord plane (Y = 0) and the leading-edge shock wave with no thickness is at Y = -17. Examination of the no-thickness results show no effect of the Kutta condition on the flow angles. The maximum effect of the Kutta condition on the flow angles with wing thickness is about 0.5° for α_f and 0.2° for β_f. Thus, the effect of the Kutta condition on the calculated flow angles on the vertical plane of symmetry is small.

Comparing the thickness and no thickness cases with the Kutta condition reveals that differences in α_f of 1° - 2° occur on the windward plane of symmetry and differences of about 1° or less occur on the leeward plane of symmetry; the values with thickness being generally of greater magnitude than those for no thickness. For the windward side the difference in β_f are as great as 1° or more, while for the leeward side the differences are 0.1° to 0.2°. It appears that the stronger

pressure disturbances on the shock side of the wing cause greater effects of thickness on α_f and β_f than the weaker disturbances cause on the leeward side of the wing.

While the previous discussion has noted small effects of wing thickness and the Kutta condition on the wing flow field on the extended chord plane and on the vertical plane of symmetry, the question arises whether the effects of these parameters are negligible in the neighborhood of the vortex. Accordingly, the results were examined for a radial trace through the vortex center. Figure 12 shows a machine generated plot of the flow 3 chord lengths behind the trailing edge of the AR = 2 rectangular wing. In order to bring out the vortex formation, $V_\infty \sin\alpha$ has been subtracted out of the vertical velocities. The root chord is at R = 20 and the wing tip is at R = 30.78. The vortex is nearly directly above the wing tip lateral position. A radial line of the computational mesh at ϕ = 100.2° goes approximatley through the vortex center and the vortex center lies near R = 31 to 32.

Figure 11(c) gives the values of α_f and β_f for the four cases being considered. It is clear from the figure that generally the effects of wing thickness and the Kutta condition on the calculated value of α_f and β_f are small. The maximum differences exceed 1° but are less than 2°.

5. EXAMPLE BODY AND RECTANGULAR WING COMBINATION

5.1 Preliminary Considerations

Data are avilable on the local flow fields for a rectangular wing-body combination and for its component body from measurements made under the Bumblebee Program, References 6 through 9. The data provide a means for evaluating the accuracy of an Euler code in predicting the local flow field

behind a wing-body combination in a position where an empennage might be located. The local flow field data included angles of attack and sidewash, dynamic pressure, Mach number, and total pressure.

Basically, the local flow field quantities which determine the normal force on the fin mounted on the body are the local Mach number, dynamic pressure, and flow angle in a plane normal to the fin chord plane. These are the basic quantities for which comparisons are made between data and the predictions of the Euler code.

The flow field at a possible tail location behind the fins of a wing-body combination is influenced by both the body and the wing. At an angle of attack of 16° a body will generally exhibit symmetric vortex separation so that the flow field at the tail position will be influenced by body vortices. Also, the fins of the wing will shed additional vortices which will interact with those due to the body. The fins may also change the flow separation characteristics of the body section behind the wing compared to what they may have been without the wing present. The body vortices up to the wing position will be unchanged by the presence of the wing, but may be altered in strength and position as they pass over the wing. The Euler code accounts for all these vortex effects by imposing the Kutta condition at specified primary separation locations on the body and fins. The wing-body combination will now be described preparatory to specifying the lines of primary separation.

The rectangular wing-body combination for which the comparisons are made is shown in Figure 13 as taken from Reference 6. The flow surveys for the complete configurations were made at station 3, two chord lengths behind the wing trailing edge. Calculations without the vertical fins present will be presented. Note that the wing section is a

biconvex airfoil 10 percent thick. The leading-edge semiwedge angle is 11.3° which, when added to an angle of attack of 16°, produces a total deflection angle of the flow at the leading edge on the lower surface of 27.3°. This angle exceeds the shock detachment angle for two-dimensional wedges of 23° at $M_\infty = 2.0$. Accordingly, the Euler code will not march since the flow is subsonic behind a detached, unswept, leading-edge shock. For this reason the Euler code was applied to the combination with a rectangular wing of no thickness. As shown in the previous section, thickness did not significantly change the flow field behind the wing alone of Reference 4.* Even though the airfoil section of the present fin is different from that of the wing in the previous section, it is assumed that wing thickness distribution will not significantly affect the calculated flow field in the wake. Turning now to the wing-body combination, it will be noted that the upwash angle calculated near the wing-body juncture will not exceed the shock detachment angle so that the wing with no thickness does not detach the leading-edge shock wave at $\alpha = 16°$. However, the data at station 3 show upwash angles slightly in excess of the shock detachment angle but the excess is within the accuracy of the local angle of attack measurements.

Results will be presented for the body alone as well as the wing-body combination. The location of the primary separation lines are thus of interest to both cases. For the body alone, the polar angle of separation is specified for the conical nose and the cylindrical afterbody. These positions are determined from the correlation curves of Reference 3, Figures 6 and 7. For the conical nose the value of ϕ_{s_1} of 163° was found from the correlation curve and for the cylindrical afterbody $\phi_{s_1} = 80°$. A cubic transition was made behind the nose from 163° at the shoulder of the nose to 80° a distance about 1.8 diameters behind the soulder with zero slope at

*This conclusion holds only for no shock detachments.

at each end. This distance is an approximation based on the schlieren pictures in Reference 13. For the wing-body combination the same locations of primary separation lines were specified in front of the winged section. Over the winged part of the combination no body primary separation line was specified. The Euler code continued to generate the primary separation line by the persistence of vorticity as described in Reference 3. Behind the wing, the afterbody separation line was taken as that for the body alone. The wing-tip separation was handled in this example in the same manner as for the previous example, i.e., a Kutta condition was applied to ensure that the flow on the upper surface at the wing tip separates parallel to the tip.

It is noted that although the body alone nominal angle of attack is 16°, the actual angle in the wind tunnel was 16.85° because of model deflection. This angle was used in the calculations. For the wing-body combination, the actual angle of attack was 17.45° for a 16° nominal angle of attack.

5.2 Body-Alone Flow-Field Comparisons

While the primary purpose of this study is to make flow-field comparisons between data and Euler code predictions, it is important to know if the shed vorticity and body loading are well predicted by the Euler code. For this body the vorticity distribution was not measured although the body axial loading distribution is available from Reference 14 and the body flow field from Reference 7. Vortex strengths for an ogive cylinder body as measured and as calculated by an Euler code were favorably compared in Reference 2. It is a resonable conjecture that the Euler code will predict the amount of vorticity shed by the present cone-cylinder given the primary separation lines on

cone and cylinder. The experimental axial loadings will now be compared with the prediction of the Euler code before considering the body flow-field results.

The axial distribution of local normal-force coefficient per unit angle of attack on the Bumblebee body is shown in Figure 14 where the experimental loading is compared with the predictions of the Euler code. On the conical nose, which extends to z/D = 1.86, the loading is linear with axial distance, and is very well predicted by the Euler code with the flow separation model for the conical nose. Crossing the shoulder onto the body a sharp decrease in loading is predicted which also agrees well with the data. Behind the shoulder on the cylindrical portion the loading falls asymptotically. However, the data exhibit a more rapid fall than the Euler code so that the loading at the survey station is somewhat over-predicted.

The flow velocity vectors at the survey station in the upper quadrant as measured are presented in Figure 15 to give a general idea of the flow field. The radial lines differ by increments of 5°. There is evidence of a vortex and recirculation region above the body. Some of the measured flow angularities at the extreme right seem to be excessive for some unknown reason. Also the flow sidewash angles on the plane of symmetry above the body should be zero but are not.

Comparable results obtained from the Euler code are shown in Figure 16 for the upper and lower quadrants. While the same qualitative flow character is exhibited, there are definte quantitative differences in the flows. These are best exhibited by detailed comparisons along radial lines in the flow as presented in the following figures.

Detailed comparisons will be made for the following flow quantities at z/D = 10.95.

Quantity	Figure
1. Flow angle normal to radius, α_f	17
2. Angle of radial outflow, β_f	18
3. Local Mach number, M_l	19
4. Ratio of local dynamic pressure to free-stream value, q_l/q_∞	20
5. Ratio of local total pressure to free-stream value, p_{t_l}/p_{t_∞}	21

Comparisons are made along radial lines at various angular locations around the body. Letting $\phi = 0$ be the windward plane of symmetry, comparisons are shown for $\phi = 0$, 45°, 90°, 135°, and 180° for each of the above quantities.

Before examination of the comparisons between data and predictions, it should be pointed out that two series of predictions were made. The first series uses a nonvariable mesh from the shoulder of the body all the way downstream. This mesh has 40 equally spaced radial nodal points and 37 nodal points in the polar angle. The angular spacing of the radial mesh lines was uniform. The conical nose was calculated with a coarser grid of 17 by 19 versus 40 by 37 on the cylindrical body. It was found that the radial spacing on the windward side was adequate. On the leeward side the distance from the body to the nose wave is much greater than on the windward side with the result that the radial distance between nodal points is much greater. Since a reverse flow regime occurs on the leeward side, the spacing was such that this reverse flow was not well resolved in the radial direction. Thus, a second series of calculations was run.

In the second series of calculations, radial clustering was used to improve the mesh resolution on the leeward side, particularly in the region of the vortex and on the leeward meridian. Let

$$\xi_u = \frac{r - a}{r_s - a} \tag{5}$$

be the parameter associated with the unclustered mesh. Then the clustering was accomplished by the following rule:

$$\xi_c = \xi_u^n \tag{6}$$

This equation produces a clustering of the radial nodes near the body which is controlled through the use of the parameter n.

In the first clustering run, a value of n was chosen which gave fairly fine clustering near the body and the clustering was started slightly behind the body shoulder at Z = 3.0. After proceeding satisfactorily about half way down the body, the code developed an instability which prevented further calculation. This instability was overcome by applying the clustering gradually according to the following schedule.

Z	n
3-6	0
6-11	1.2
11-15	1.35

This approach eliminated the instability.

The original Euler series of calculations with no clustering developed oscillation as a function of r/a for some of the quantities. For α_f and β_f no serious oscillations occurred; for M_1 serious oscillations occurred at $\theta = 90°$ and 135°; for q_1/q_∞ and p_{t_1}/p_{t_∞} serious oscillations occurred at $\theta = 135°$ and 180°. The oscillations occurred principally over the

inboard stations. The two series are generally in agreement over the outboard stations. Thus, the oscillations did not influence the accuracy outboard. It is interesting that α_f and β_f were much less subject to oscillations than M_1, q_1/q_∞ and p_{t_1}/p_{t_∞}. In view of these facts, it was decided to cluster the radial nodes in the vicinity of the body. This approach led to generally lesser oscillations, although they were not entirely eliminated as seen in Figures 17 to 21. Comparisons with the data will be made for the calculations based on clustering.

Comparisons between the Euler calculations and data for the flow angle normal to the radial lines are shown in Figure 17. The quantity α_f should be zero for the $\phi = 0$ and $\phi = 180°$ radial lines [Fig. 17(a) and (e)]. It is noted that several data points show values of α_f from 4° to 5°, a result interpreted here as possible experimental error. The data in Figure 17(d) exhibit differences for measurements taken at corresponding points on the left- and right-hand sides of the body which are as much as 8°. For $\phi = 45°$ [Fig. 17(b)] the theory underpredicts the values of α_f slightly, but the data exhibit a systematic trend. For $\phi = 90°$ [Fig. 17(c)] the same results as for $\phi = 45°$ are obtained. The reverse flow near the body is not well resolved by the mesh.

For $\phi = 135°$ [Fig. 17(d)] there is reverse flow near the body but the data are not adequate to pin down the reversal point. The flow reversal near the body is predicted by the Euler code at about $r/a = 1.4$.

The results for the radial flow angles measured with respect to the body axial direction are presented in Figure 18. It is noted that $\beta_f = 0$ at the body surface and is positive for outflow. The only repeat data [for $\phi = 135°$, Fig. 18(d)] exhibit a variation in β_f from left to right as large as 9°. However, most of the data exhibit systematic variations which are in fair

agreement with the prediction except for the inboard station for $\phi = 135°$ where the accuracy of both data and theory are in question. The oscillation in the theory may be associated with too few nodal points in the reverse flow. The flow angularity α_f is generally well enough predicted for most engineering purposes, but β_f is well predicted only on the windward side. The crossflow stagnation point for $\phi = 180°$ is predicted at about r/a of 2.4 [Fig. 18(e)] and from the data is at about $r/a = 3.1$.

The comparisons for local Mach number are shown in Figure 19. Examining first the $\phi = 135°$ data, [Fig. 19(d)], it is seen that at r/a of 1.68 the Mach numbers between the left- and right-hand sides differ by about 0.2. For $\phi = 90°$ and 135° the mesh resolution was not sufficient to define the predicted curve for the inboard stations well and oscillation resulted. Dashed straight lines are used to connect adjacent predicted points. Generally, the predicted local Mach numbers are well within ±0.1 of the data on the windward side [Figs. 19(a)-(c)].

Consider now the comparisons for the ratio q_1/q_∞ in Figure 20. The only accuracy check available for the data and theory is that q_1/q_∞ should approach unity for large r/a. Both data and prediction exhibit this tendency. The data taken for $\phi = 135°$ and $\phi = 225°$ [Fig. 20(d)] exhibit differences in q_1/q_∞ of as much as 0.085. Before comparing the data and the predictions, it is noted that a strong oscillatory behavior of the solution occurs at $\phi = 135°$ for $r/a < 1.6$, a region of reverse flow. At $\phi = 180°$ [Fig. 20(e)] there are some mild oscillations in the inboard region. The difference between the predicted and measured values of q_1/q_∞ are within about 0.1 for $\phi = 0$, 45°, 90°, and for $\phi = 135°$ outside the reverse flow region. At $\phi = 180°$ the prediction generally over-predicts q_1/q_∞ by about 0.1.

The final flow quantity for which comparisons will be made is the ratio of local total pressure to free-stream total pressure. Figure 21(d) shows the repeatability of the measurements between corresponding points on the left and right sides. A difference as large as 0.1 in the ratio exists. For the windward positions, $\phi = 0°$ and $\phi = 45°$ [Figs. 21(a) and (b)] the Euler code somewhat overpredicts the total pressure on average. For $\phi = 135°$ [Fig. 21(d)], a position close to the vortex core, there is a region of reduced total pressure near the body. The total pressure on the leeward meridian [$\phi = 180°$, Fig. 21(e)] seems quite high for a vortical region. The value of the ratio greater than unity is clearly experimental error.

One point is noteworthy, that the calculated total pressure ratio has the same value for all points on the body; namely 0.917. This fact indicates that the body surface is at constant entropy. The entropy S of a given thermodynamic state can be related to that of a reference state by the following result from Equation 23(b) of Reference 15.

$$S - S_R = C_V \ell n \frac{p}{\rho^\gamma} - C_V \ell n \frac{p_R}{(\rho_R)^\gamma} \tag{7}$$

Since $\frac{p}{\rho^\gamma} = \frac{(R_G T_t)^\gamma}{p_t^{\gamma-1}}$

$$S = C_V \ell n \frac{(R_G T_t)^\gamma}{p_t^{\gamma-1}} + S_R - C_V \ell n \frac{p_R}{\rho_R^\gamma} \tag{8}$$

Thus, for constant total temperature, T_t, as assumed in the Euler code, the local total pressure depends only on the local entropy.

Except for regions of oscillations over the inboard station for $\phi = 135°$ and 180°; the Euler code predicts p_{t_1}/p_{t_∞} within 0.1 for all ϕ.

5.3 Wing-Body Flow-Field Comparisons

Data are available from Reference 7 for the flow quantities a distance 2 chord lengths behind the wing trailing edge of the Bumblebee rectangular wing and body combinations. Comparisons are made between the data and the predictions of the Euler code for flow angle normal to the radius (α_f), local Mach number (M_1), and local dynamic pressure ratio (q_1/q_∞). These are the parameters that are important in determining the normal force on a fin in a nonuniform flow field by strip theory. For instance, if $c_n(\alpha_f, M_1)$ is the two-dimensional normal-force coefficient corresponding to α_f and M_1 for the given airfoil section, then the fin normal-force coefficient C_{N_F} could be estimated by the following formula.

$$C_{N_F} = \frac{K}{S_F} \int_a^s cc_n(\alpha_f, M_1) \frac{q_1}{q_\infty} \, dy \qquad (9)$$

The normalization factor K would be evaluated by applying Equation (9) to the same wing for uniform flow conditions close to the mean values of α_f and M_1 at which a theoretical or experimental value of C_{N_F} is known. Comparisons are made for $\phi = 0°$, 45°, 90°, 135°, 150°, 160°, 170°, and 180°. Good coverage of the vortical region is thus obtained.

In applying the Euler code to this case the same clustering schedule was used as for the body alone. The afterbody primary separation line was specified as that given by the correlation curve for the cylinder thereby neglecting any effect of wing downwash on the separation line location.

It is also noted that the Euler calculations were made for $\alpha = 16.85°$ while the data were taken at $\alpha = 17.45°$. At $\alpha = 17.45°$ the Euler code developed instabilities over the wing which were not investigated. The difference in the angle of attack is not considered significant in terms of the overall comparisons because of uncertainty in the data and oscillations in the Euler results.

Consider now the comparisons for α_f, the angle of attack normal to the radius from the body center. With regard to the measurement accuracy, examine the data for the windward meridian ($\phi = 0°$) in Figure 22(a) and for the leeward meridian ($\phi = 180°$) in Figure 22(h). Here α_f should be zero for symmetric flow. Measured values of 3° to 4° are found although most of the values are quite small. The possibility of two stable states, one asymmetric, is considered unlikely, and it is assumed that the discrepancies are due to inaccuracies of some sort. Further insight into the accuracy of the α_f data is provided by repeat runs and by data for corresponding points on the left and right sides for $\phi = 135°$, 150°, 165°, and 170°. For $\phi = 135°$ and 150° [Fig. 22(d) and (e)] there is agreement between repeat runs and left-right data over the outer span but serious disagreement over the inner span. In general, the accuracy (repeatability?) of the data in the vortical region, 135° to 180°, is not good. Measurement in regions of rapid gradients or probe interference on the vortex are both possible sources of error.

Now with regard to the ability of the Euler code to predict α_f, a few points can be made. For the windward side, $\phi = 45°$ and $\phi = 90°$, the Euler code predicts the trends of the data well although there is an offset of a few degrees of the predictions from the data. A very narrow region of reverse flow is seen at $\phi = 90°$ since separation is near $\phi = 80°$. For the leeward side, $\phi = 135°$ to 180°, it can be said that the Euler code fits the data well in a mean sense, but the accuracy of the

data is not sufficient to make a critical judgement on the accuracy of the prediction of the Euler code in this region.

The local Mach number comparisons are presented in Figure 23. Repeat runs and data from corresponding left-right points are shown in Figures 23(d)-(h) to assess the accuracy of the Mach number data. For ϕ = 180°, the repeat runs are in good agreement. For ϕ = 170°, left-right symmetry data show large differences. For ϕ = 160° the data are in fair agreement except at one position near r/a = 2.5. For ϕ = 150° there is significant disagreement over the inboard stations. For ϕ = 135° the data agree well.

With respect to the ability of the Euler code to predict M_1, the agreement between data and prediction is good for ϕ = 0°, 45°, and 90°. For ϕ = 135° and 150° the Mach number data exhibit a dip in the middle of the span which is not predicted. The predictions are good in a mean sense for ϕ = 160°, 170°, and 180°.

Comparisons for the local dynamic-pressure data are shown in Figure 24. Only fair agreement between repeat runs and left-right symmetry data is shown for ϕ = 135°, 160° and 180°. For ϕ = 170° large discrepancies occur between the left-right symmetry data although repeat runs on either side are in agreement. For ϕ = 150°, significant disagreement occurs in the data.

Turning now to comparisons between Euler code prediction and experiment, agreement is good for ϕ = 0° and 45° and fair for ϕ = 90°. For ϕ = 135°, the predictions show oscillations over the inboard stations, oscillations which disappear by the time ϕ = 180°. The dips in dynamic pressure near the midspan are not predicted for ϕ = 135° and 160°. No critical comparison can be made for ϕ = 170° because of the scatter of the data. For ϕ = 180° the Euler code predicts the data well.

6. WING-BODY-TAIL EXAMPLE

In the previous sections of this report, the accuracy of the Euler code for predicting body-alone and wing-alone loading characteristics was examined by comparison with data. Also, its accuracy in predicting the nonuniform flow-field characteristics at a tail location was examined for both a body alone and a wing-body combination for which data were available. No data were found for the pressure distribution on the tail of a wing-body-tail combination which were suitable for verifying the accuracy of the Euler code to predict the loading distribution on a tail in a nonuniform vortical flow field. As an illustrative example for a complete wing-body-tail combination calculated results are presented for the loading distribution for a tail placed in the nonuniform flow field of the body alone and the wing-body with the tail leading edges starting just behind the position of the flow-field survey at Z = 15.

The body alone and the wing-body chosen for the illustrative example are those shown in Figure 13. To form the tail, fins with dimensions identical to those of the wing were used. The tail leading edge was placed at Z = 15.1, just behind the Z = 15.0 survey station. To maximize the vortex interference, an interdigitation angle of 45° was introduced. Comparisons were made between body-tail and body-wing-tail with respect to pressure distributions, span loading, and normal force. Only the upper fin was included in the Euler code, and comparisons were made only for this fin since it experiences maximum vortex interference.

The flow parameters just in front of the fin leading edge are discussed first with a view to explaining the differences in the fin loading for the body-tail and wing-body-tail. The most important parameter is the angle of attack normal to the fin at the leading edge shown in Figure 25(a). Both cases exhibit downwash over the first 15 to 20 percent of the exposed semispan. Large angles of upwash occur outboard of the 20 percent semispan station. It seems probable that the large loadings outboard of this station could propogate inboard over the rear part of the wing and possibly wipe out any negative span loading on the inboard section. The presence of the wing reduces the angle of attack over the fin by about 6° to 7° over the outer 40 percent of the semispan. The calculated Mach number distribution across the semispan of the two configurations is shown in Figure 25(b). Addition of the wing to the body reduces the calculated Mach number at the fin leading edge by about 5 to 10 percent in the outer half of the semispan. Since the two-dimensional normal-force curve slope varies approximately inversely as $(M^2 - 1)^{1/2}$, some small gain in fin normal force would result from adding the wing to the body-tail. The dynamic pressure at the tail, shown in Figure 25(c), is greater for the wing-body-tail than for the body-tail in the middle of the fin semispan but the relationship reverses over the outer part of the fin. This suggests very small change in fin loading as the result of dynamic pressure effect. On balance, it appears that the fin loading would be expected to be less for the wing-body-tail than for the body-tail as a result principally of the angle-of-attack effect.

Consider now the pressure distributions near the midspan (53 percent semispan) as shown in Figure 26 for both cases. As expected the magnitude of the pressures for the wing-body-tail are substantially less than for the body-tail on both surfaces. The same result is seen for the pressure distributions along the midchord of the tail as shown in Figure 27. The local loading at the root chord is essentially zero.

The local section normal-force coefficient for a rectangular wing are proportional to the span loading. These are shown in Figure 23 for both body-tail and wing-body-tail. Large reductions in span loading occur on the outboard half of the fin because of the addition of the wing. Over the inboard 20 percent, not much difference in span loading occurs. However, the loading over the outboard section of the wing has carried over to a considerable extent onto the inboard section sufficient to nearly wipe out any negative span loading at the root location due to large downwash angles as exhibited in Figure 25(a).

7. CONCLUDING REMARKS

The present report is concerned with evaluating a supersonic marching Euler code with respect to its ability to predict loading and flow fields of bodies, wings, wing-bodies, and wing-body-tails. The vortices due to the body and afterbody are simulated in the Euler code by introducing primary separation lines at the locations determined from experimental correlations and applying a Kutta-type condition on the primary separation lines. The wing or fin separation vortices are introduced into the code by applying a Kutta condition to all subsonic edges. Data for checking the accuracy of the Euler code are incomplete, but a number of comparisons have been made. Such comparisons include body axial loading, detailed wing pressure distributions, flow fields of a body alone and behind the wing of a wing-body combination. An example calculation for a wing-body-tail combination was also carried out. Comparisons were also made with several other theories where possible. The details of the comparisons and what they show with regard to the Euler code are summarized below.

The same cone-cylinder body was used for the body alone and wing-body comparisons. As prelude to the body-alone flow-field calculations, the axial loading distributions based on experiment and the Euler code were compared. The comparison (Fig. 14) showed excellent agreement on the cone with separated flow, and good agreement on the cylindrical after-body, the loading falling off slightly more rapidly than predicted.

An Euler code with an unclustered mesh applied to the body showed oscillation in some flow-field variables on the leeward side of the body near the body. This was ascribed to too large a spacing between radial nodes to resolve well the reverse flow near the body and the flow structure near the vortex. Accordingly, radial clustering of the points near the body was used. This device reduced the oscillations near the body but did not completely eliminate them. The clustering was applied gradually with increasing downstream distance to stabilize the calculation. It was found that the flow directions varied more smoothly than the local Mach number, local dynamic pressure, and local total pressure. The comparisons were made at a downstream distance behind the nose apex of 10.9 body diameters for $\alpha = 16.85°$ and $M_\infty = 2.0$.

Generally speaking, the Euler code predicted the local flow field on the windward side of the body quite well. However, on the leeward side of the body, a critical comparison could not be made with the data since the data did not repeat well and some oscillations resulted in the calculated Euler results for inboard stations. On the outboard stations the comparison of data and theory was generally fair. Further refinement of the Euler code is required, and a better set of data is necessary before critical comparisons can be made for the reverse flow and vortex region on the leeward side.

Comparisons were made with the detailed pressure distribution of an aspect ratio 2 rectangular wing at $M_\infty = 2.86$ and $\alpha = 10°$. The Euler code predicted the pressure distributions well except near the wing tip. The use of the Kutta condition resulted in a small improvement of the agreement there. The span loading distribution was well predicted to about 90 percent of the exposed semispan. On the upper surface the flow separated at the shoulder of the trailing-edge wedge and the separation was not predicted by the Euler code. The experimental pressure distributions were also compared with a panel code modified to account for nonlinear shock-expansion effects. The nonlinear shock-expansion effects were large and were well predicted by the modified panel code.

The Euler code was originally written for body-wing configurations of the type previously discussed. In order to make it operational for the rectangular wing alone it was necessary to attach a semispan wing to a large hollow rectangular fuselage aligned with the flow to simulate a reflection plane.

No data exist for the wing-alone flow field but calculations were made to determine the flow field three chord lengths behind the wing trailing edge. These calculations were made to investigate the effects of wing thickness and the wing edge Kutta condition on the calculated flow field. It was found that the effect of these two parameters on the calculated flow field are small. The Euler code without an edge Kutta condition still produces shed vorticity from the edge in a manner which is not fully understood.

A series of comparisons were made between the Euler code prediction and the flow-field data about three-chord lengths behind the wing leading edge for the wing-body combination. A clustered computational mesh with the Kutta condition but with no wing thickness was used. The nature of the agreement between data and the Euler code predictions was similar to that for the body alone.

As a final illustration, a calculative example was carried out with the Euler code to determine the loading on a tail interdigitated 45° with respect to the wing. The tail was identical to the wing in planform and thickness distribution and was located about three body diameters behind the wing. The effect of the wing in reducing the tail loading from that for the body-tail combination was illustrated.

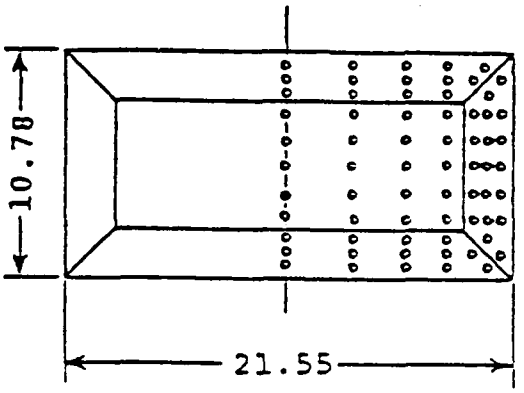

(a) Pressure tap layout (Ref. 4)

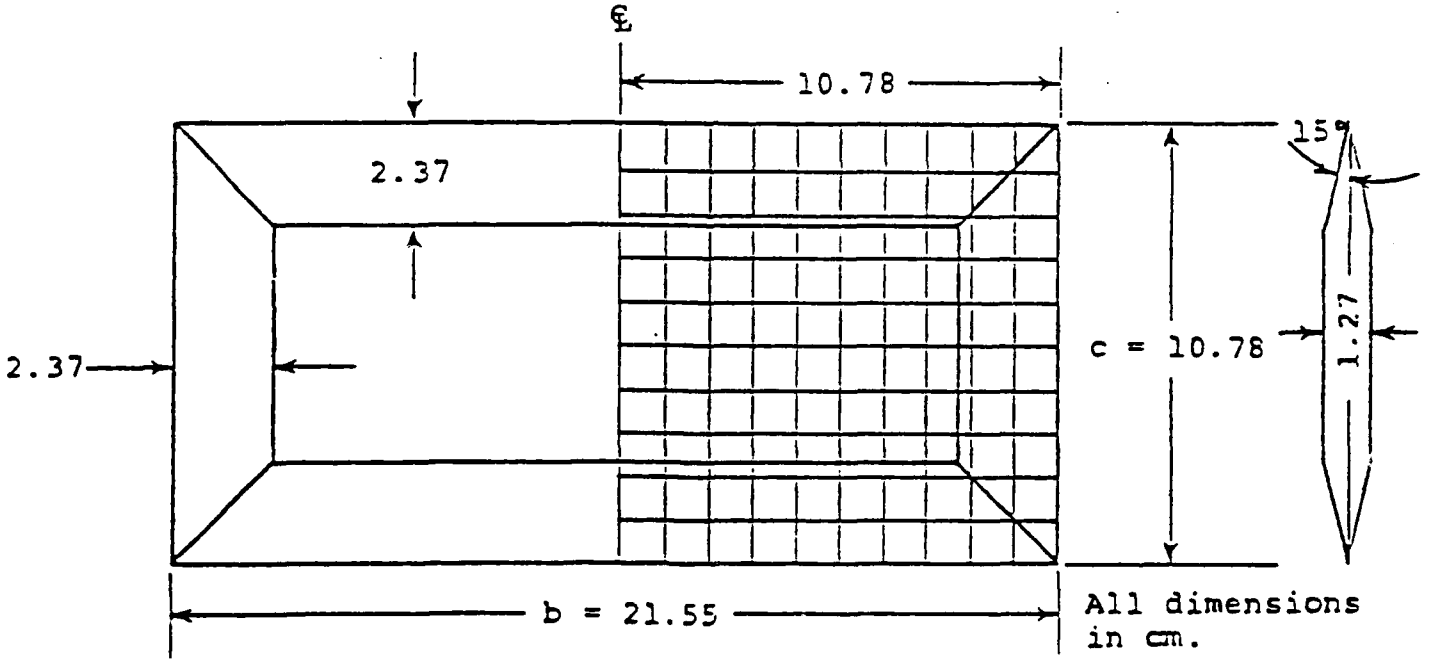

(b) Geometrical details and 10 x 10 paneling layout for prediction.

Figure 1.- AR = 2 rectangular wing, bevelled on the edges.

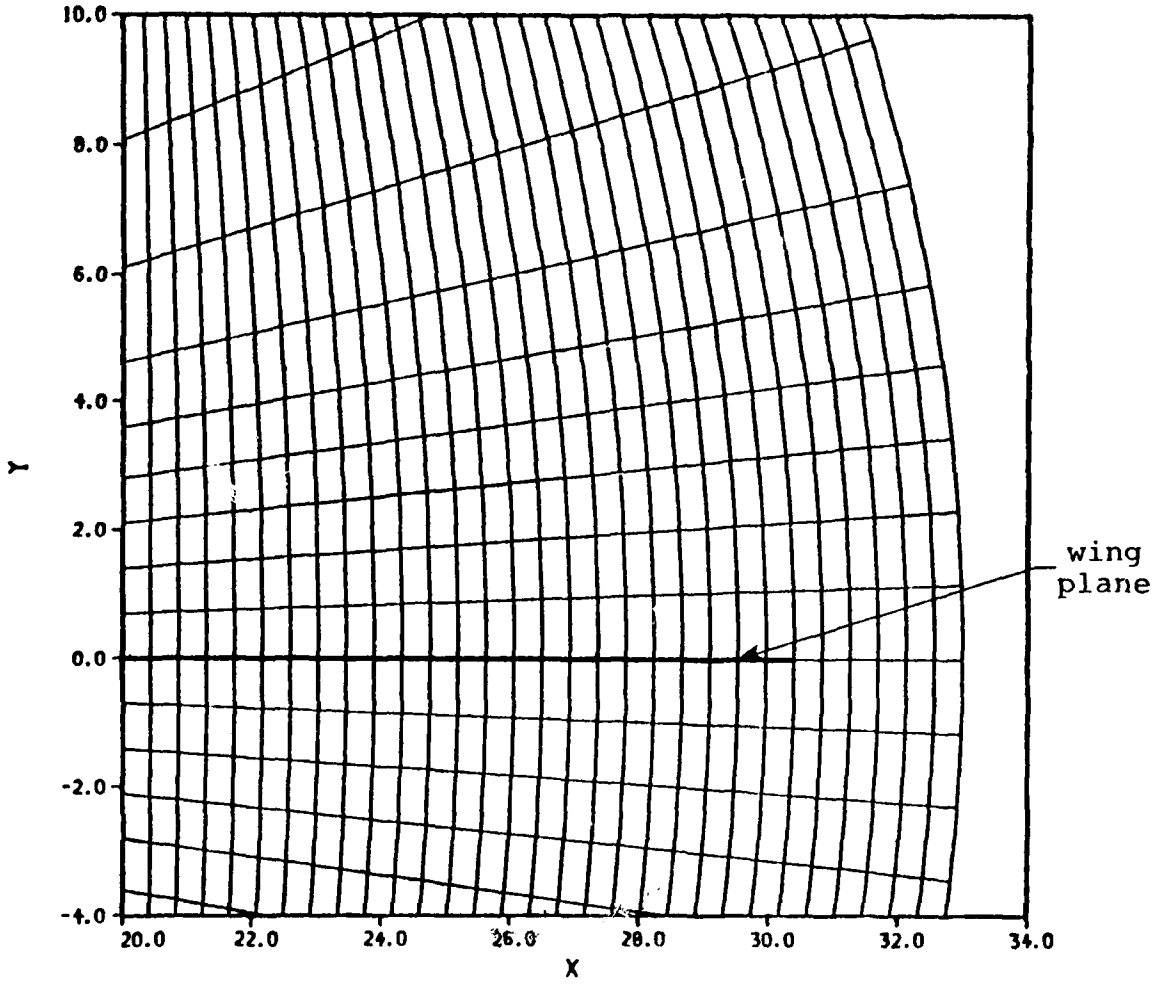

Figure 2.- Grid plot for Langley wing no. 9, 31 × 31 mesh; $M_\infty = 2.86$, $\alpha = 10.00$.

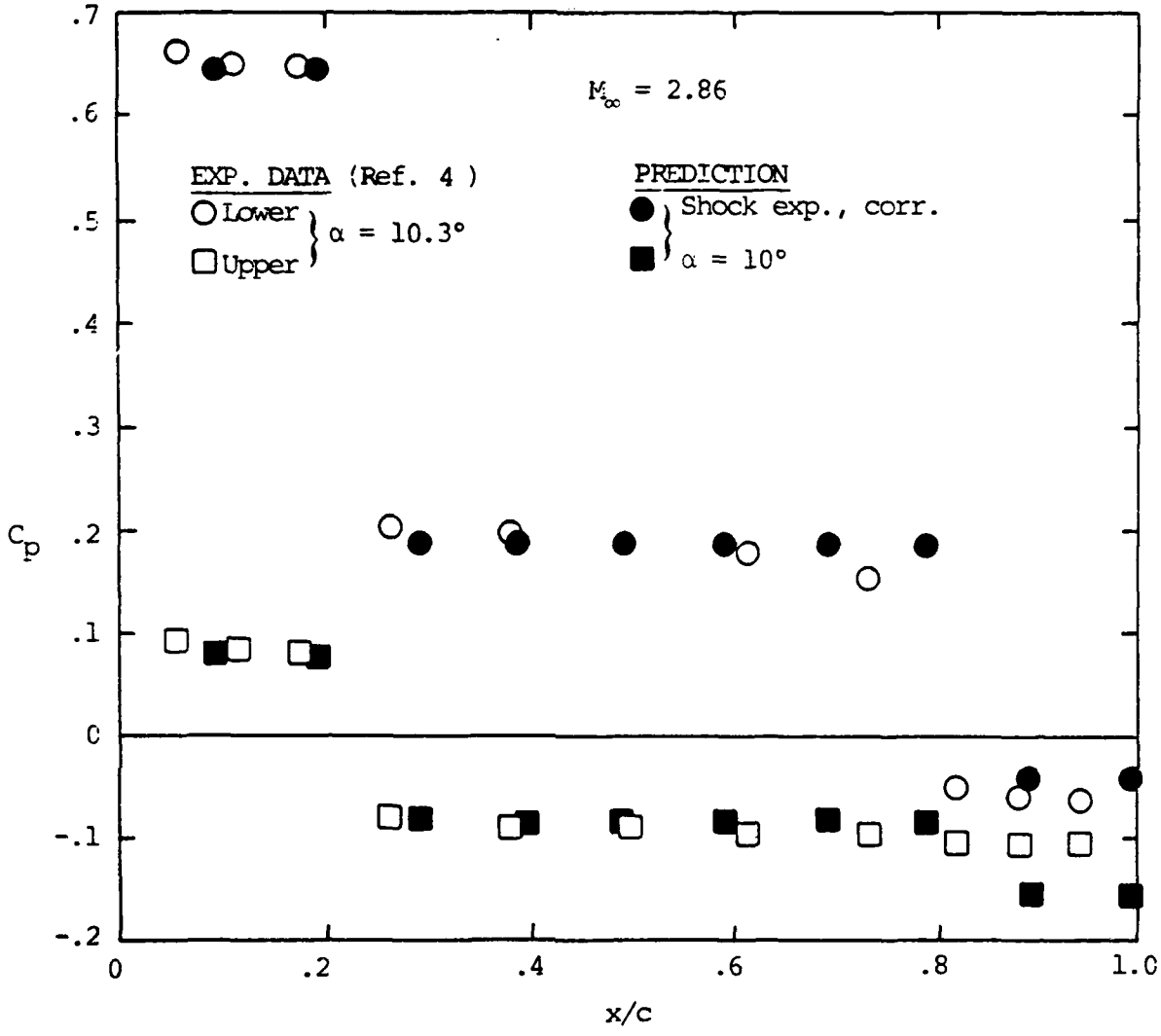

(a) Chordwise pressure distribution on upper and lower surfaces, $\frac{y}{b/2}$ = 0.53

Figure 3.- Pressure distribution acting on an AR = 2 rectangular wing as measured and as calculated by a nonlinear panel method.

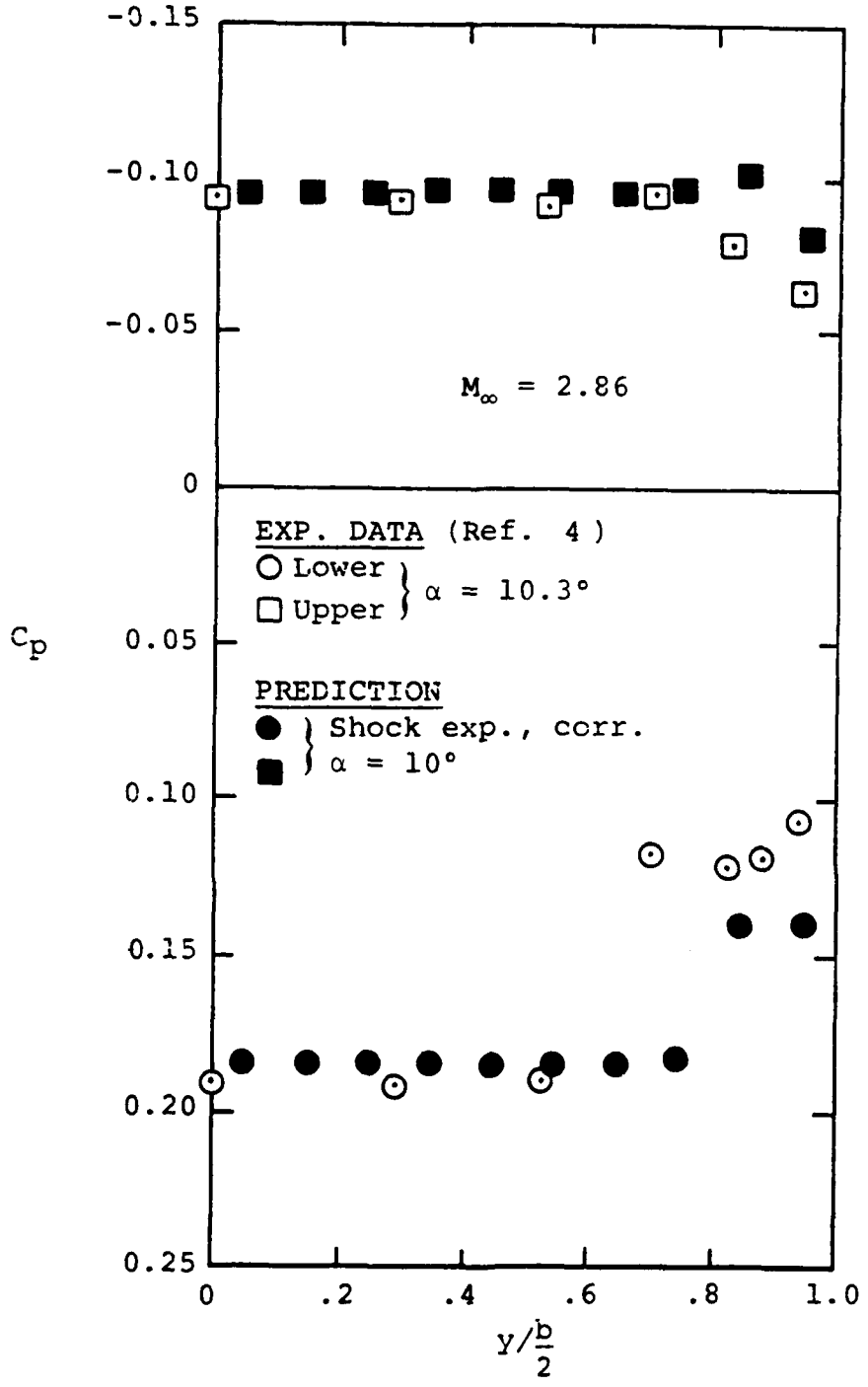

(b) Spanwise pressure distributions on upper and lower surfaces, x/c = 0.5

Figure 3.- Concluded.

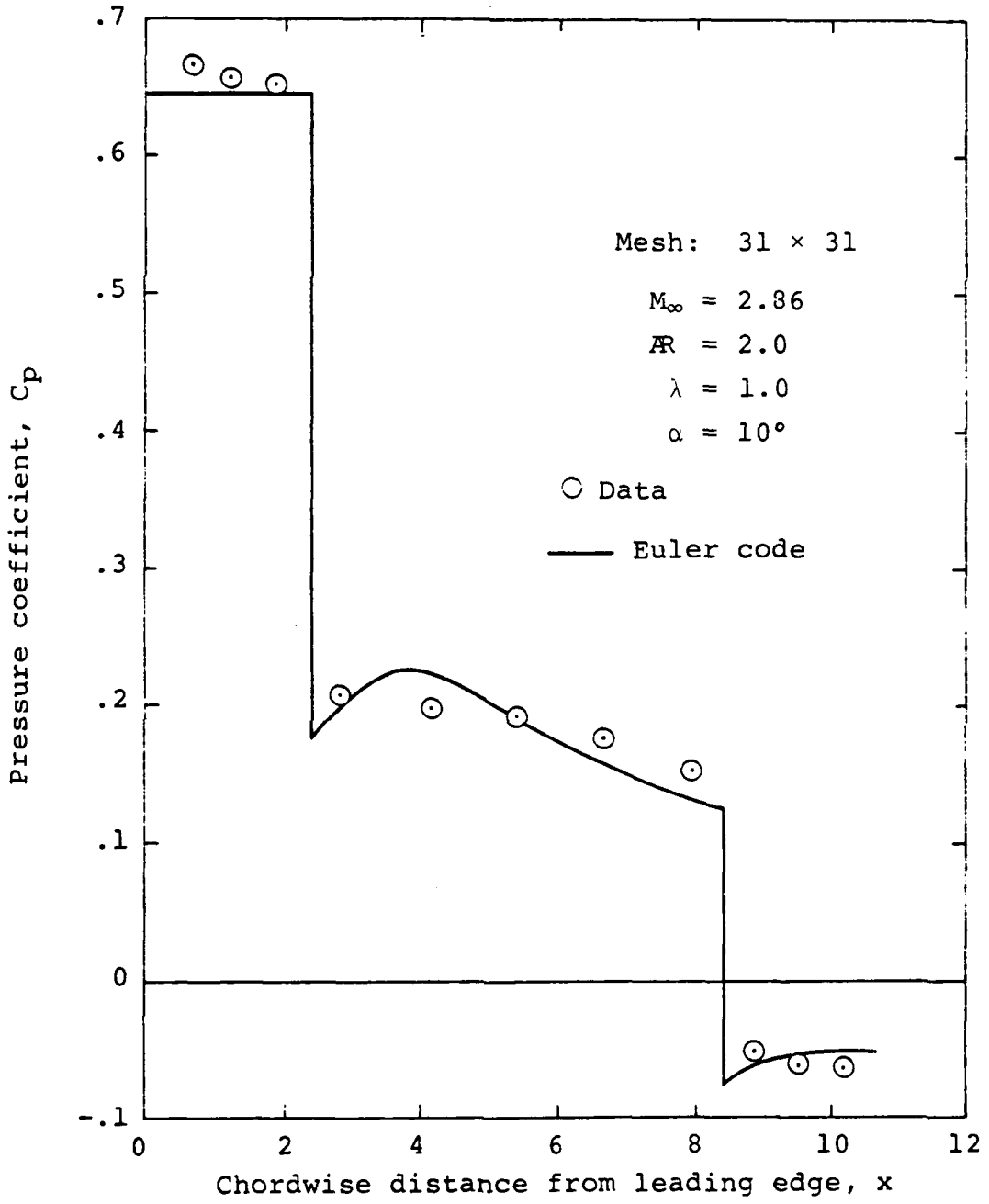

(a) Lower surface

Figure 4.- Chordwise pressure distribution on an AR = 2 rectangular wing as measured and as calculated by an Euler code.

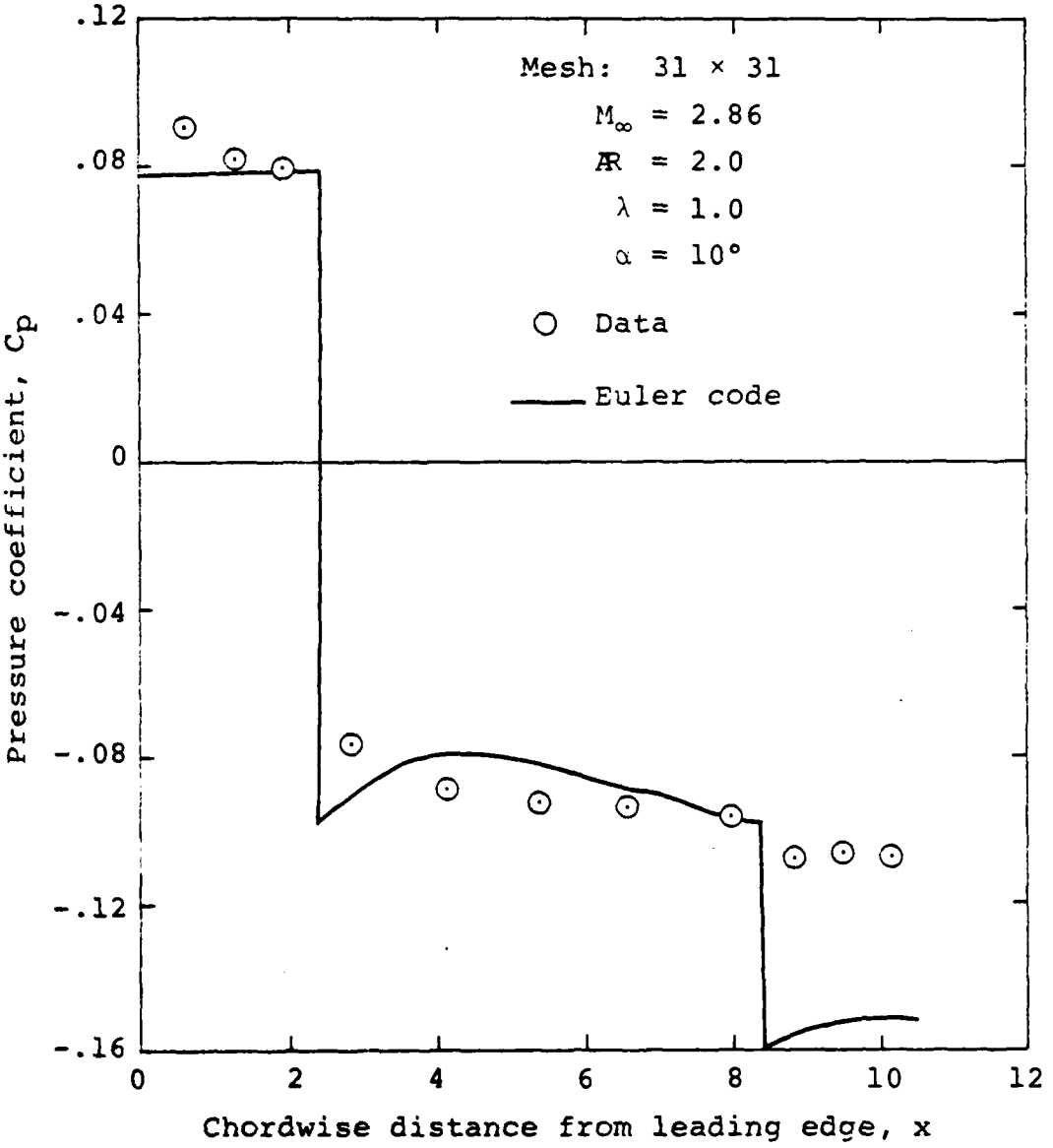

(b) Upper surface

Figure 4.- Concluded.

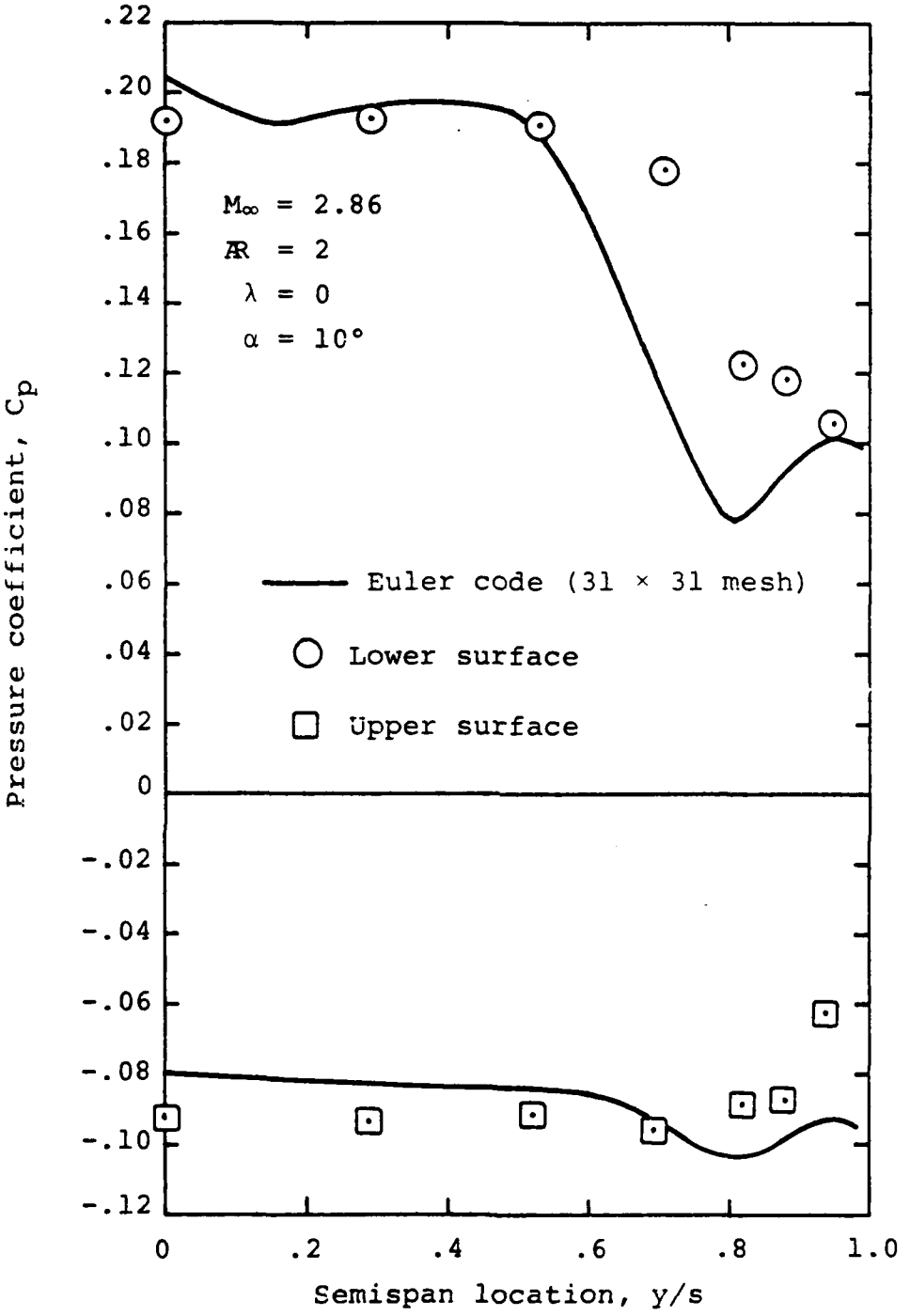

Figure 5.- Spanwise pressure distribution at midchord of an AR = 2 rectangualr wing as measured and as calculated by an Euler code.

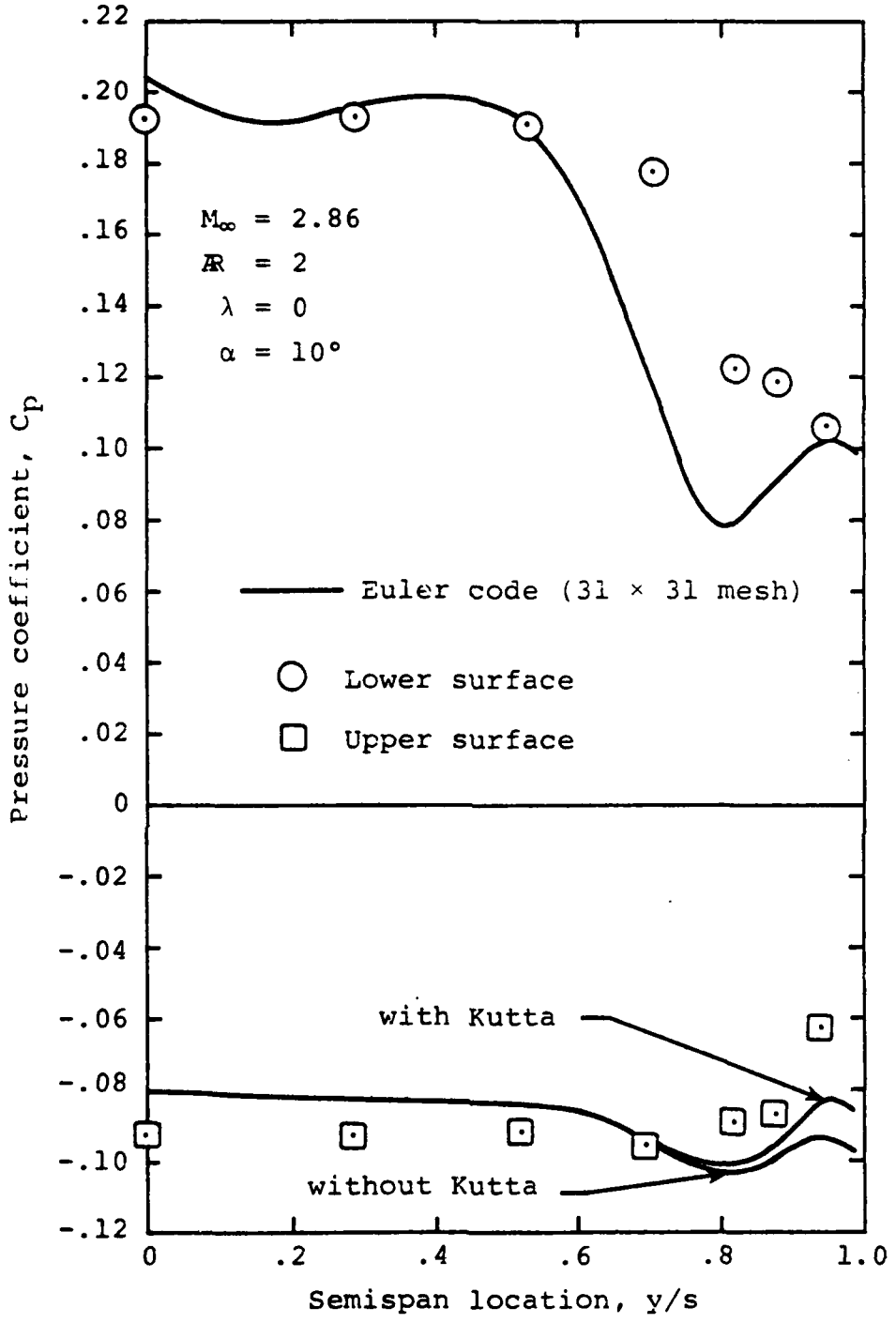

Figure 6.- Spanwise pressure distribution at midchord of an AR = 2 rectangular wing as measured and as calculated by an Euler code with and without a Kutta condition on the side edge.

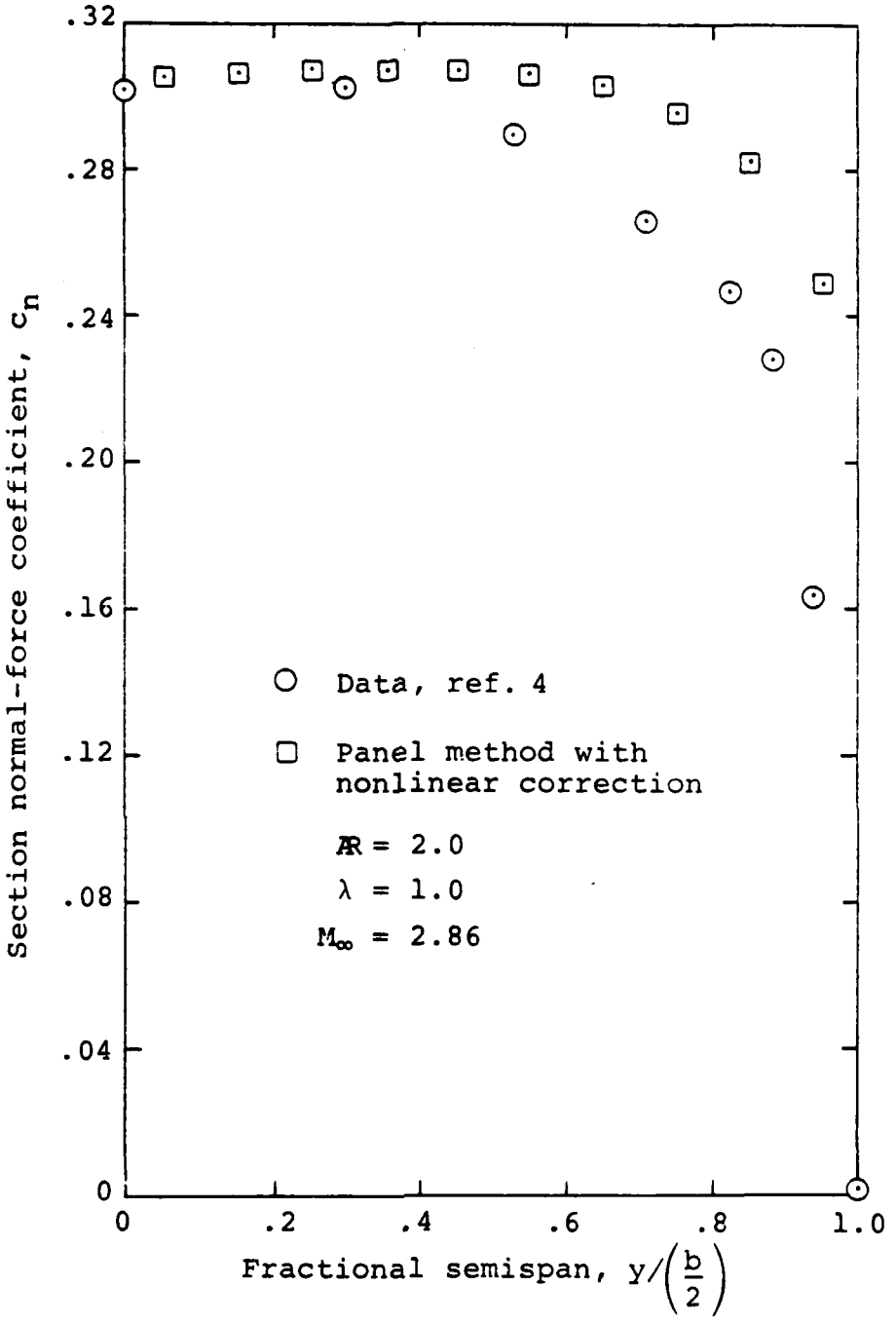

Figure 7.- Comparison of rectangular wing section normal-force coefficients from various sources.

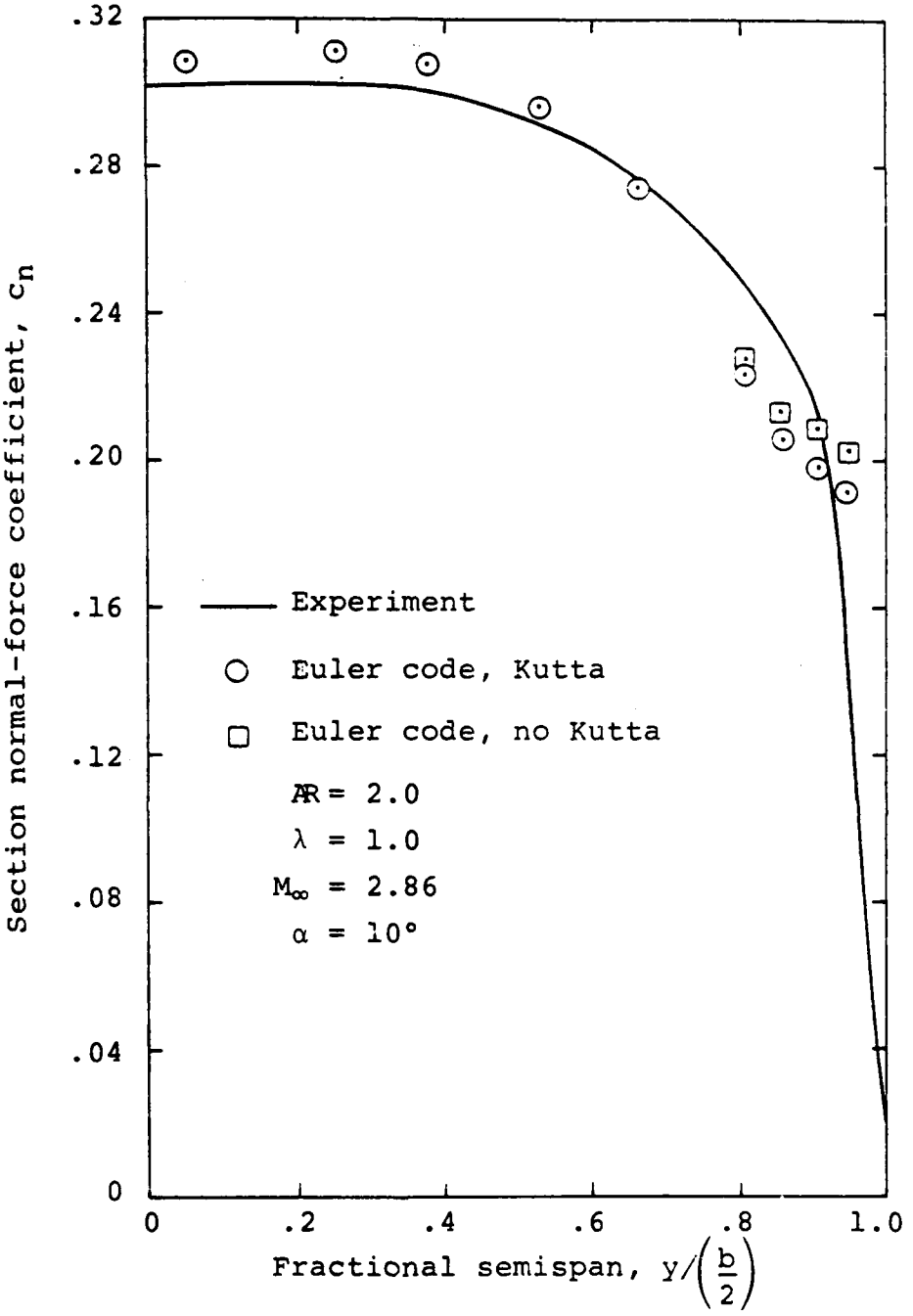

Figure 8.- Comparison of rectangular wing section normal-force coefficients from experiment and from Euler code.

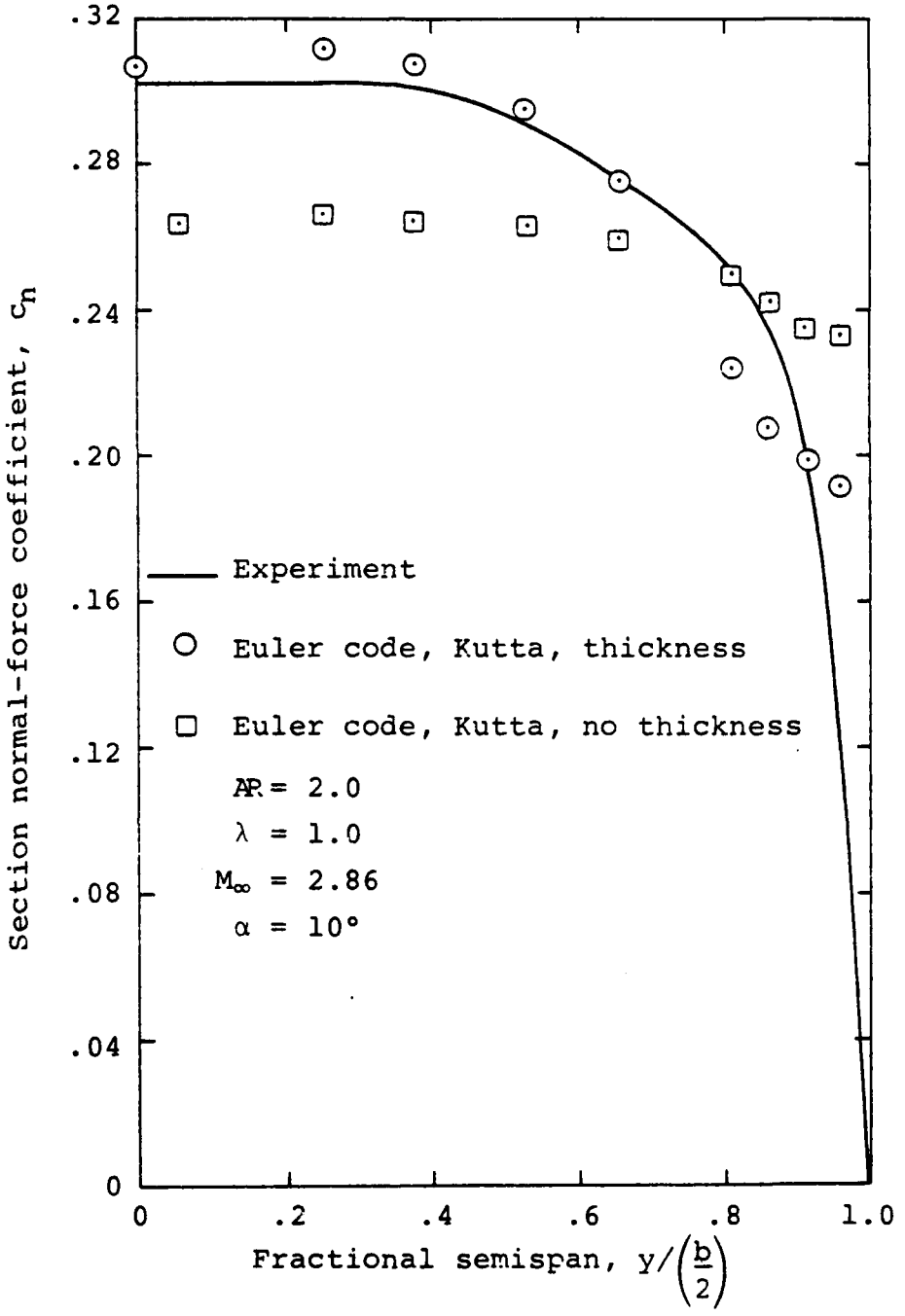

Figure 9.- Effect of wing thickness on section normal-force coefficients of rectangular wing as calculated by an Euler code.

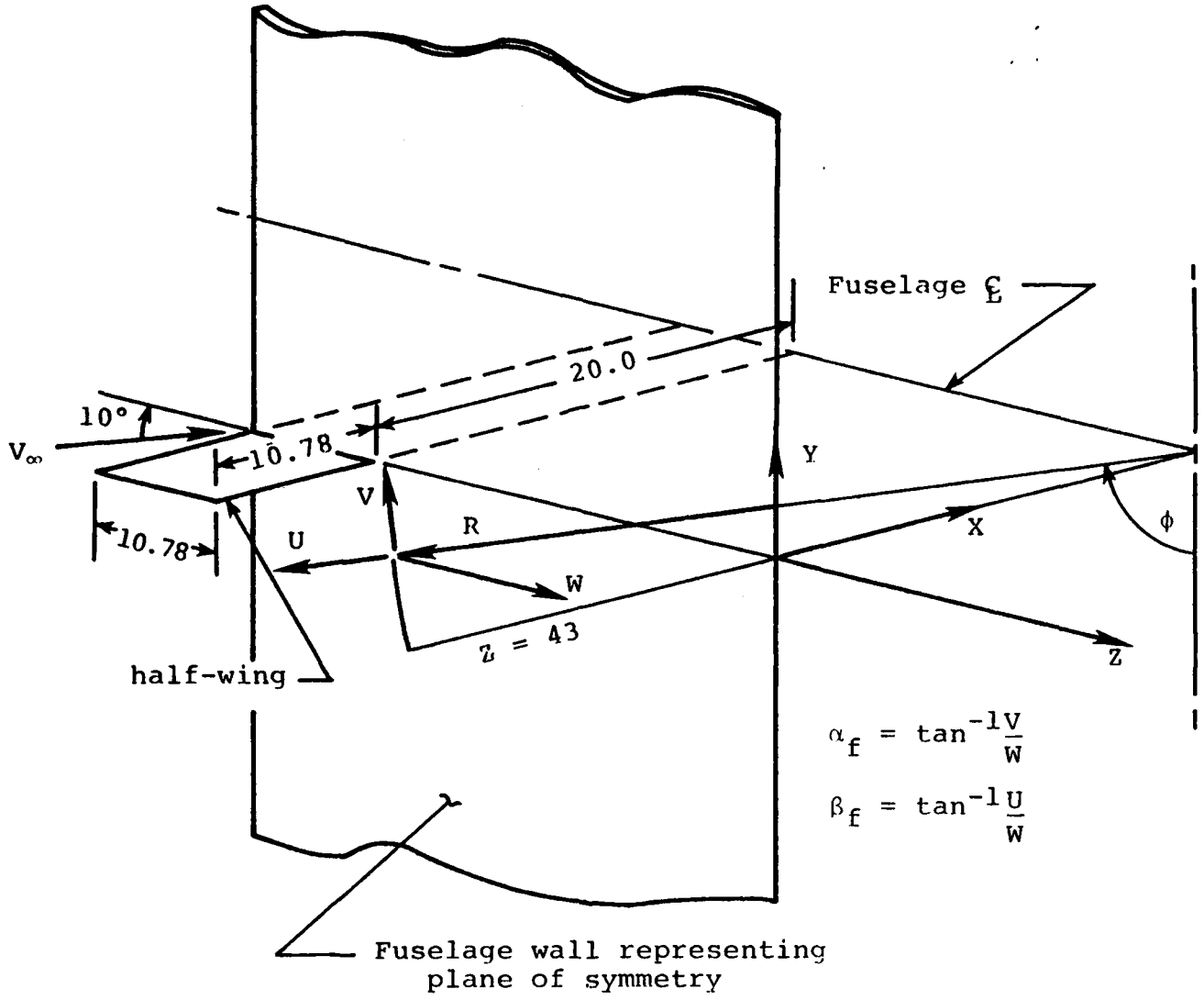

Figure 10.- Coordinate system used in Euler code to define flow angles for wing-alone model.

	No Thickness				Thickness			
	Kutta		No Kutta		Kutta		No Kutta	
R	α_f	β_f	α_f	β_f	α_f	β_f	α_f	β_f
20.0	7.53	0	7.53	0	8.63	0	8.08	0
22.8	9.75	.54	9.75	.51	9.60	.20	9.37	.14
25.7	9.75	1.67	9.75	1.67	9.40	.52	9.21	.48
28.5	9.47	1.81	9.46	1.81	9.65	1.75	9.50	1.78
31.4	10.32	1.67	10.32	1.68	10.30	2.30	10.20	2.27
37.0	11.12	.96	11.12	.96		2.11	10.96	2.14
39.8	10.52	.99	10.84	.84	10.78	2.00	11.33	1.77
42.7	10.18	1.18	10.18	1.18	10.46	1.51	10.37	1.57
45.5	9.81	.84	9.65	1.47	9.90	2.42	9.86	2.47
48.4	10.0	0	10.0	0	10.0	0	10.0	0

(a) Extended wing chord plane

Figure 11.- Effect of wing thickness and the Kutta condition on the calculated flow angles three chord lengths behind a rectangular wing at $M_\infty = 2.86$ and $\alpha = 10°$.

		No Thickness				Thickness			
		Kutta		No Kutta		Kutta		No Kutta	
ϕ	Y	α_f	β_f	α_f	β_f	α_f	β_f	α_f	β_f
47	-18.65	1.08	-1.00	1.08	-1.00	1.93	-1.80	1.70	-1.59
55	-14.01	1.78	-1.25	1.78	-1.25	3.26	-2.28	2.94	-2.06
62	-10.63	2.97	-1.58	2.97	-1.58	4.98	-2.65	4.57	-2.44
68	-8.08	4.54	-1.84	4.54	-1.84	6.65	-2.70	6.17	-2.50
73	-6.11	6.13	-1.88		-1.88	7.98	-2.45	7.43	-2.28
79.8	-3.60	7.79	-1.41	7.78	-1.41	8.14	-1.66	8.54	-1.55
86	-1.40	7.20	-.51	7.20	-.51	8.19	-.58	7.66	-.54
90	0		0	7.53	0	8.63	0	8.08	0
94	1.40	7.80	.55	7.80	.55	8.93	.63	8.36	.59
100.2	3.60	7.33	1.33	7.33	1.33	8.41	1.52	8.75	1.40
107	6.11	6.55	2.01	6.55	2.01	7.41	2.20	6.86	2.10
112	8.08	6.21	2.52	6.21	2.52	6.89	2.80	6.43	2.61
118	10.63	5.64	3.01	5.64	3.01	6.08	3.24	5.70	3.04
125	14.01	4.62	3.24	4.62	3.24	4.86	3.41	4.58	3.21
133	18.65	3.27	3.05	3.27	3.05	3.42	3.19	3.23	3.01

(b) Vertical plane of symmetry

Figure 11.- Continued.

R	No Thickness				Thickness			
	Kutta		No Kutta		Kutta		No Kutta	
	α_f	β_f	α_f	β_f	α_f	β_f	α_f	β_f
20.3	7.33	1.33	7.33	1.33	8.41	1.52	7.75	1.40
23.3	8.54	2.24	8.54	2.25	8.30	1.59	8.26	1.52
26.3	7.08		7.04	1.90	7.17	.80	7.14	.80
29.3	6.39	1.10	6.40	1.09	6.03	.80	6.03	.81
32.4	13.66	.18	13.66	.17	13.18	.75	12.59	.72
35.4	10.69	.85	10.69	.83	11.75	.76	12.12	.98
38.4	10.89	1.59	11.90	1.58	12.58	2.24	12.41	2.33
41.4	11.05	1.68	11.05	1.68	11.12	2.89	11.11	2.93
44.4	10.32	2.28	10.31	2.27	10.00	2.52	9.99	2.15
47.4	9.97	2.08	9.94	2.08	10.06	3.54	10.05	3.52
50.4	9.84	1.90	9.84	1.90	9.84	1.79	9.84	1.79

(c) Radial trace through vortex center;
ϕ = 100.2°

Figure 11.- Concluded.

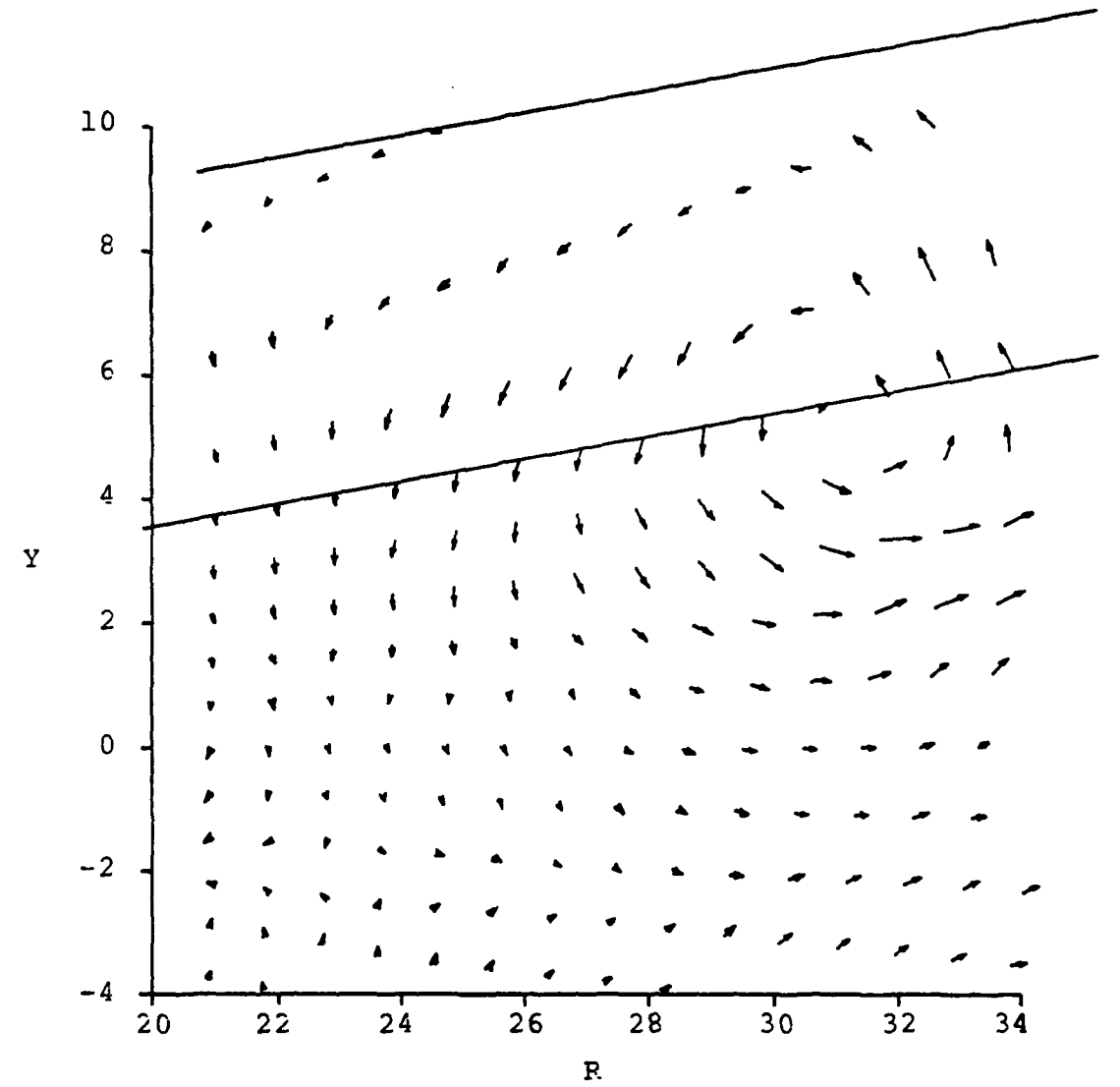

Figure 12.- Cross-flow velocity vector plot with V_∞ sin α subtracted out three chord lengths behind $\mathcal{AR}$ = 2 rectangular wing; M_∞ = 2.86, α = 10, Z = 43.16.

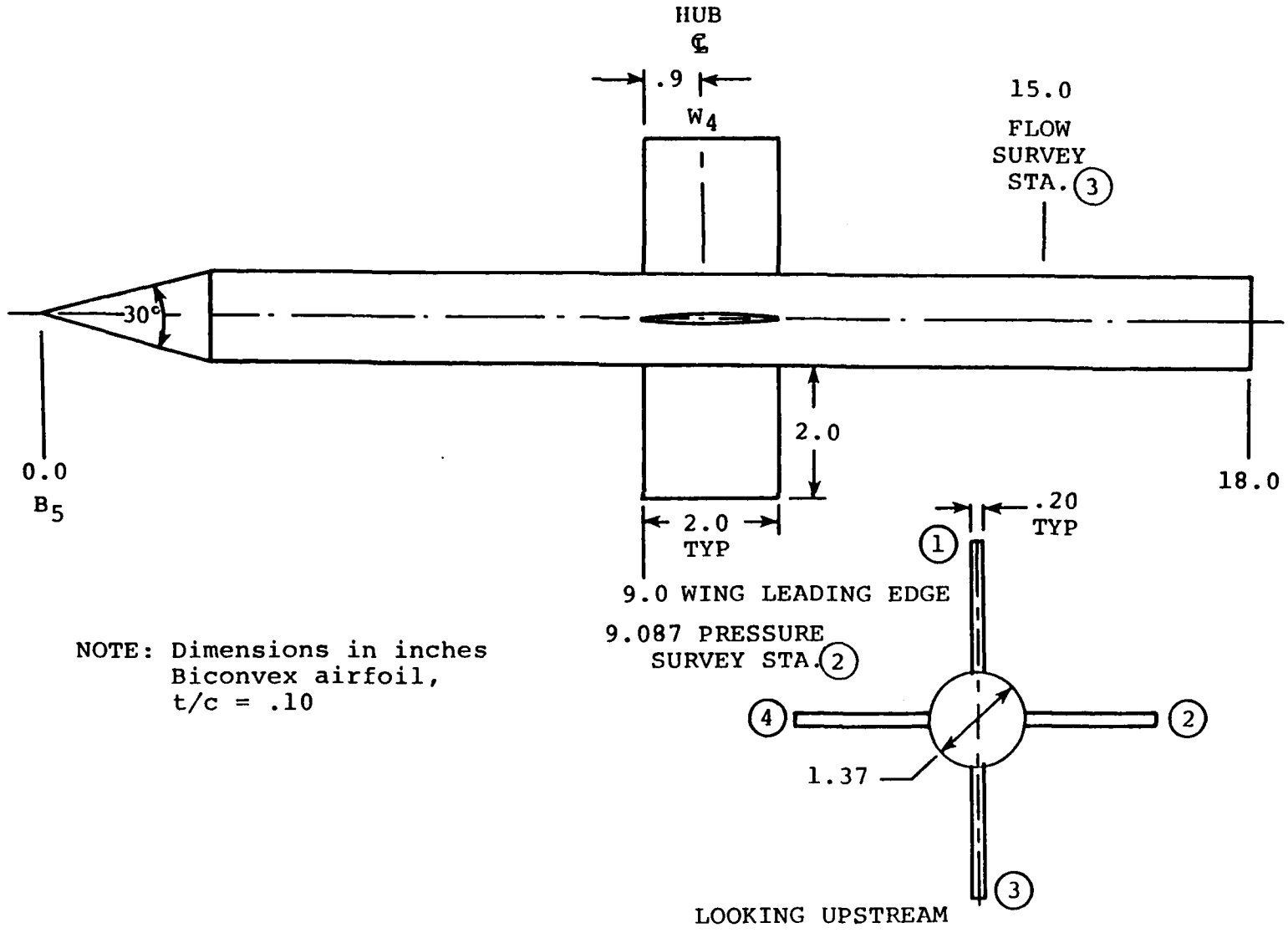

Figure 13.- Rectangular wing-body combination for which flow field surveys made in Bumblebee program.

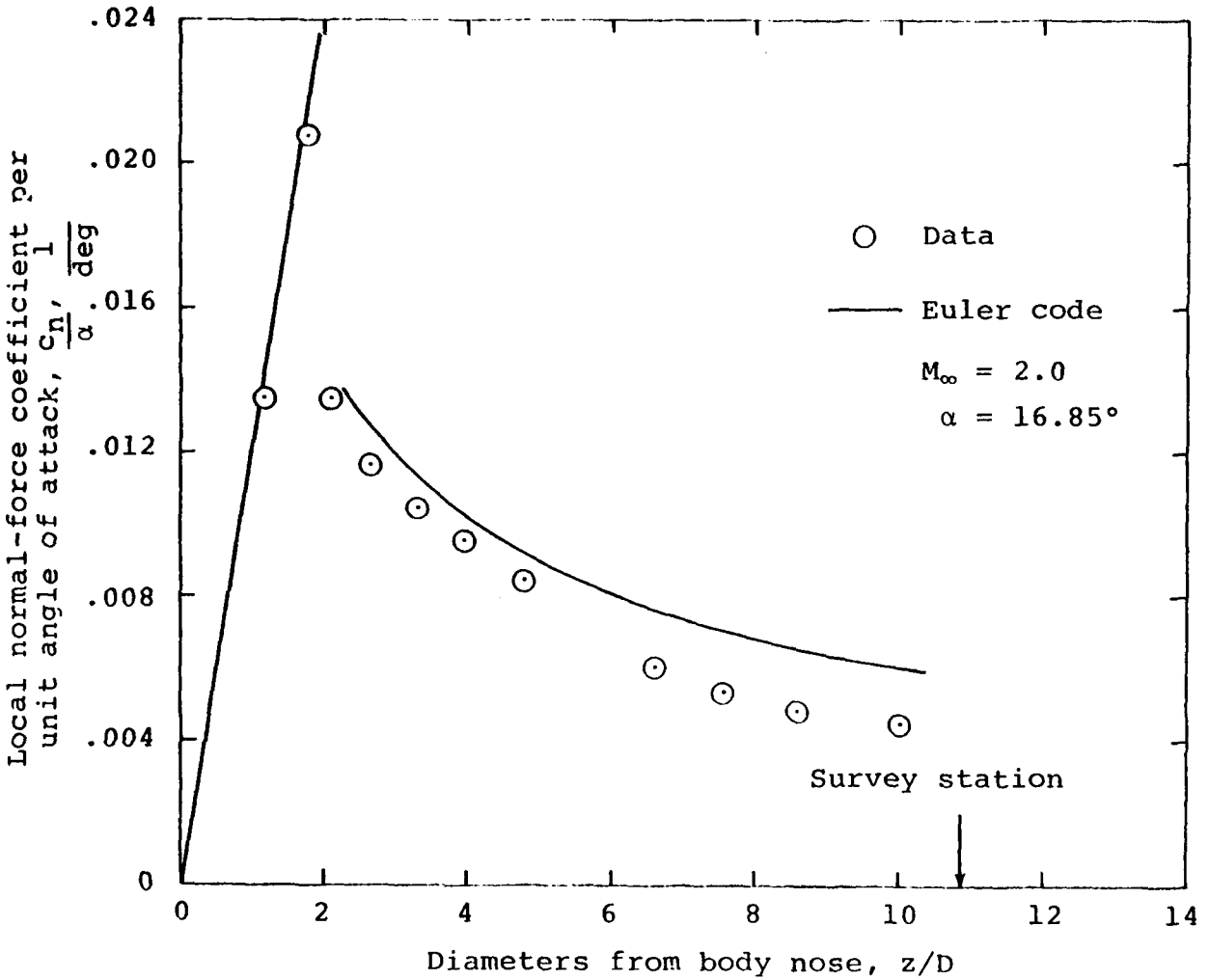

Figure 14.- Axial distribution of local normal-force coefficient per unit angle of attack for Bumblebee body as measured and as predicted by Euler code.

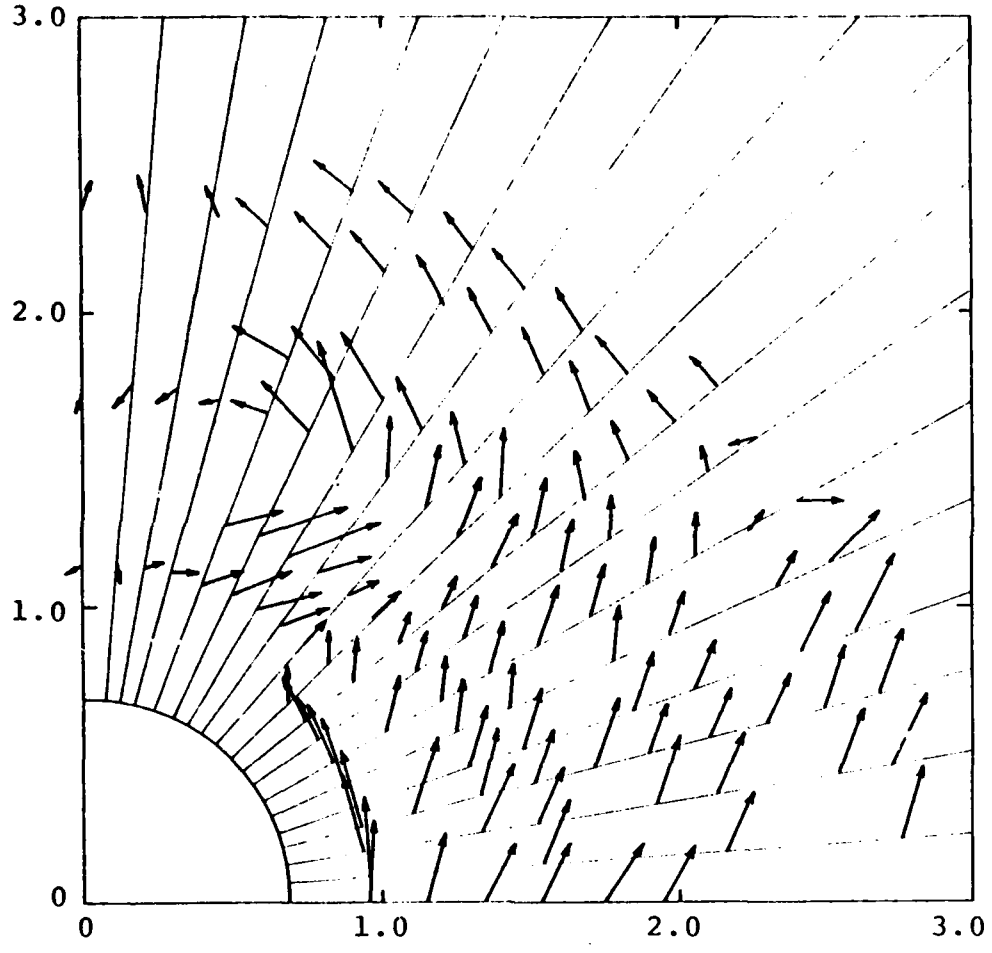

Figure 15.- Measured flow inclination distribution in the wake of a planar wing on a cone-cylinder body; $M_\infty = 2.0$, $\alpha = 16°$, $z/D = 10.95$.

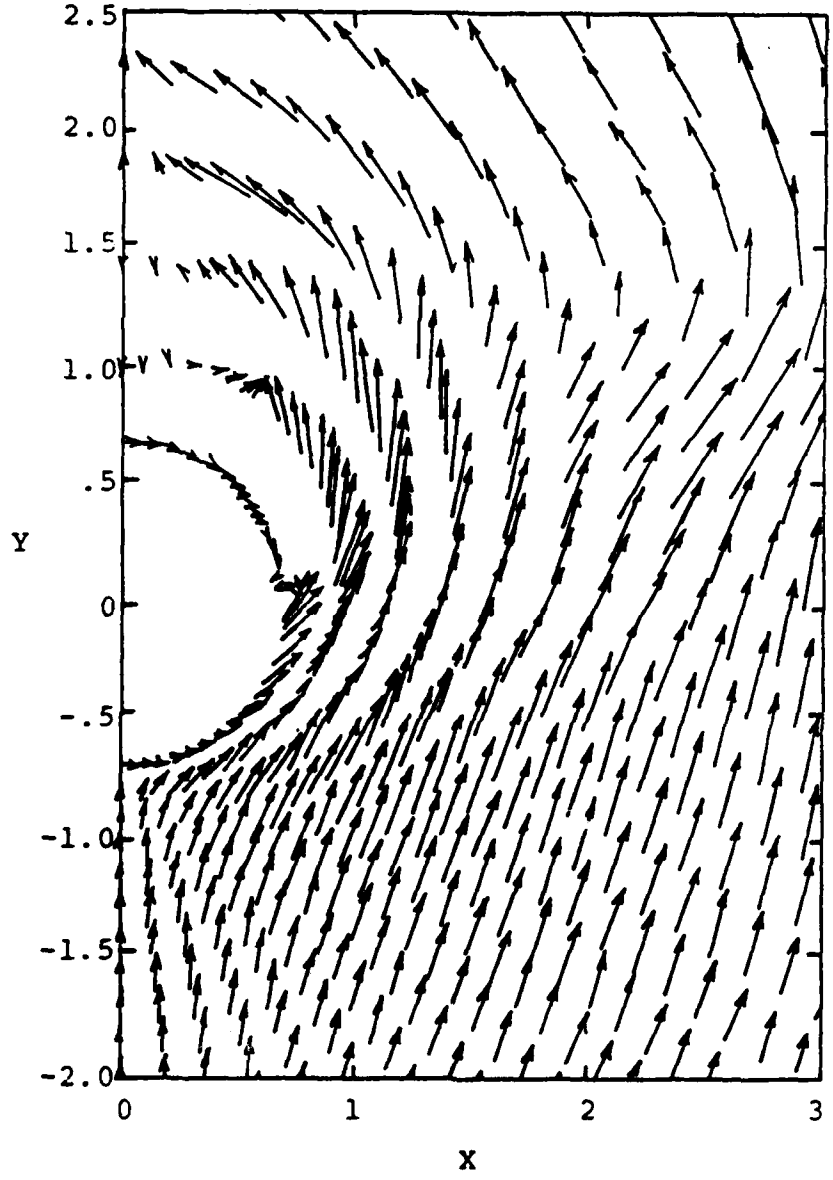

Figure 16.- Calculated flow inclination distribution in wake of a planar wing on a cone-cylinder body; M = 2.0, α = 16°, Z/D = 10.95.

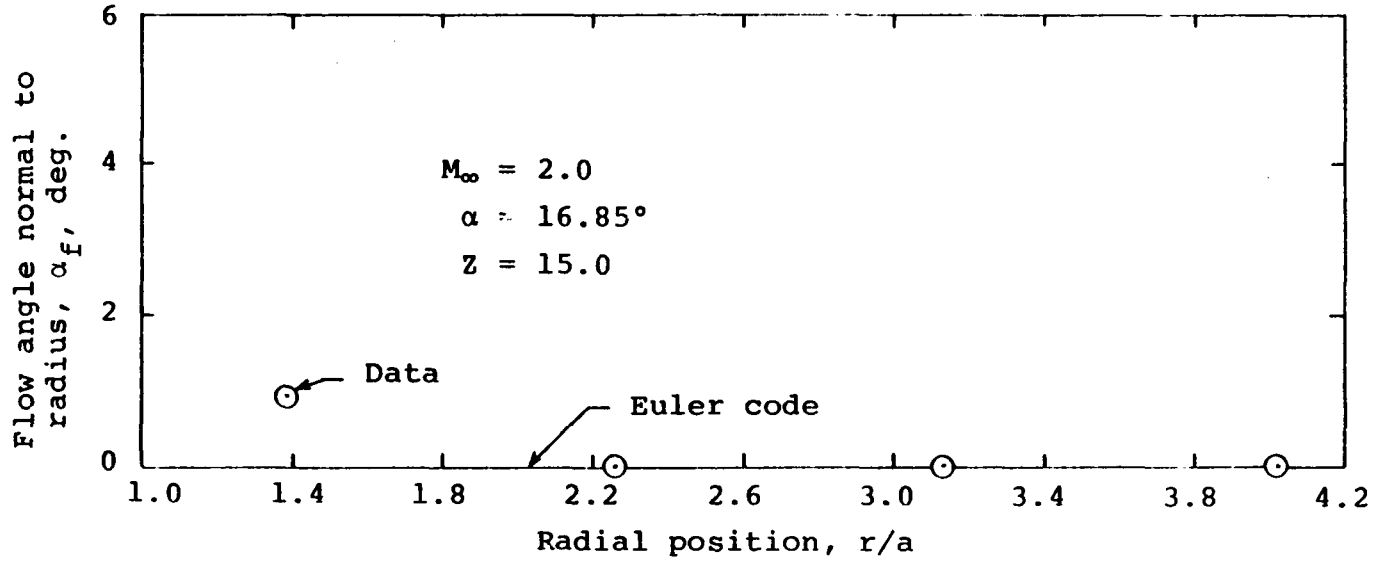

(a) $\phi = 0°$

Figure 17.- Comparison of flow angle normal to radius as measured and as calculated from Euler code for cone-cylinder body.

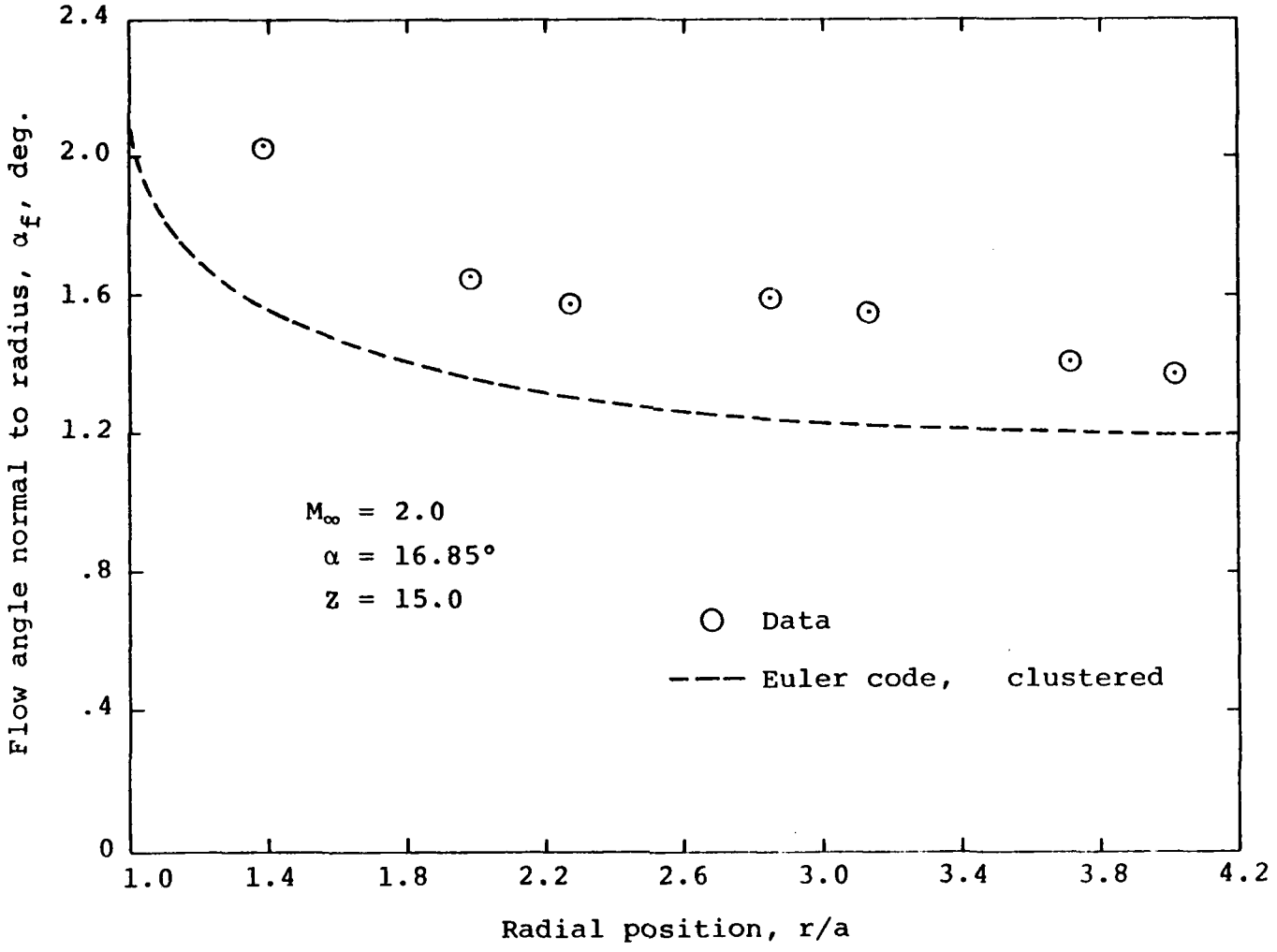

(b) $\phi \approx 45°$

Figure 17.- Continued.

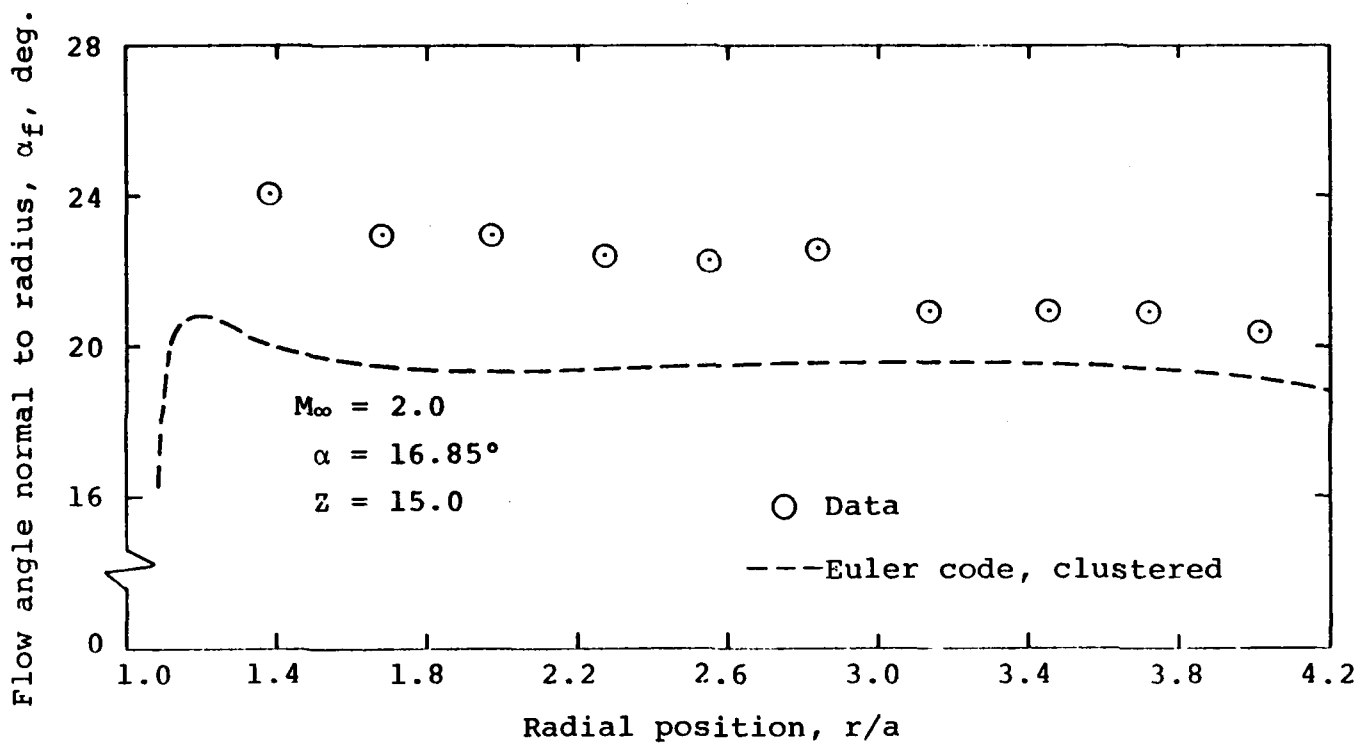

(c) ϕ = 90°

Figure 17.- Continued.

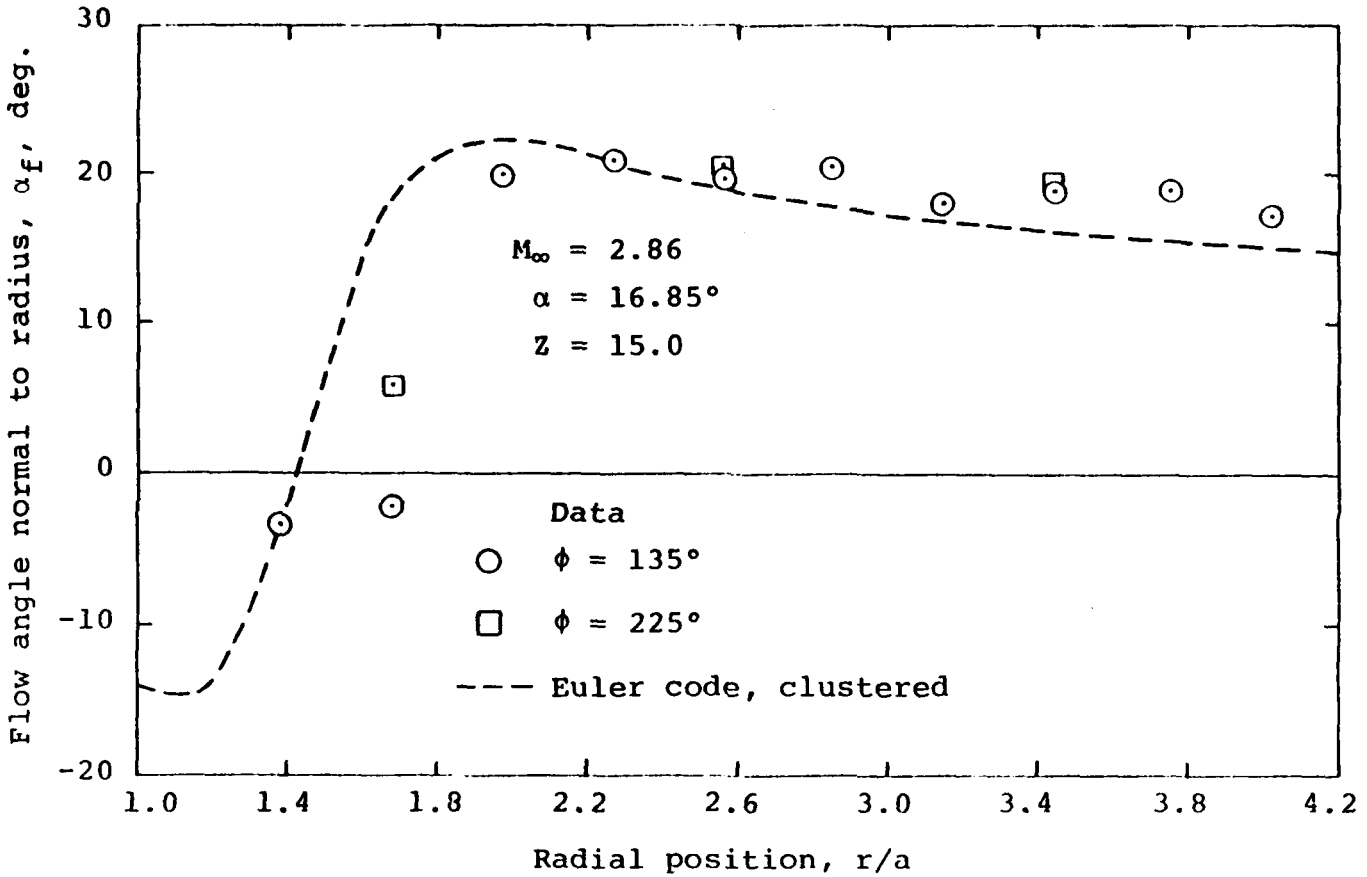

(d) ϕ = 135° and 225°

Figure 17.- Continued.

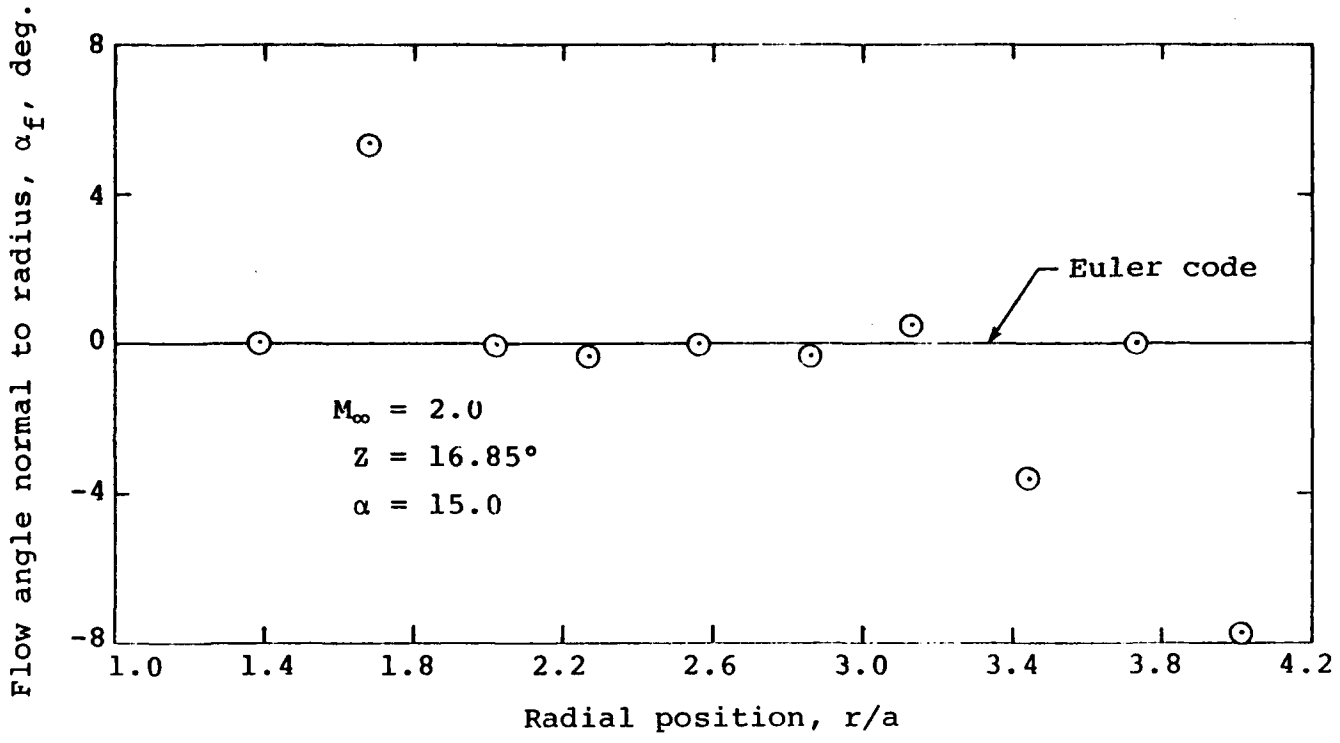

(e) ϕ = 180°

Figure 17.- Concluded.

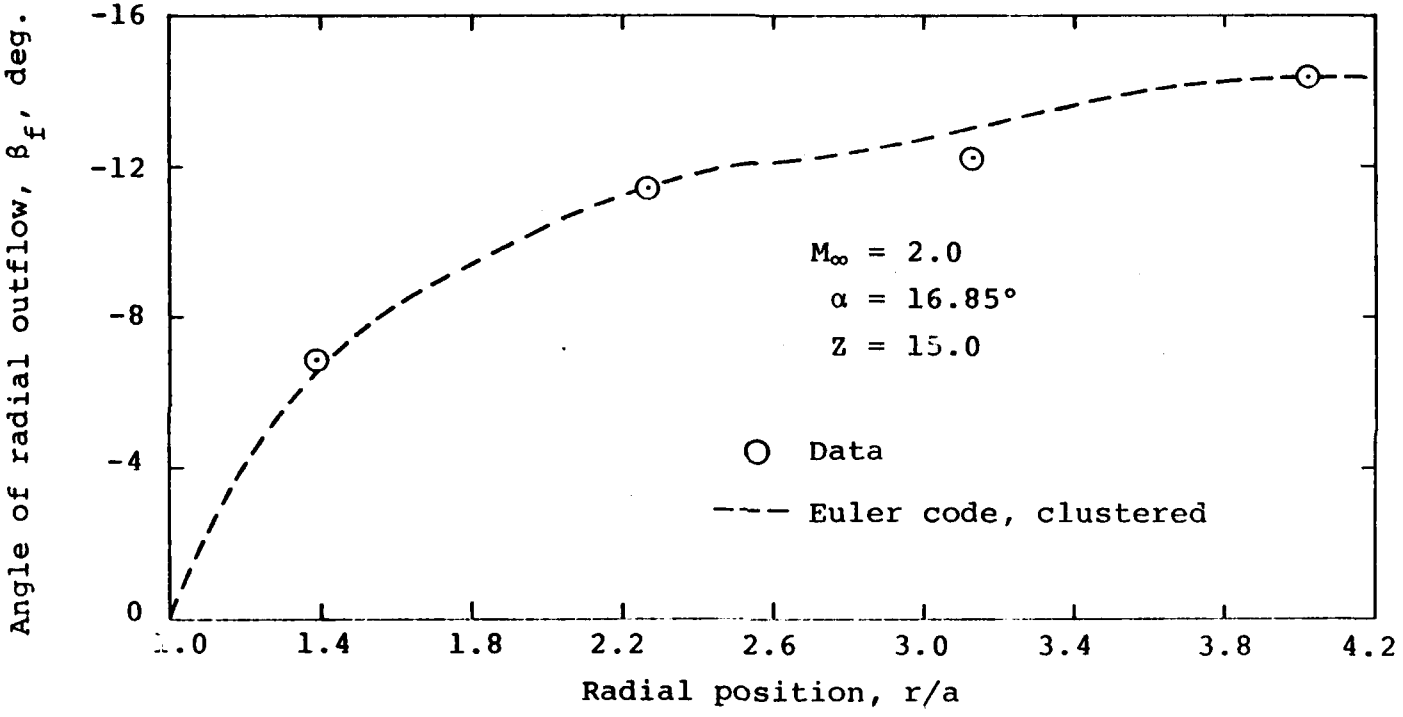

(a) $\phi = 0°$

Figure 18.- Comparison of angle of radial outflow as measured and as calculated by an Euler code for ogive-cylinder body.

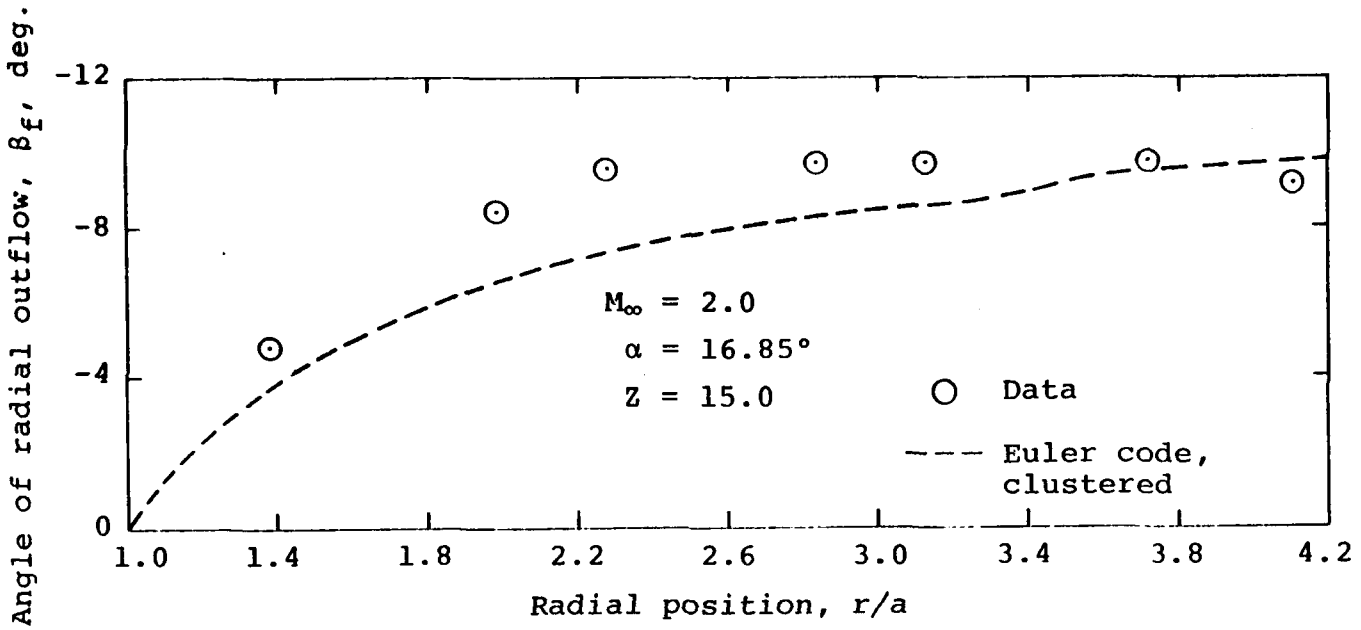

(b) $\phi \approx 45°$

Figure 18.- Continued.

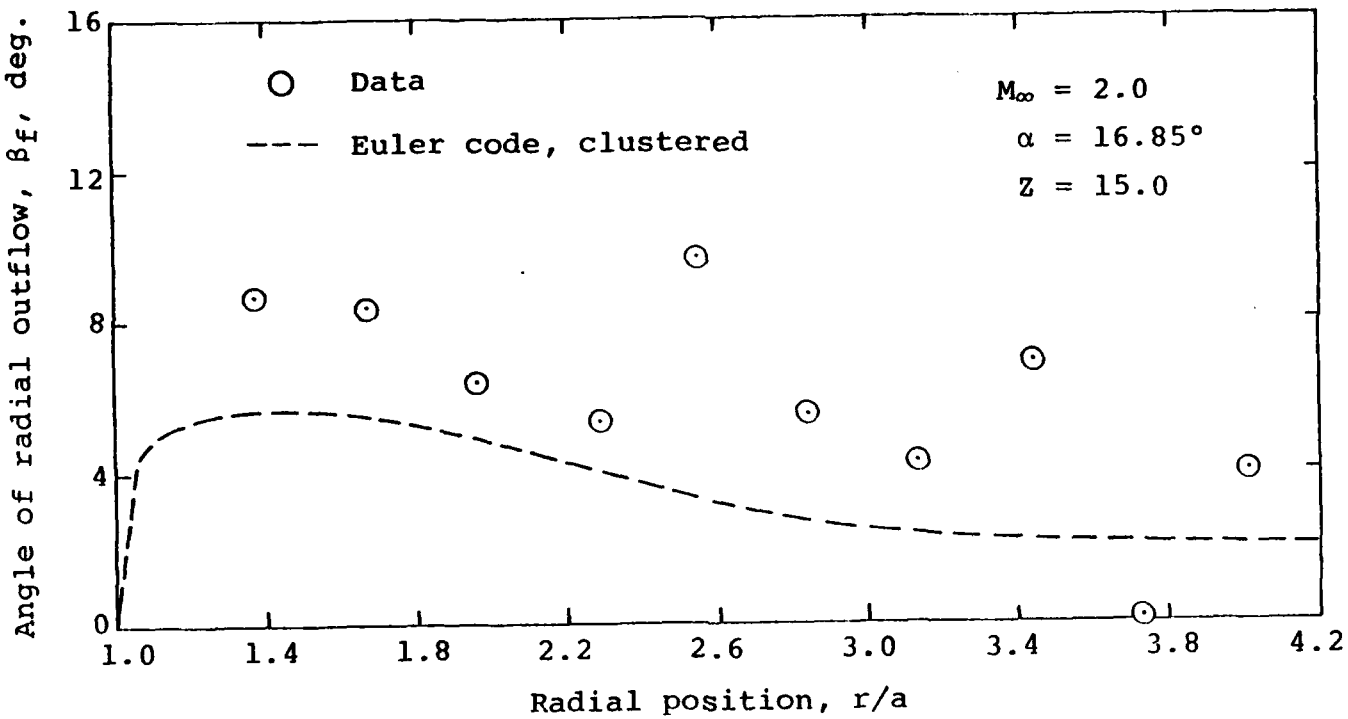

(c) ϕ = 90°

Figure 18.- Continued.

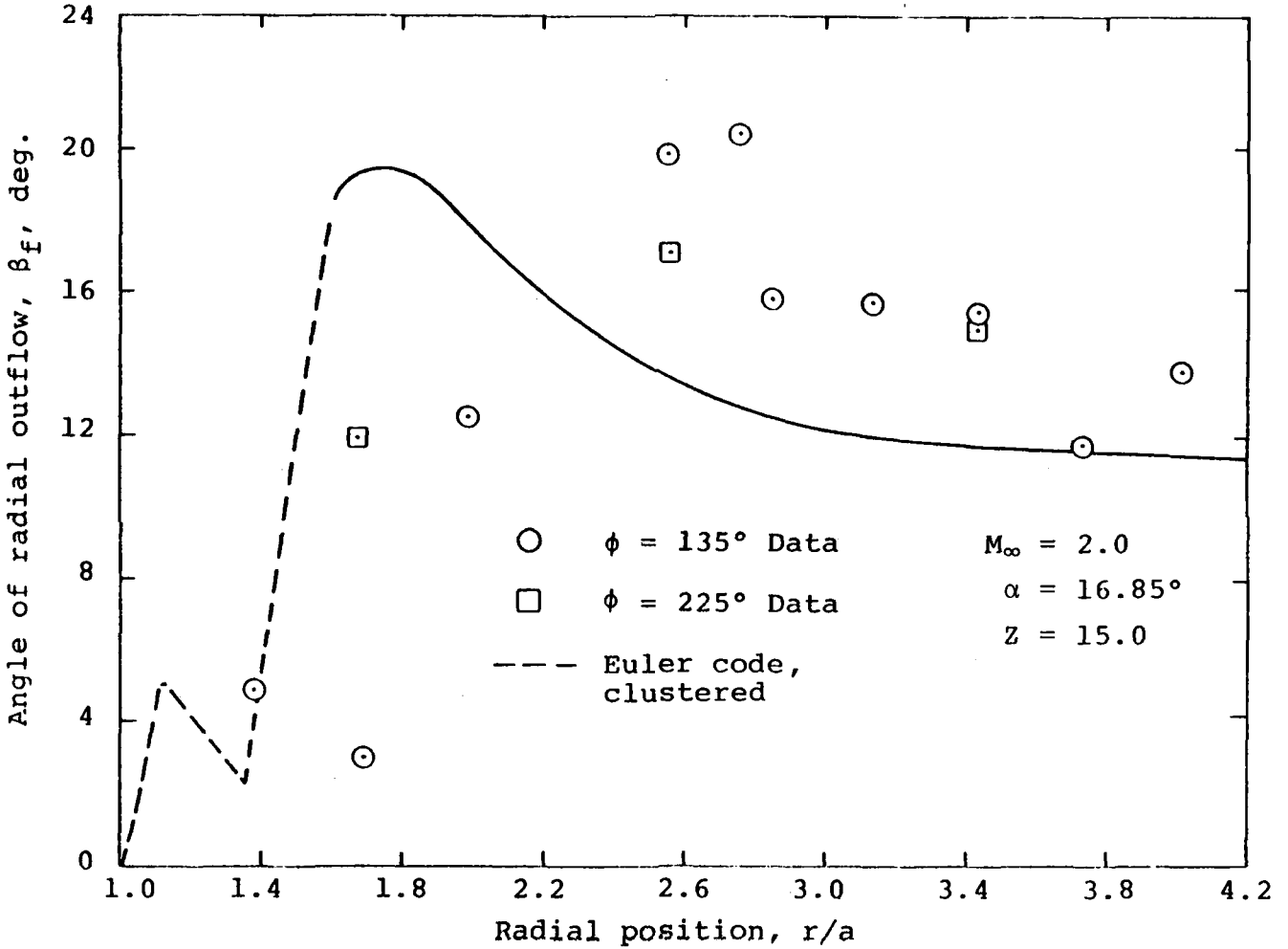

(d) ϕ = 135° and 225°

Figure 18.- Continued.

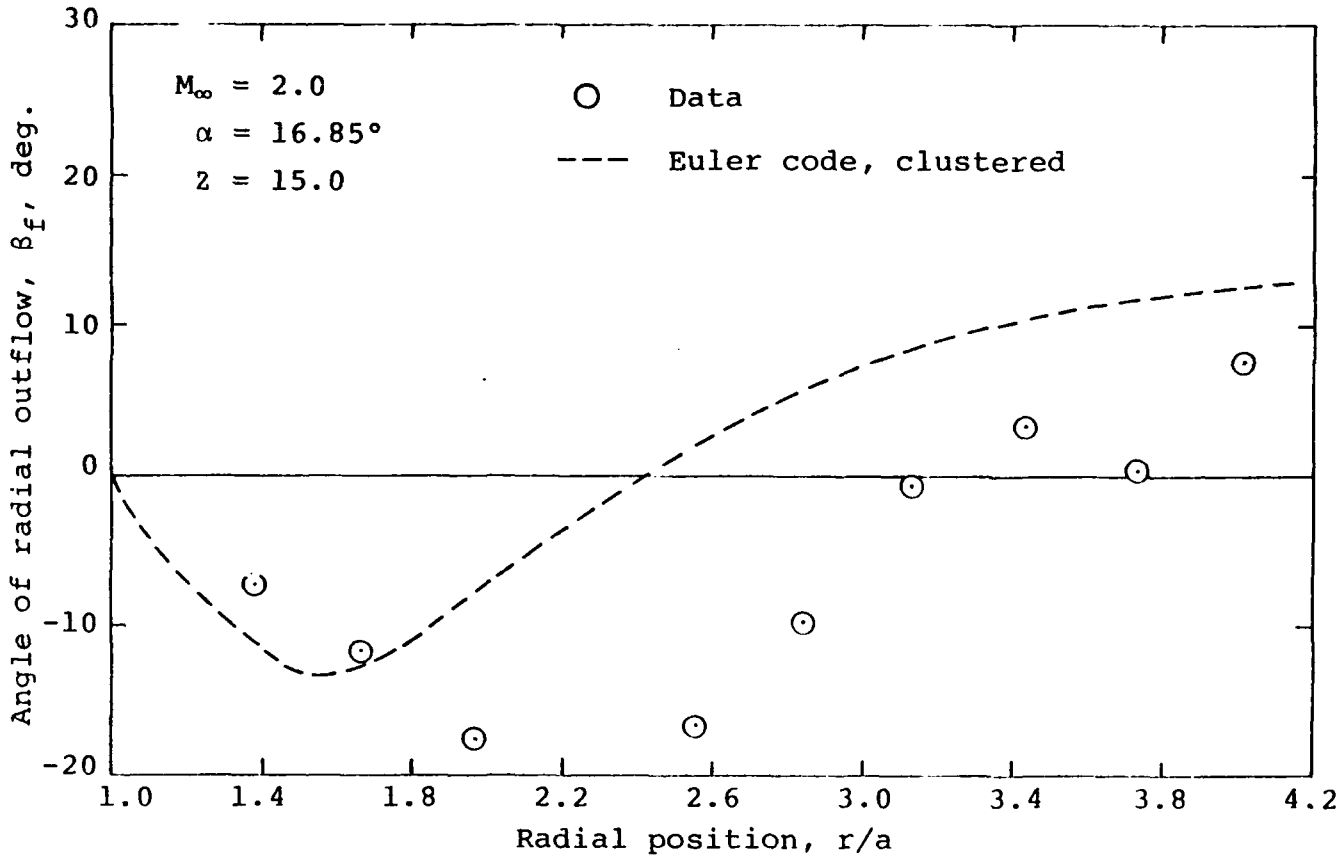

(e) ϕ = 180°

Figure 18.- Concluded.

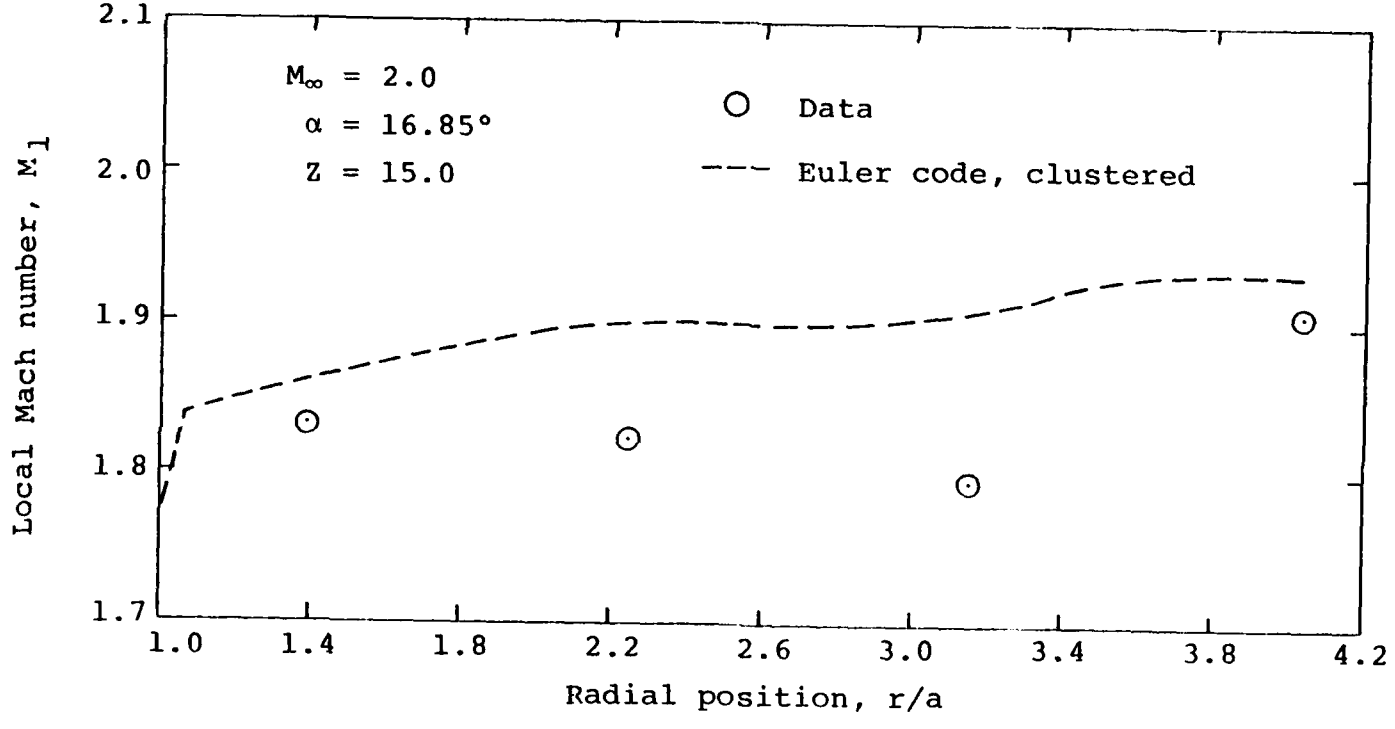

(a) $\phi = 0°$

Figure 19.- Comparison of local Mach number as measured and as calculated from Euler code for cone-cylinder body.

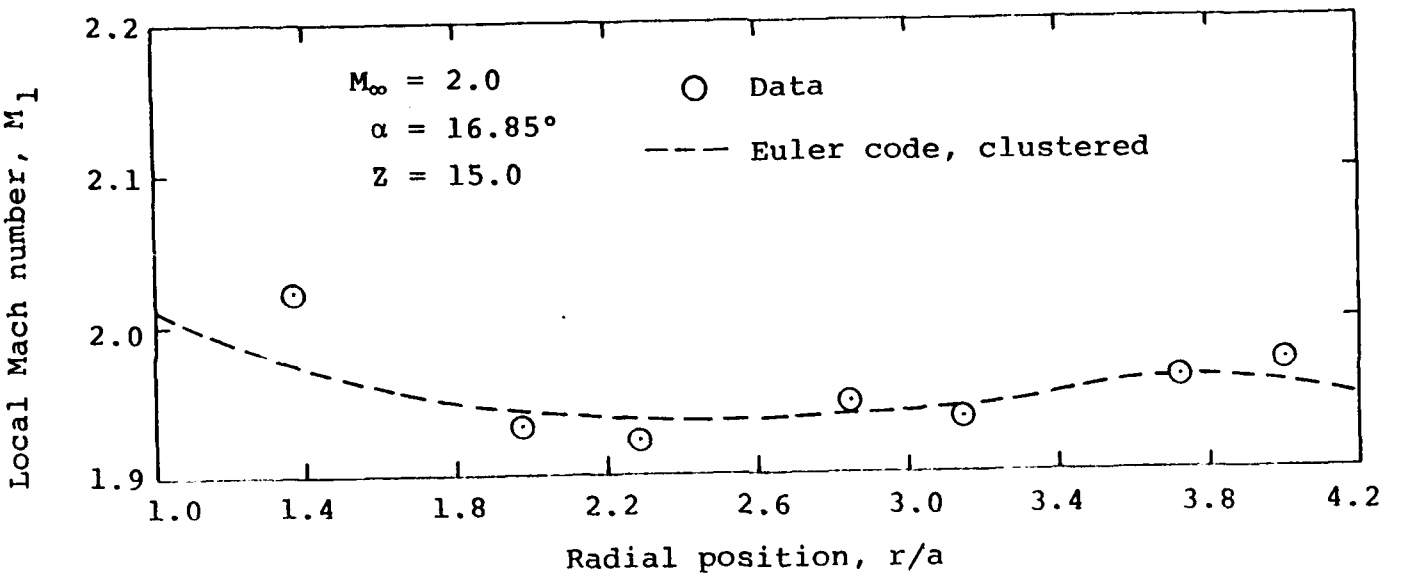

(b) ϕ = 45°

Figure 19.- Concluded.

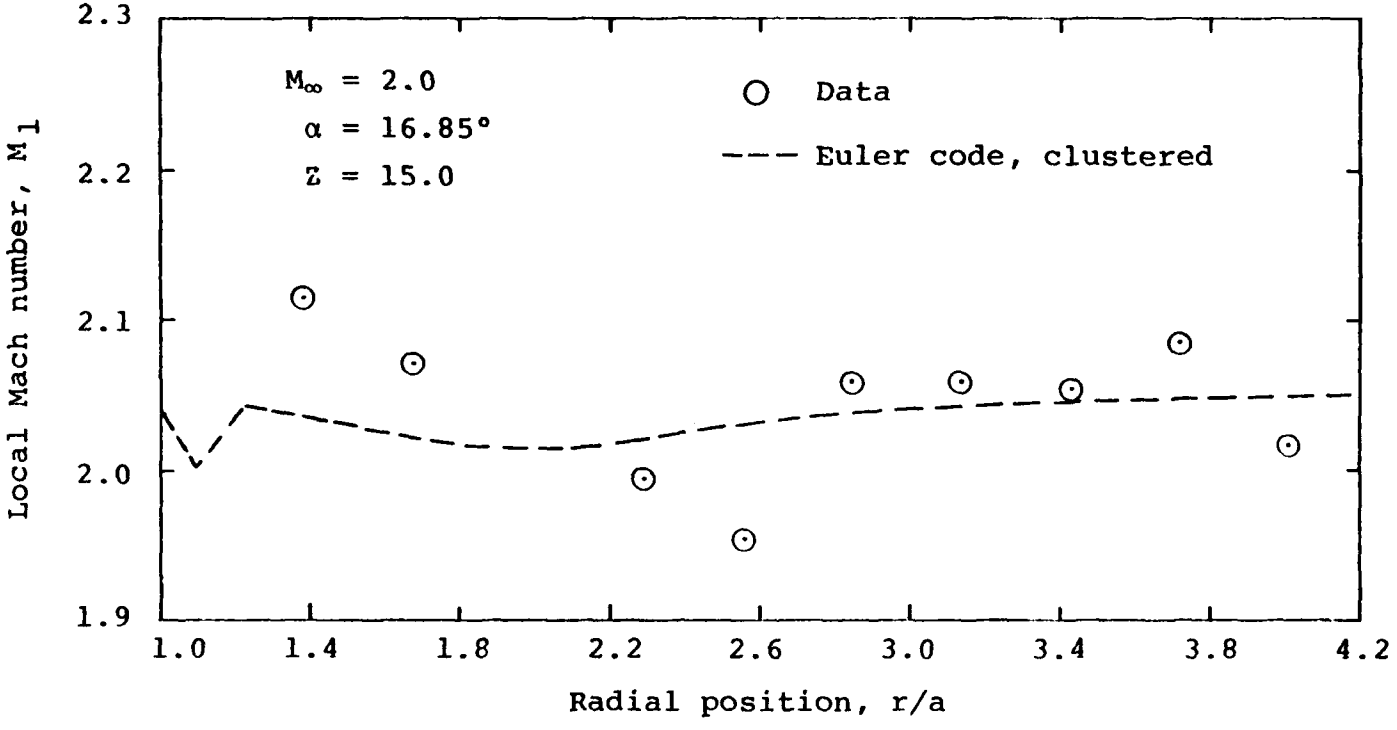

(c) ϕ = 90°

Figure 19.- Continued.

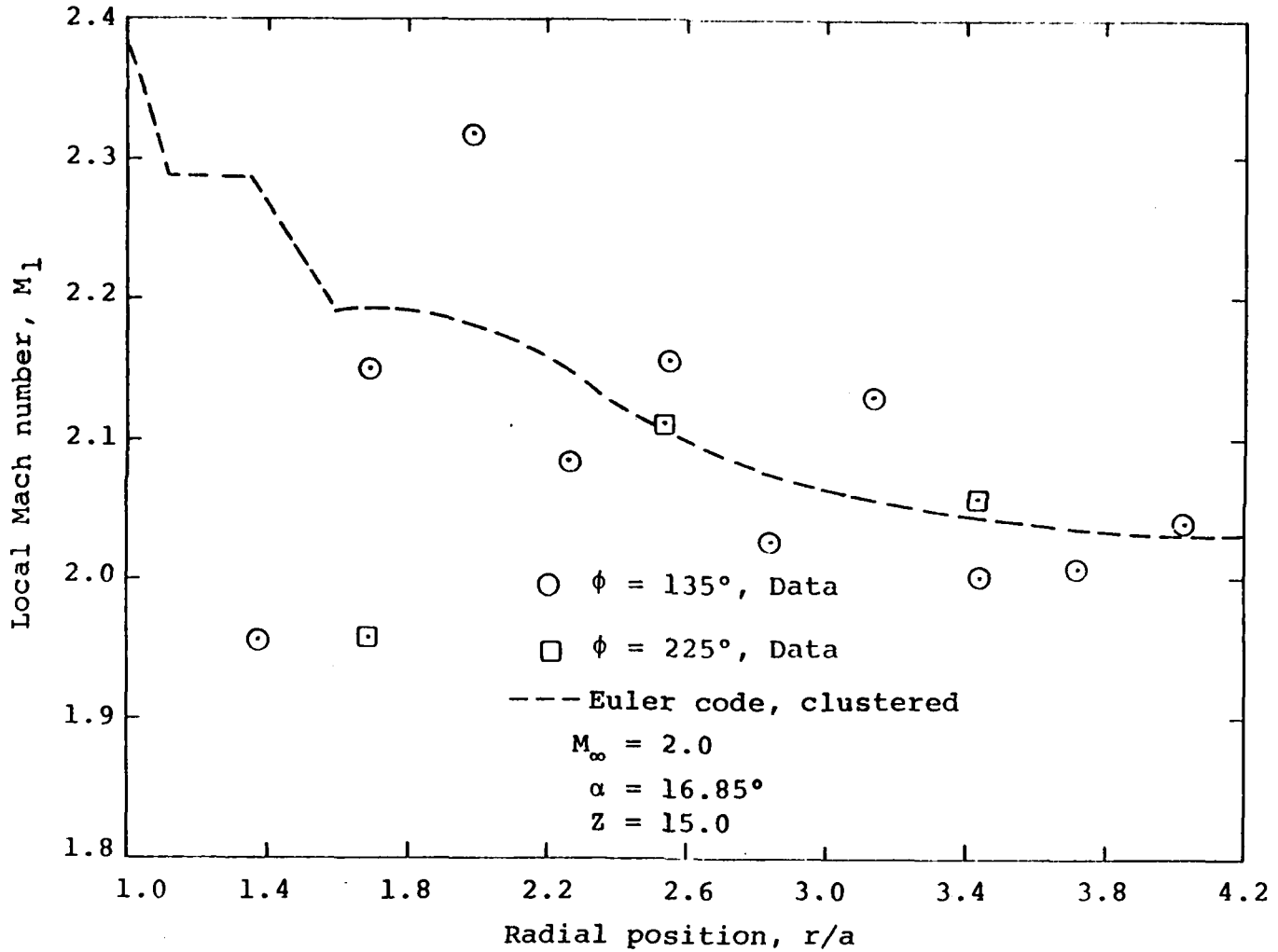

(d) ϕ = 135° and 225°

Figure 19.- Continued.

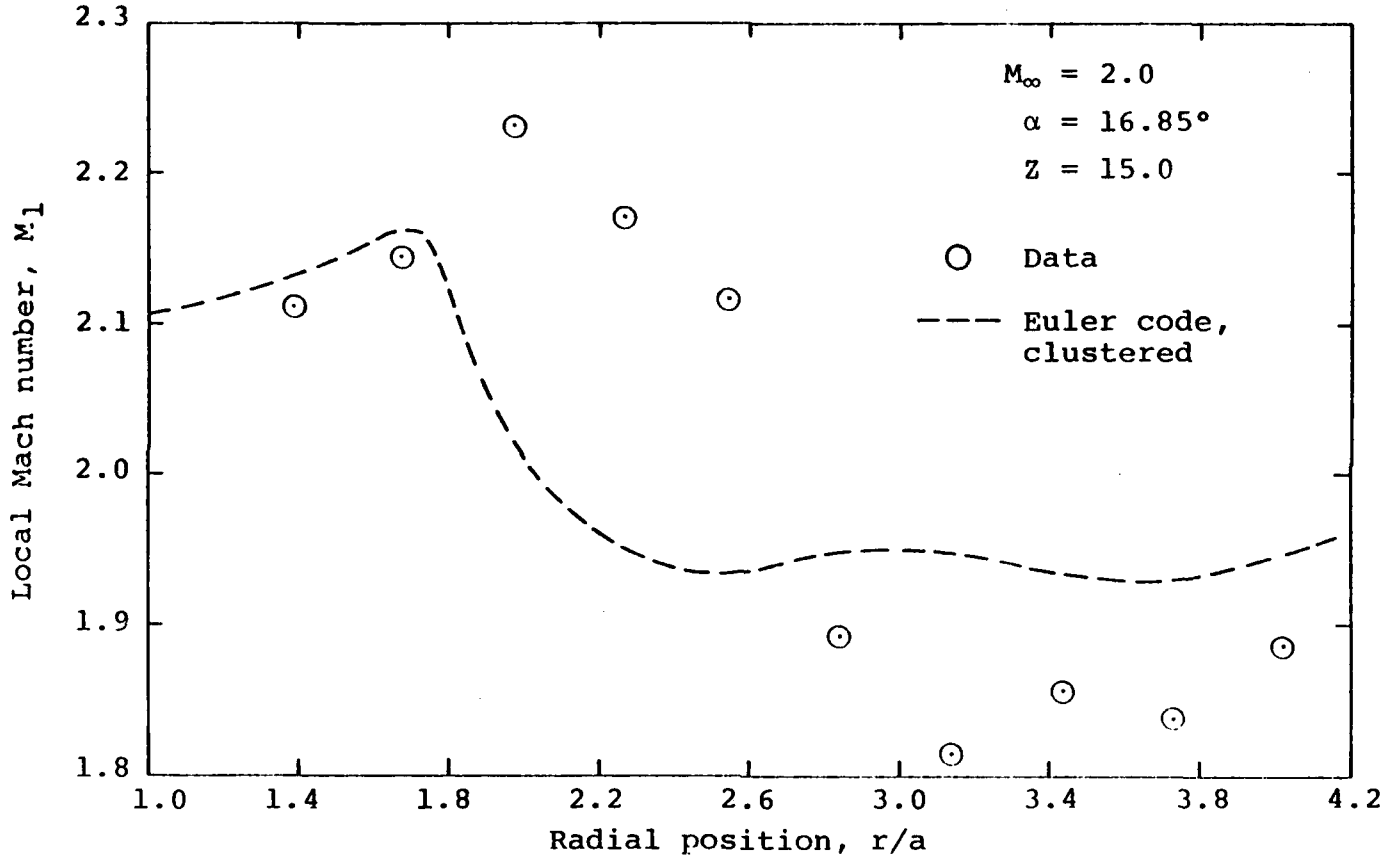

(e) ϕ = 180°

Figure 19.- Concluded.

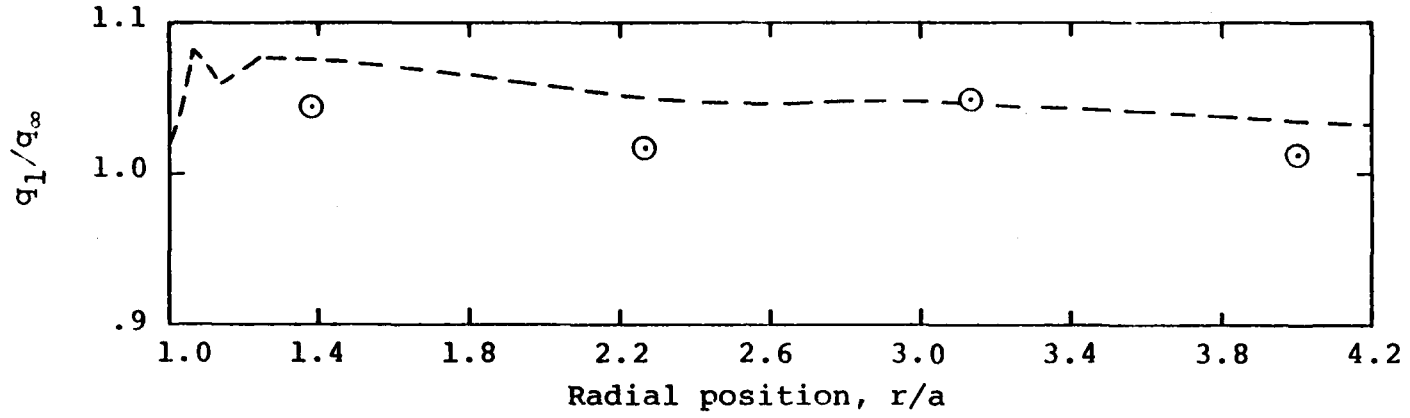

(a) $\phi = 0°$

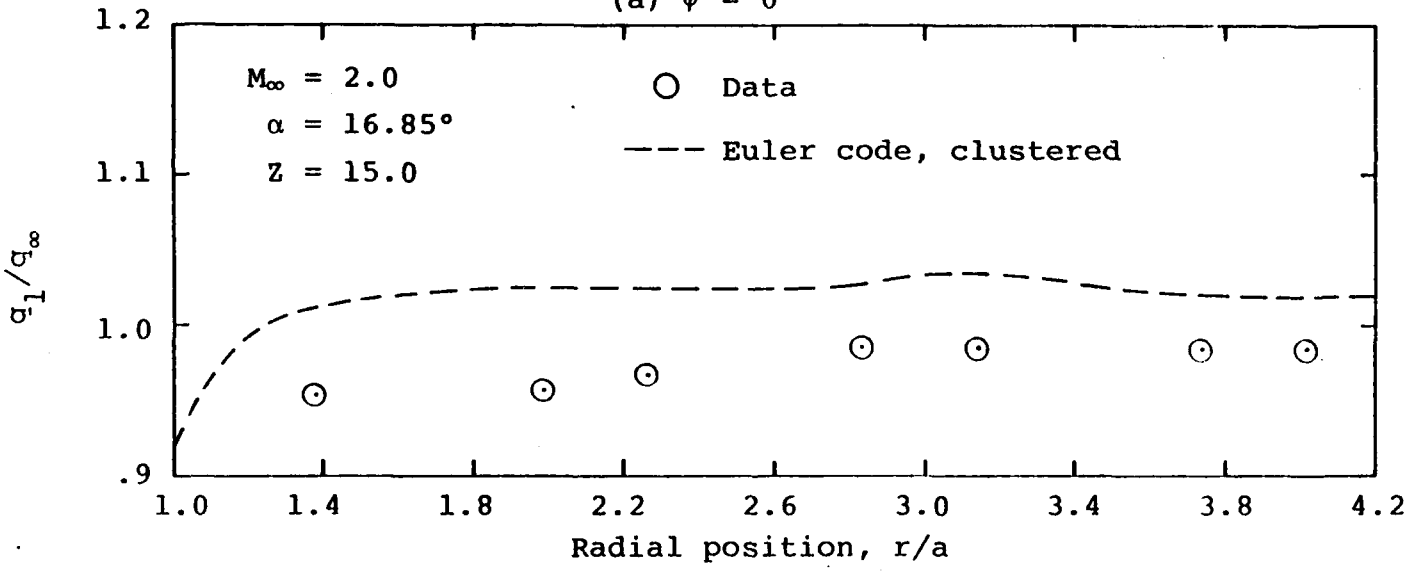

(b) $\phi = 45°$

Figure 20.- Comparison of local dynamic pressure ratio as measured and as calculated from Euler code for cone-cylinder body.

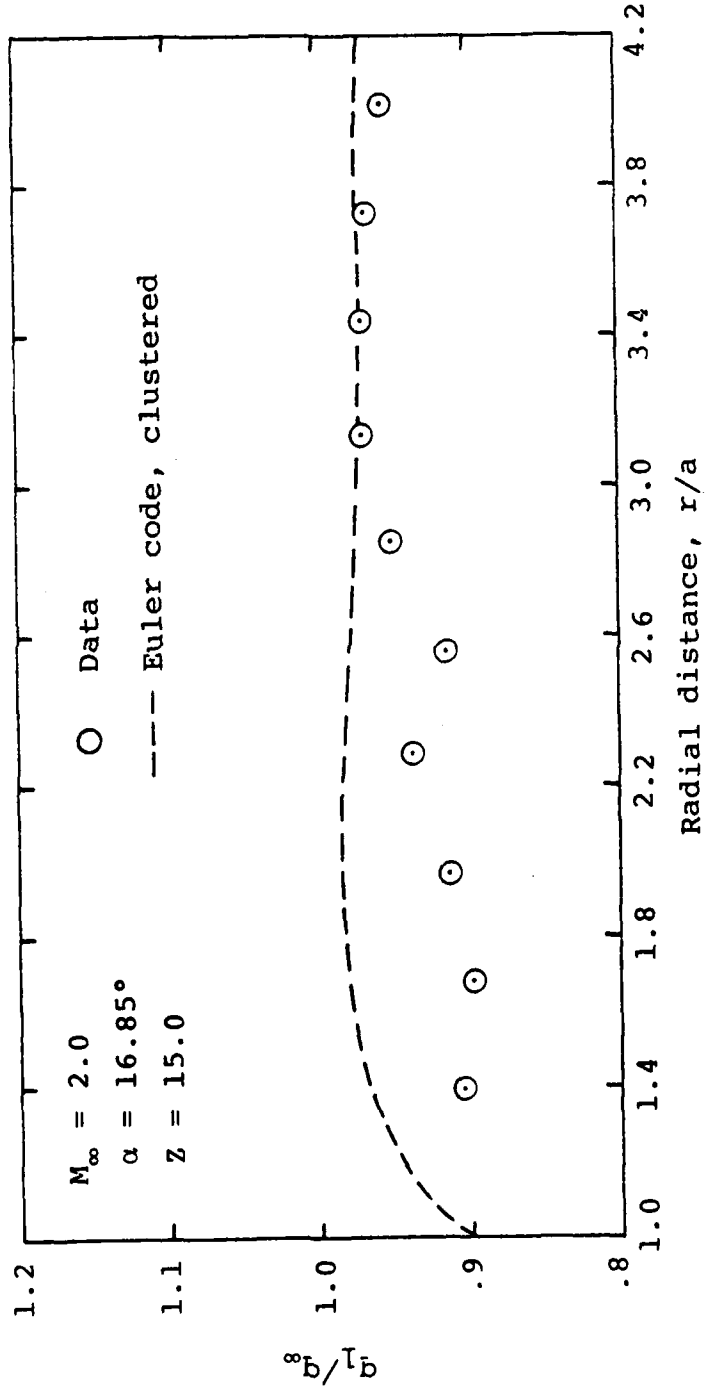

(c) $\phi = 90°$

Figure 20.- Continued.

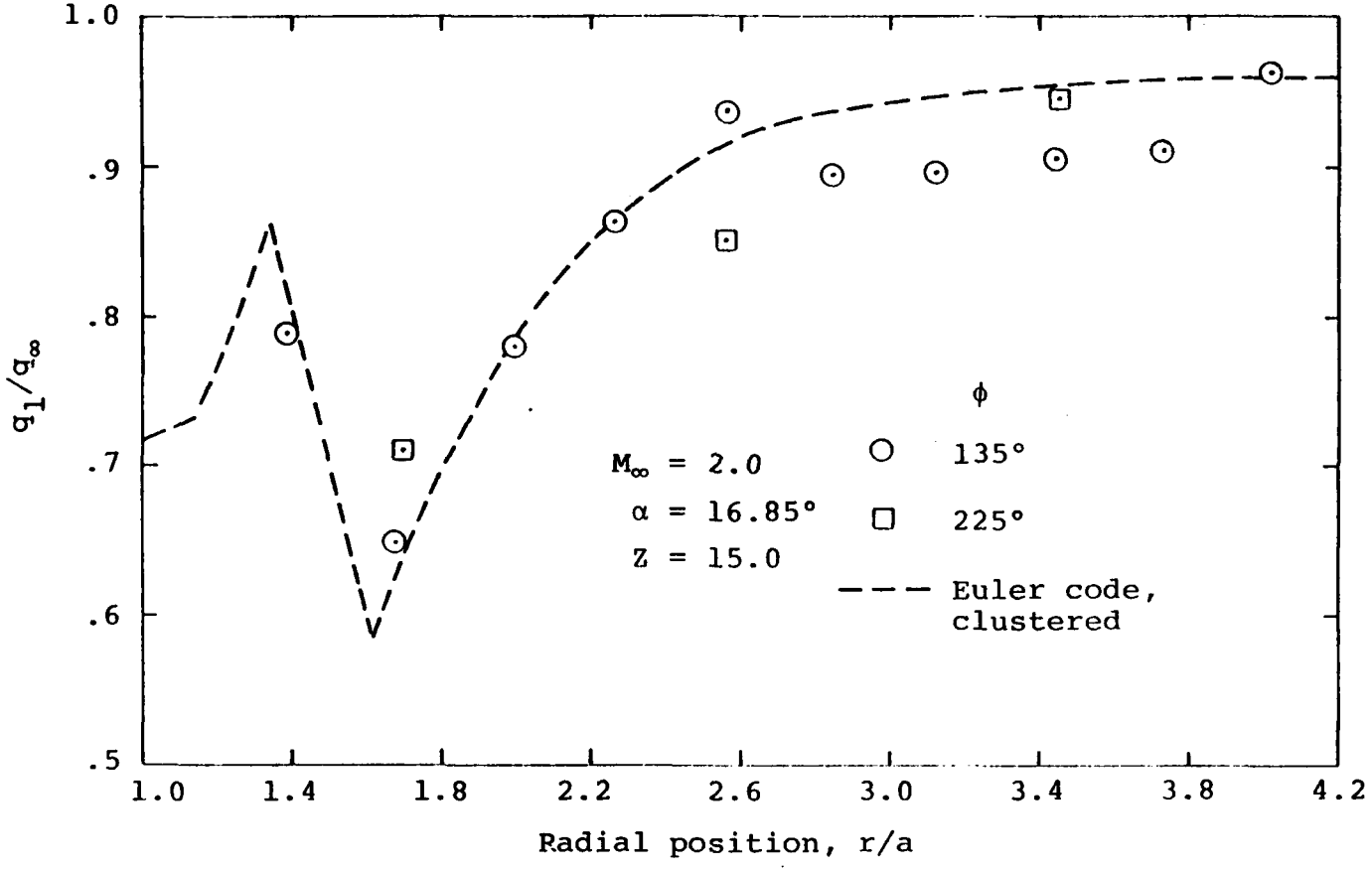

(d) ϕ = 135° and 225°

Figure 20.- Continued.

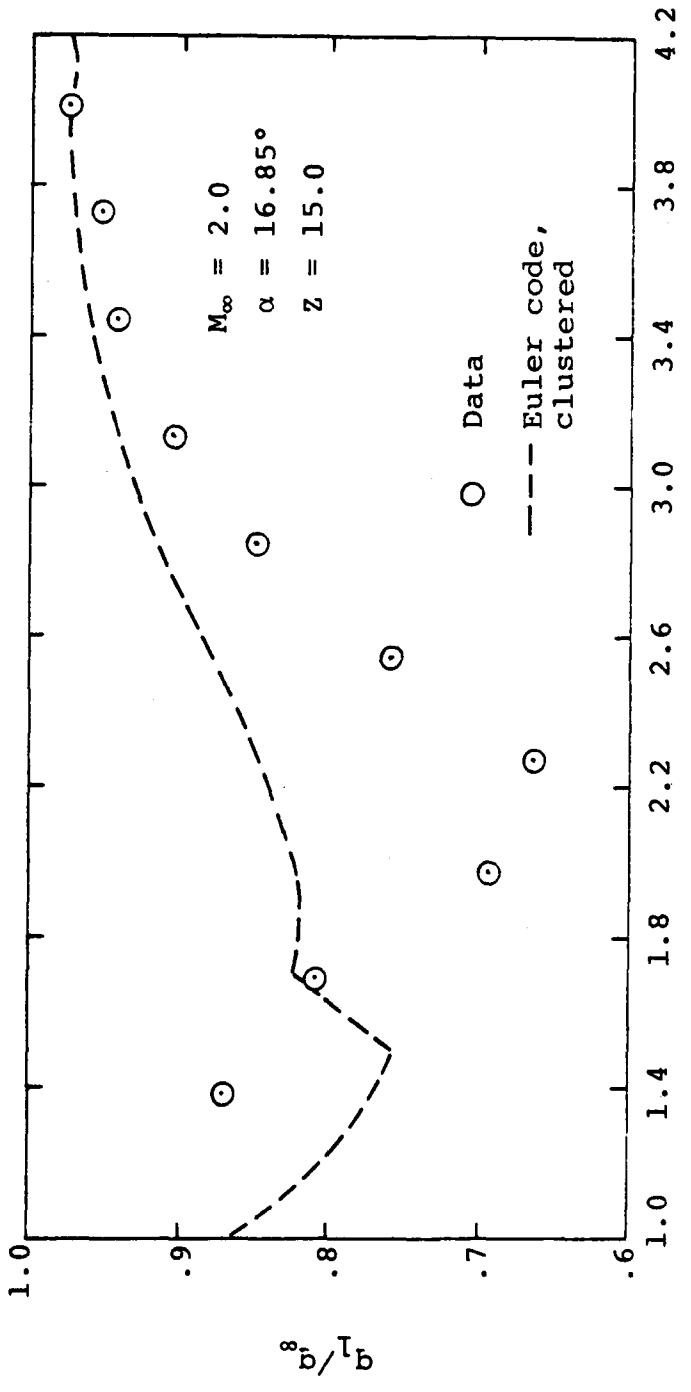

(e) ϕ = 180°

Figure 20.- Concluded.

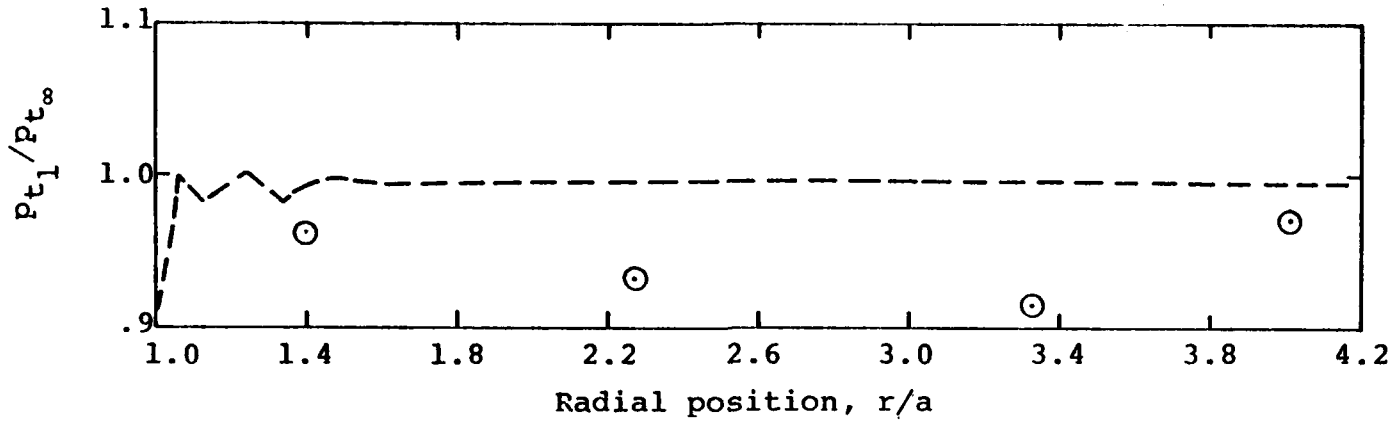

(a) $\phi = 0°$

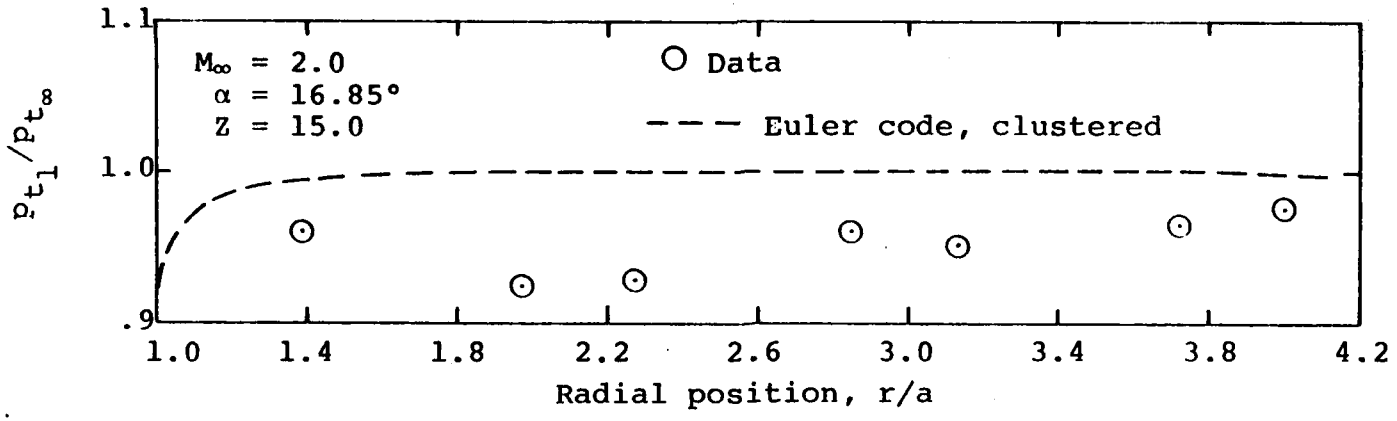

(b) $\phi = 45°$

Figure 21.- Comparison of local total pressure ratio as measured and as calculated from Euler code for cone-cylinder body.

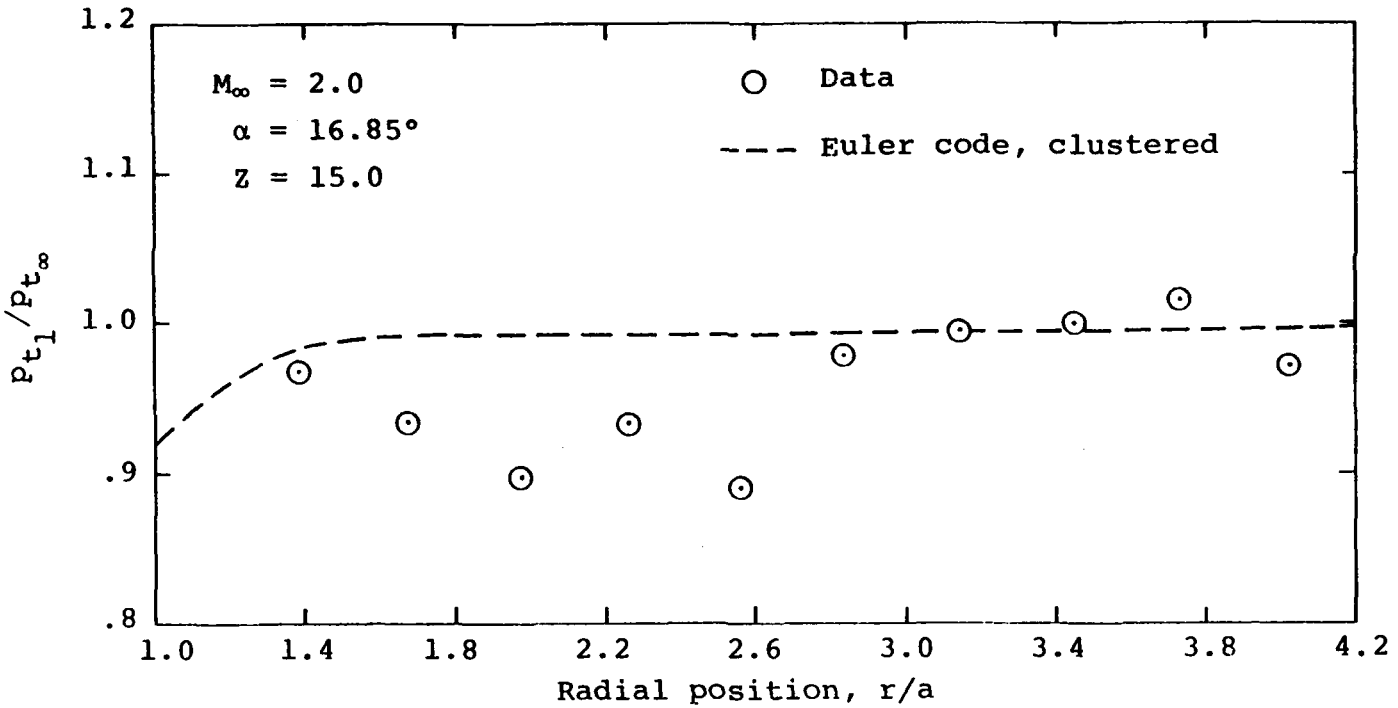

(c) $\phi = 90°$

Figure 21.- Continued.

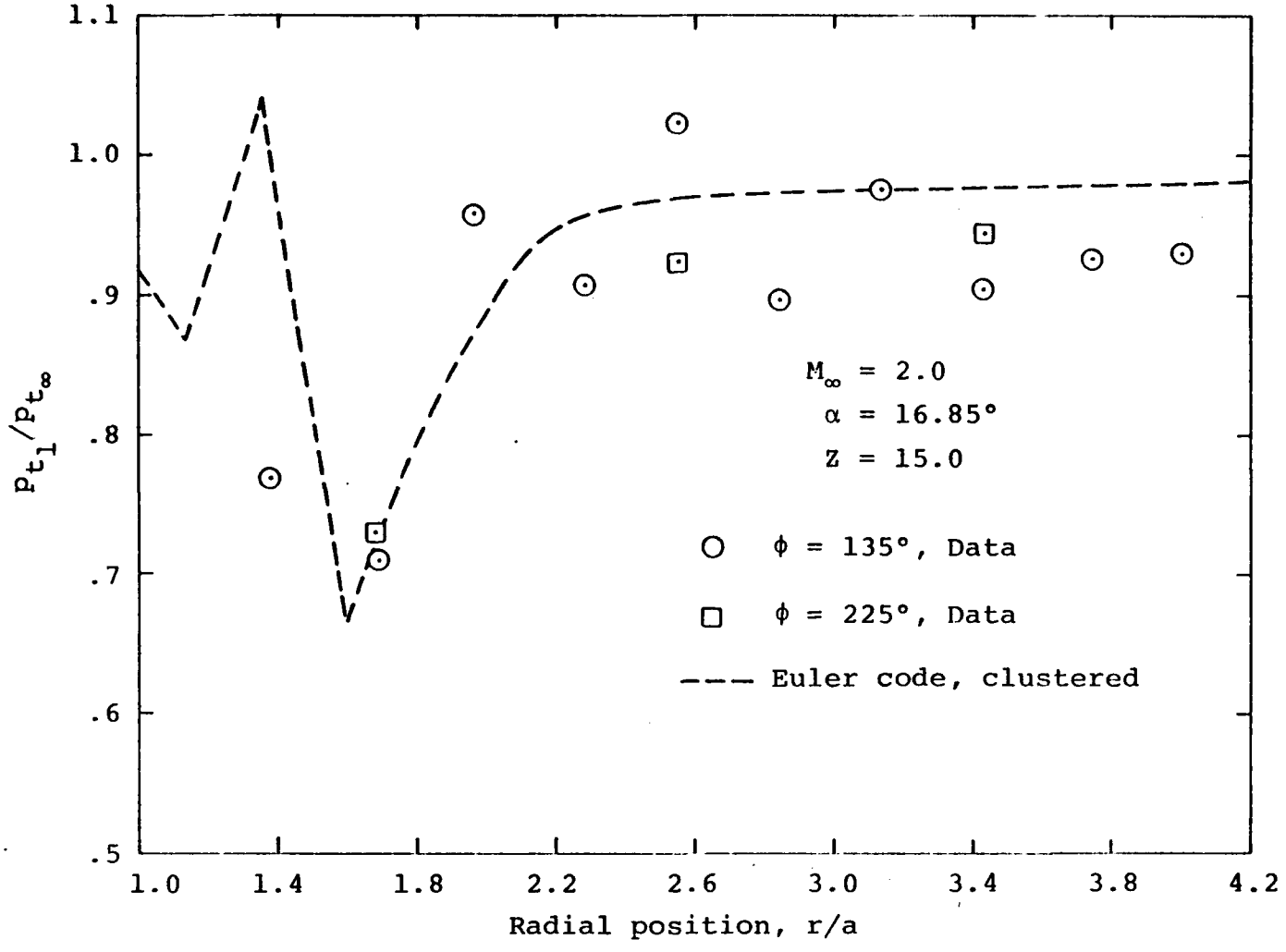

(d) φ = 135° and 225°

Figure 21.- Continued.

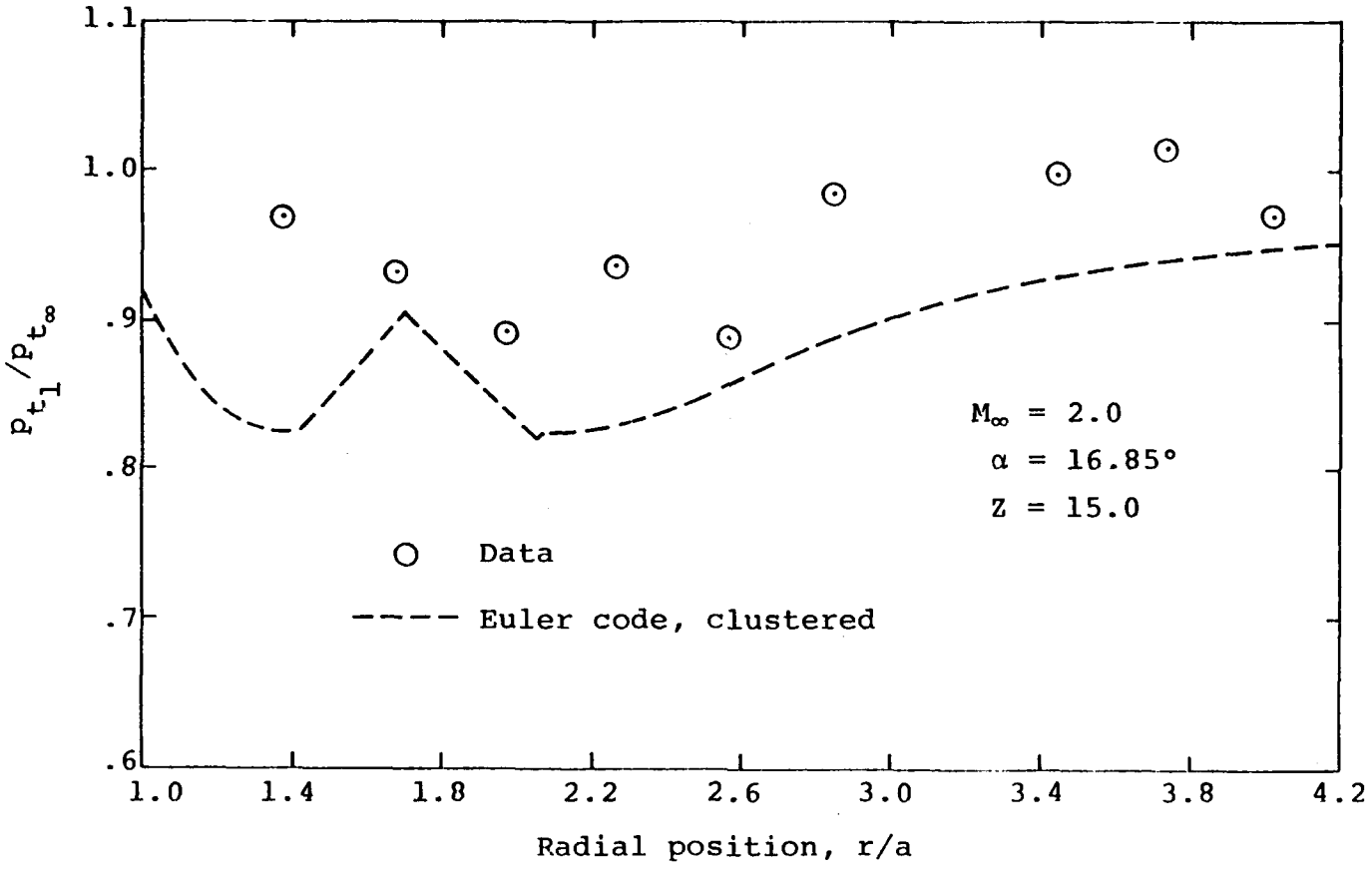

(e) ϕ = 180°

Figure 21.- Concluded.

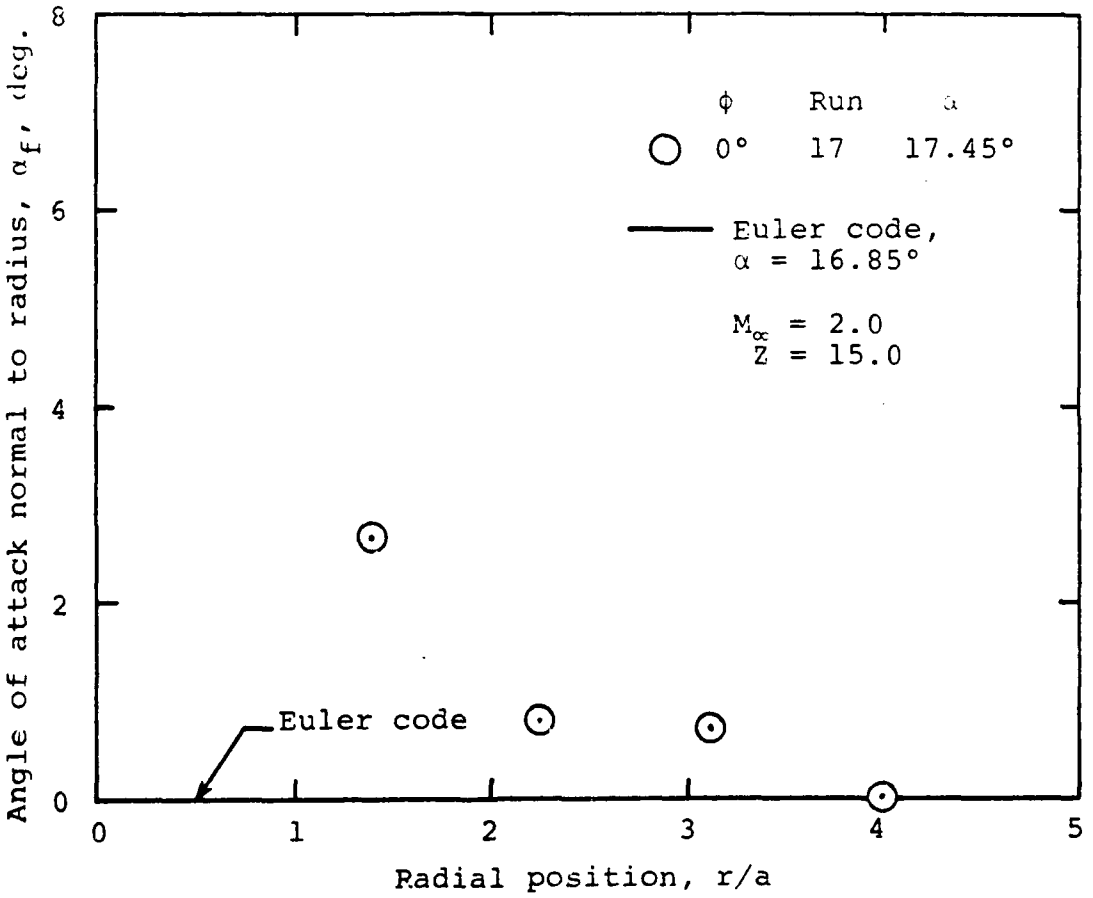

(a) $\phi = 0°$

Figure 22.- Comparison of angle of attack normal to radius as measured and as calculated from Euler code for flow behind wing of wing-body combination.

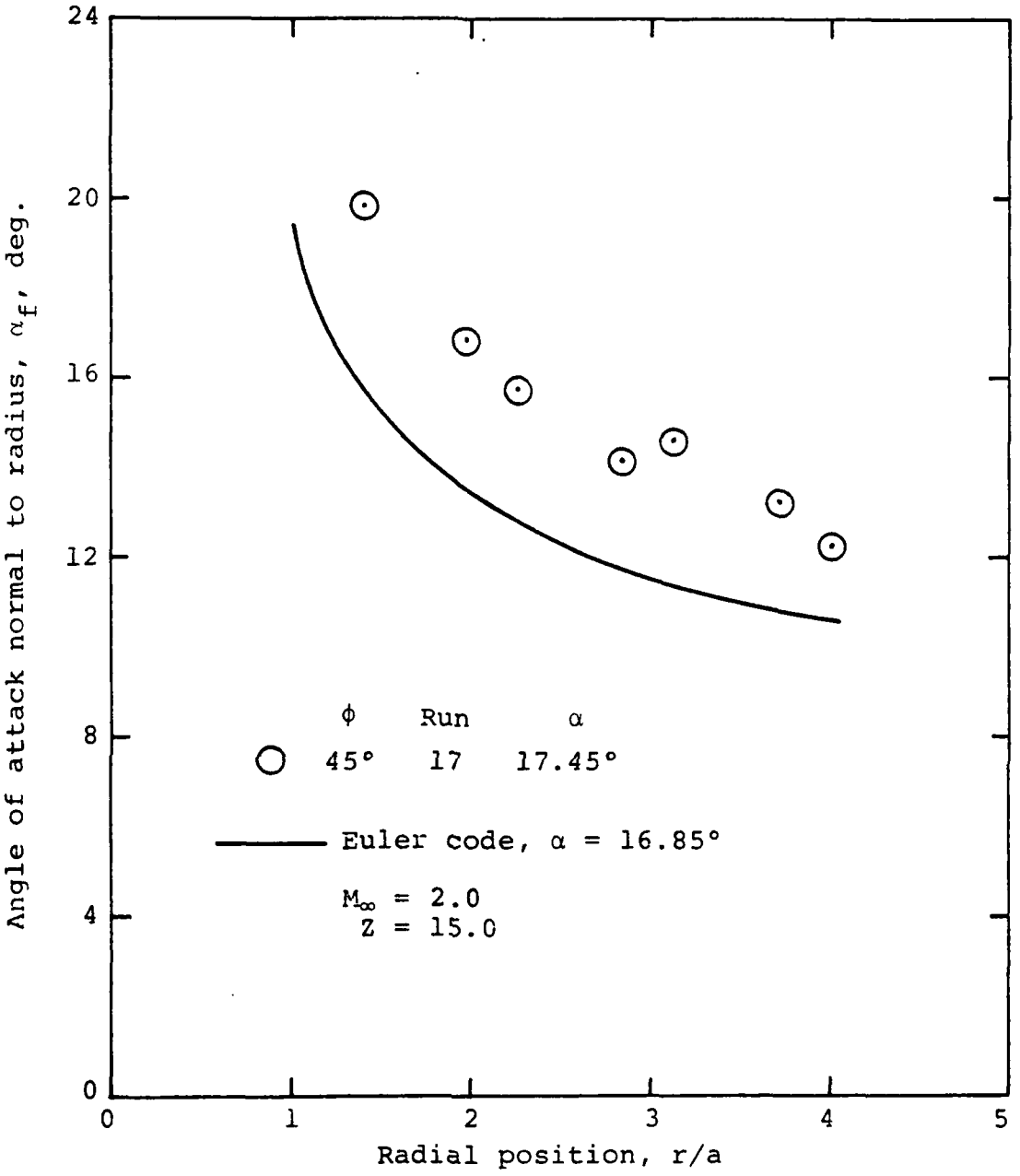

(b) $\phi = 45°$

Figure 22.- Continued.

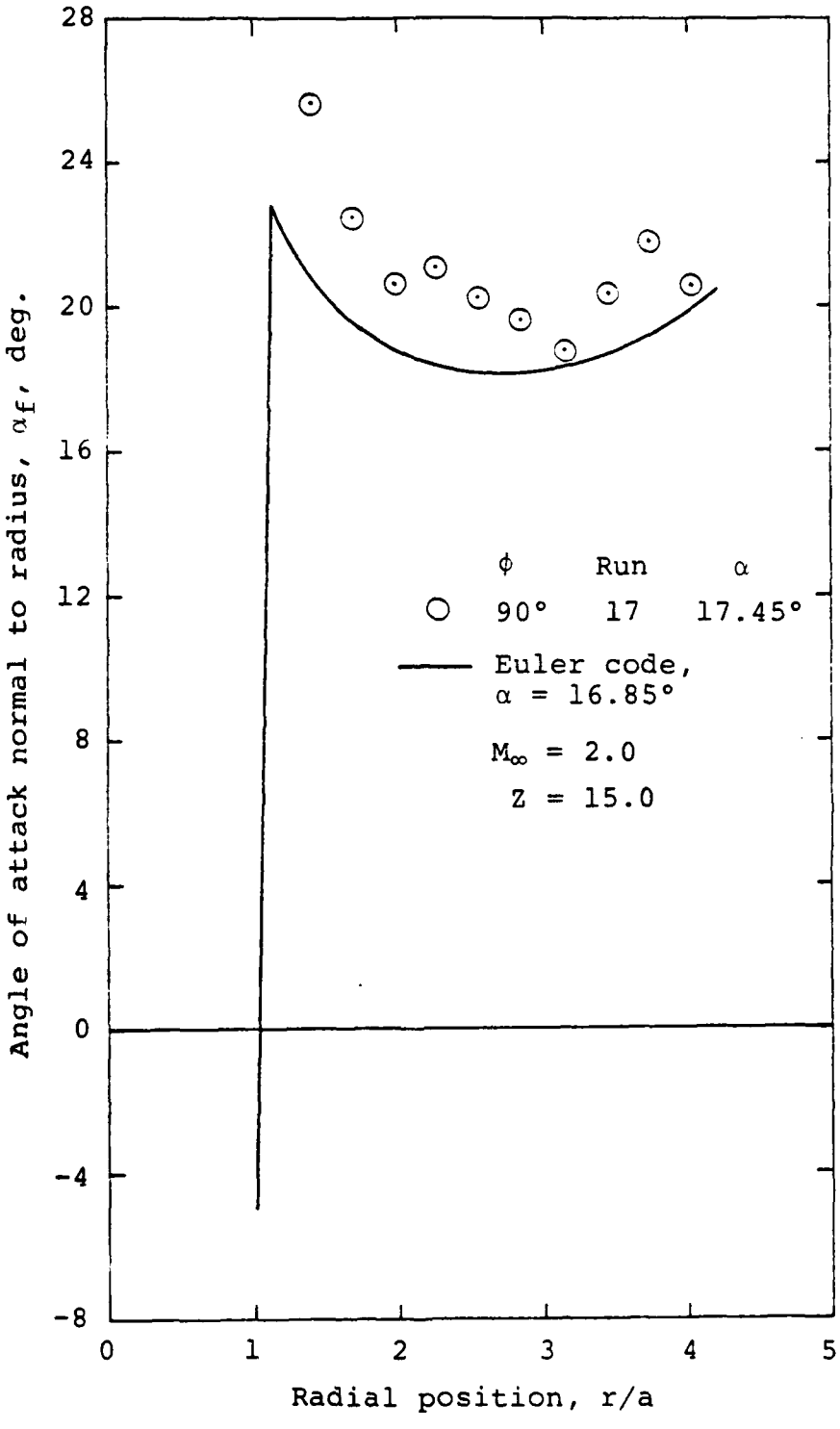

(c) $\phi = 90°$

Figure 22.- Continued.

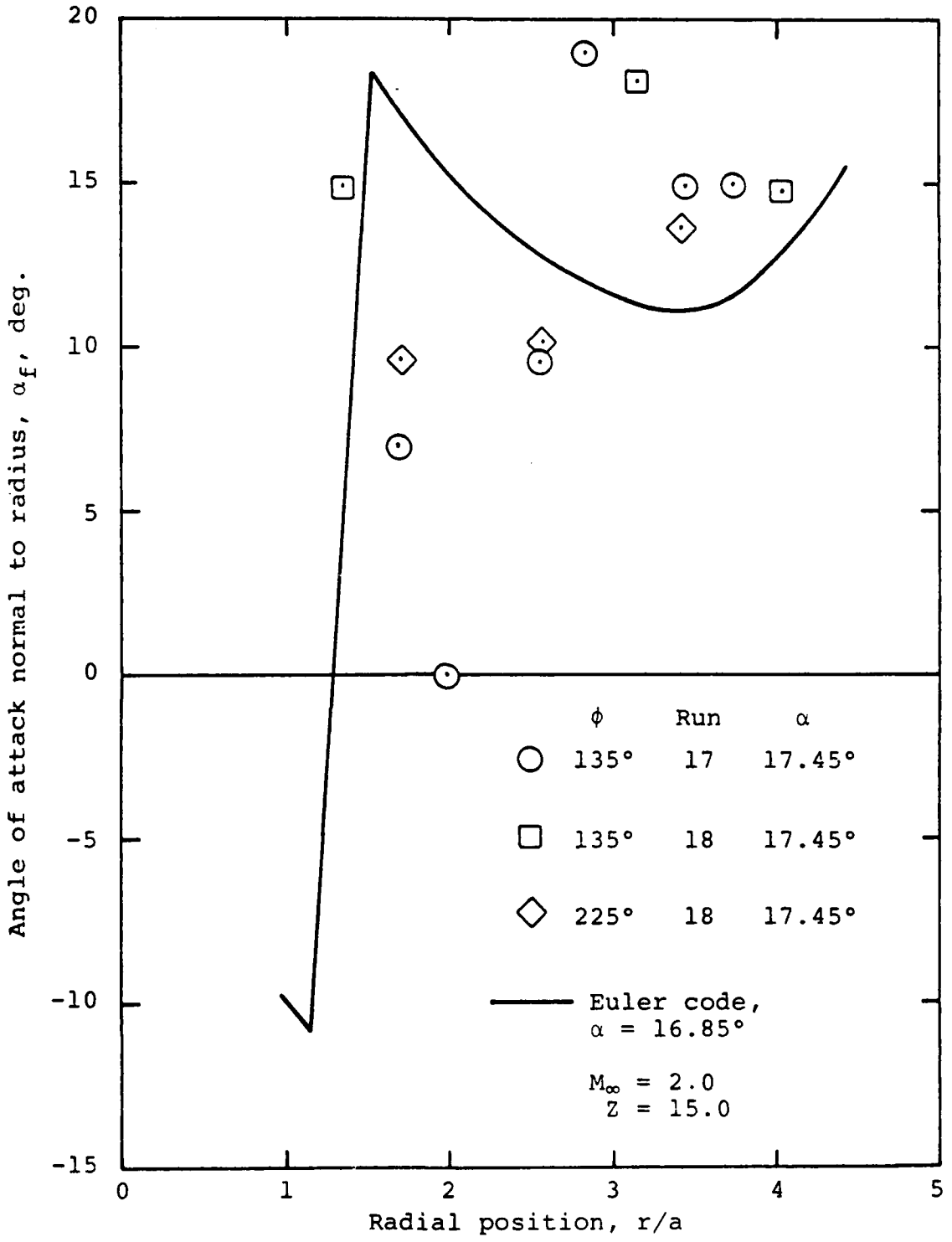

(d) ϕ = 135° and 225°

Figure 22.- Continued.

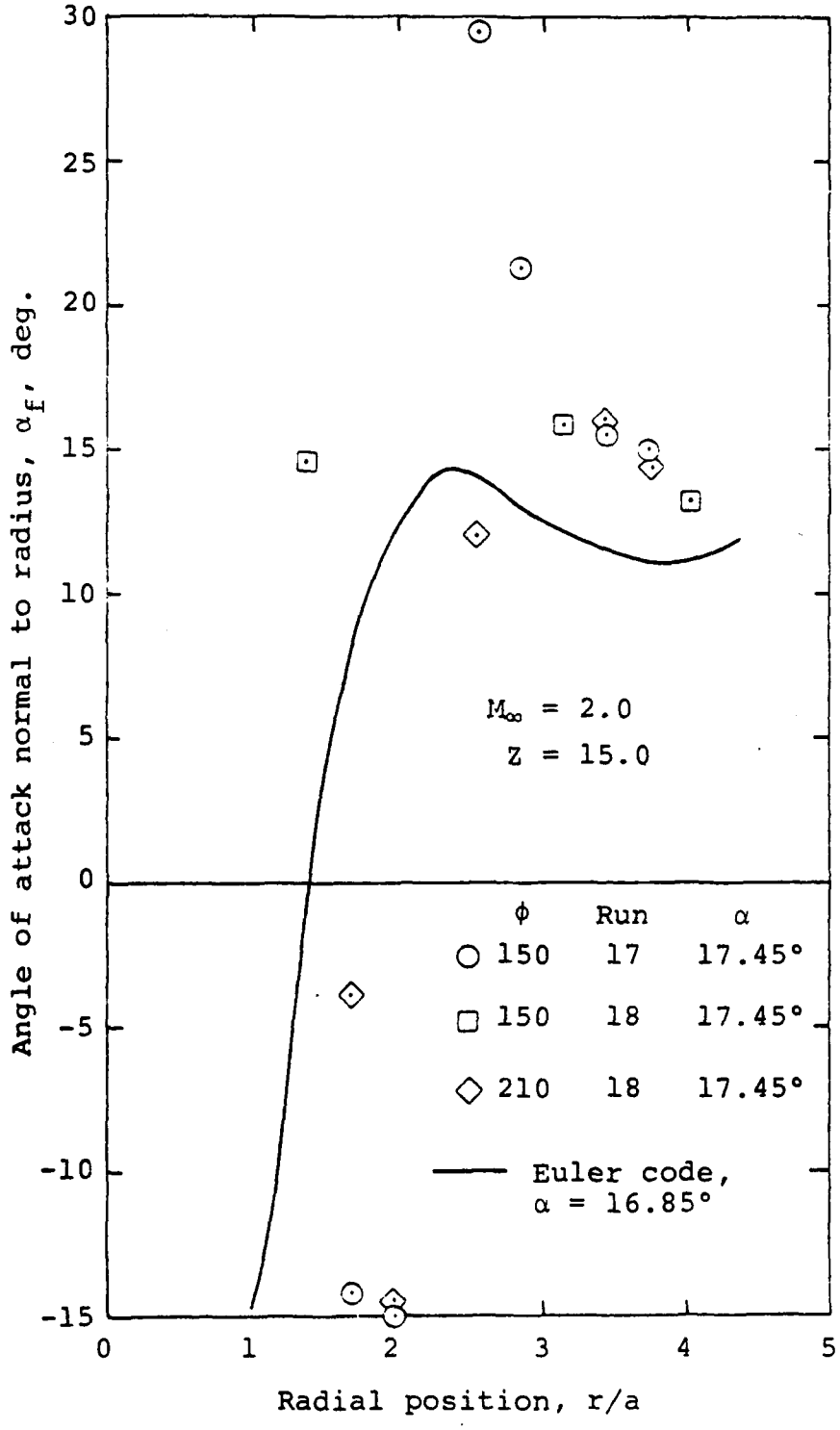

(e) $\phi = 150°$

Figure 22.- Continued.

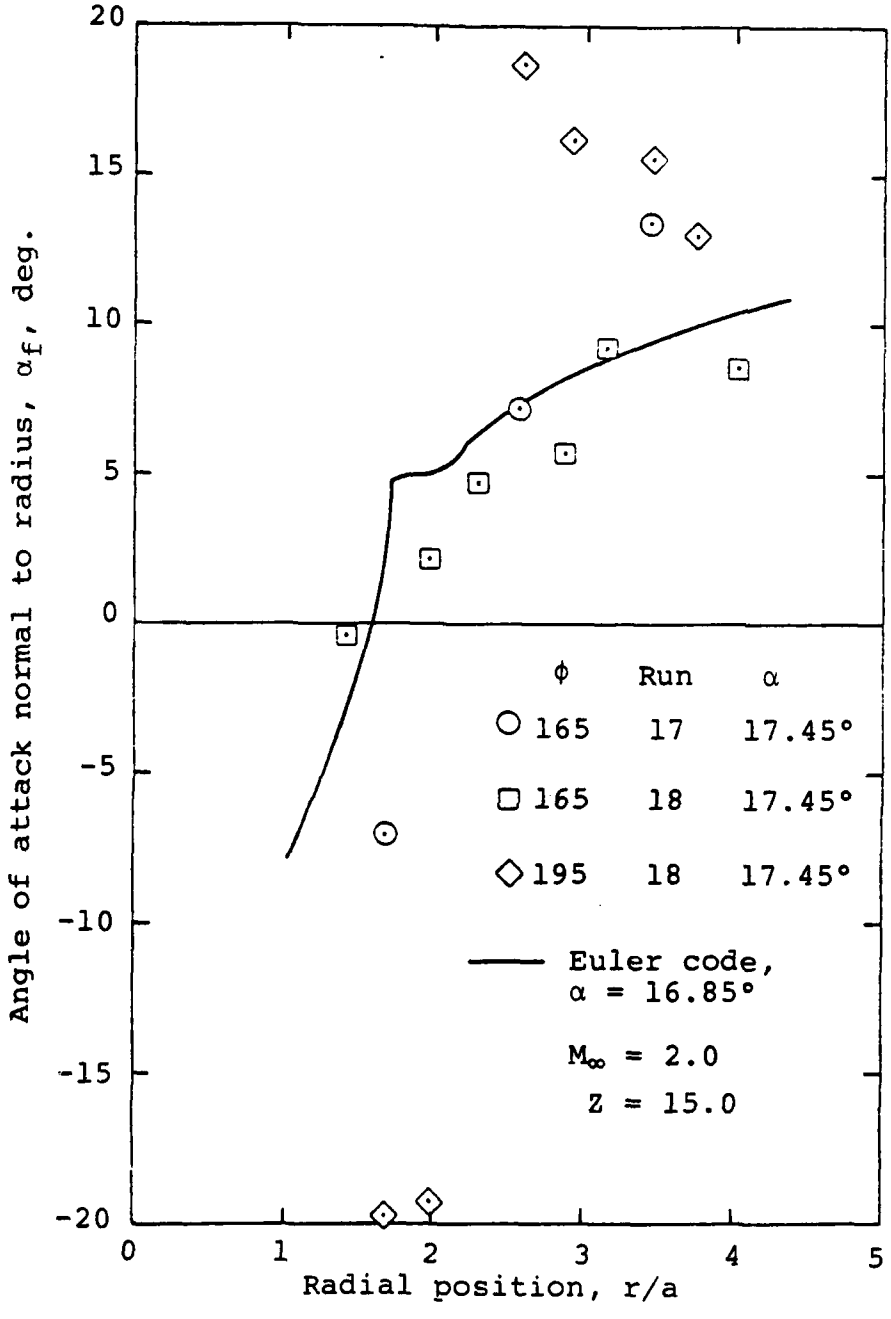

(f) ϕ = 165° and 195°

Figure 22.- Continued.

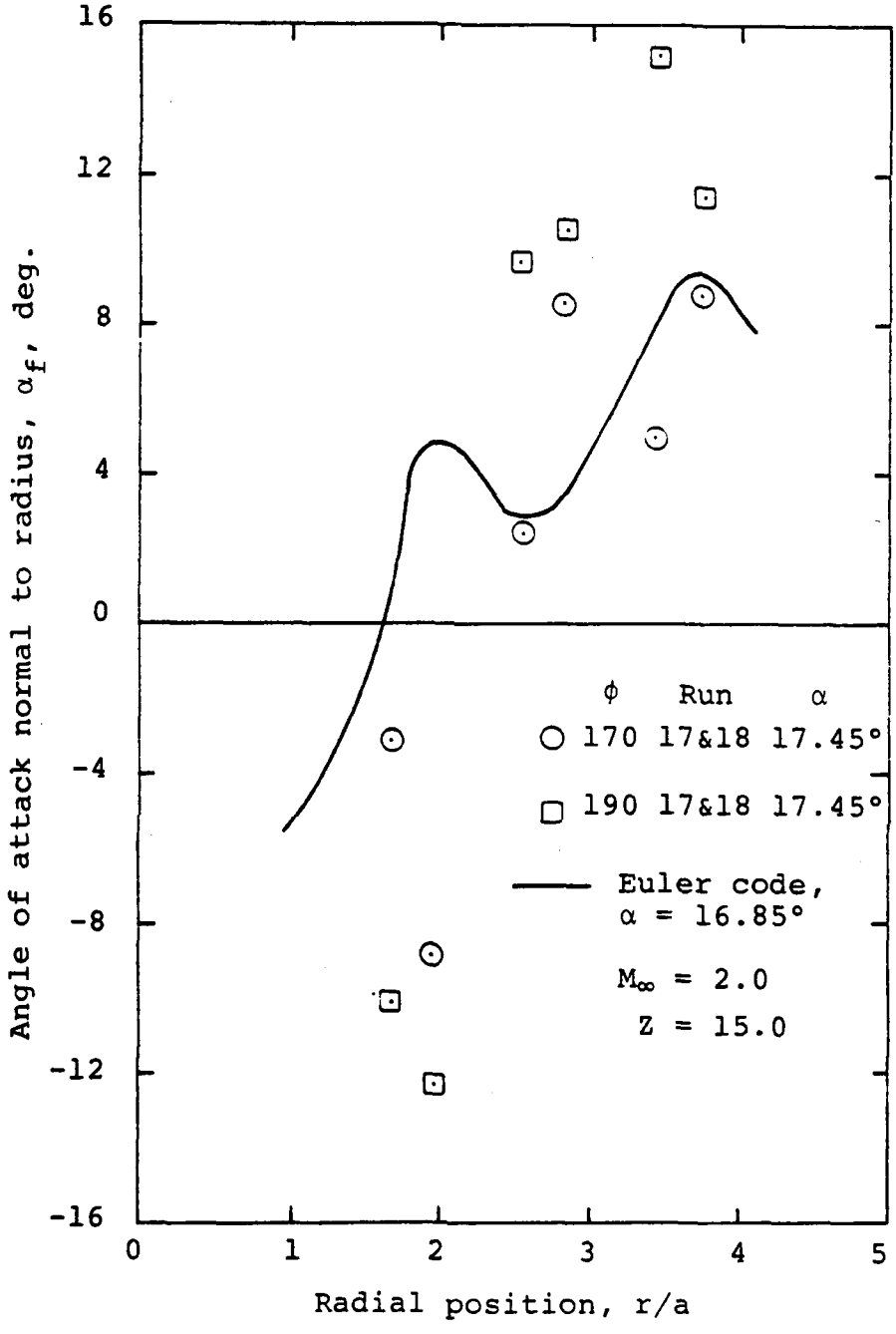

(g) ϕ = 170° and 190°

Figure 22.- Continued.

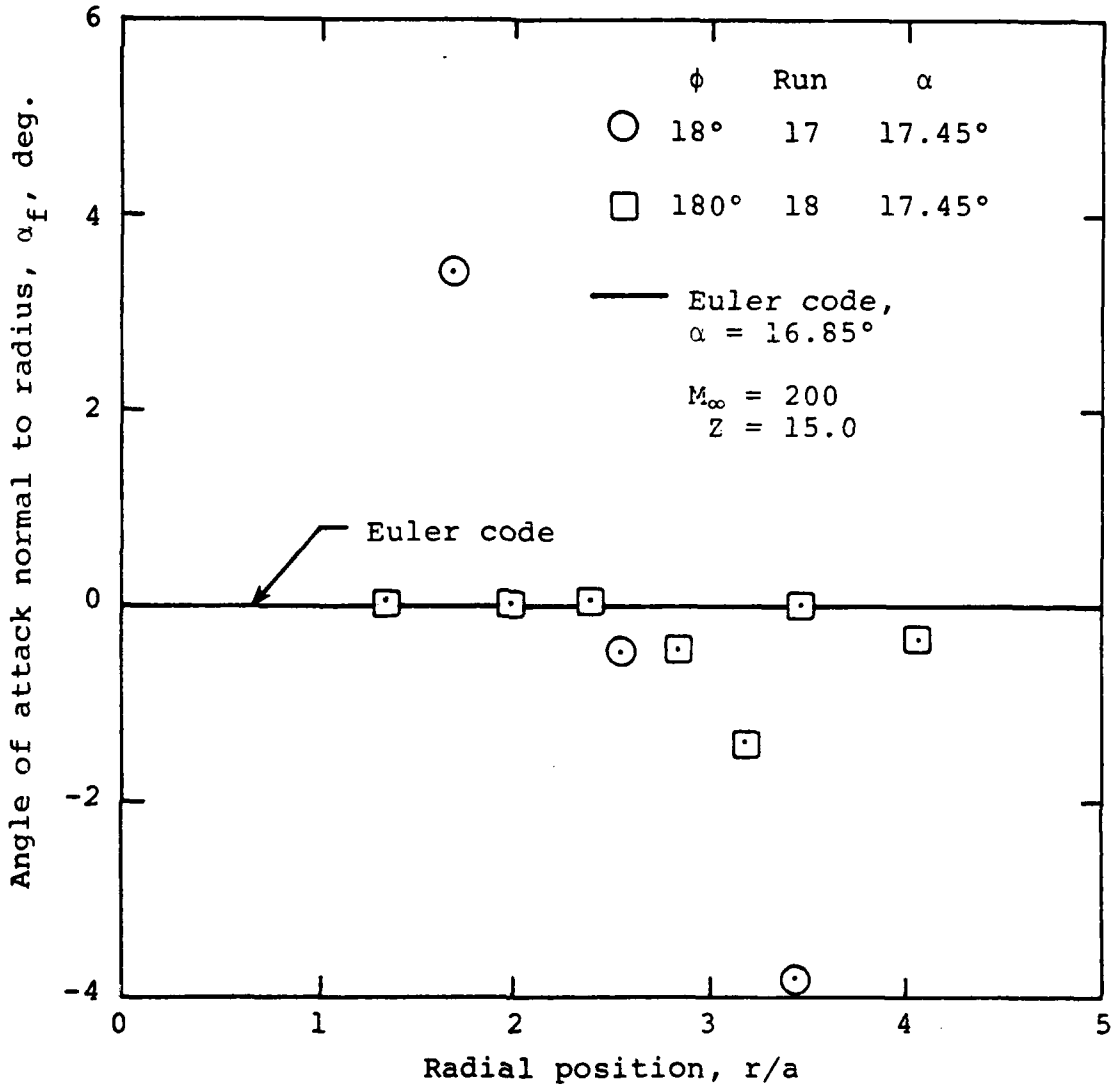

(h) $\phi = 180°$

Figure 22.- Concluded.

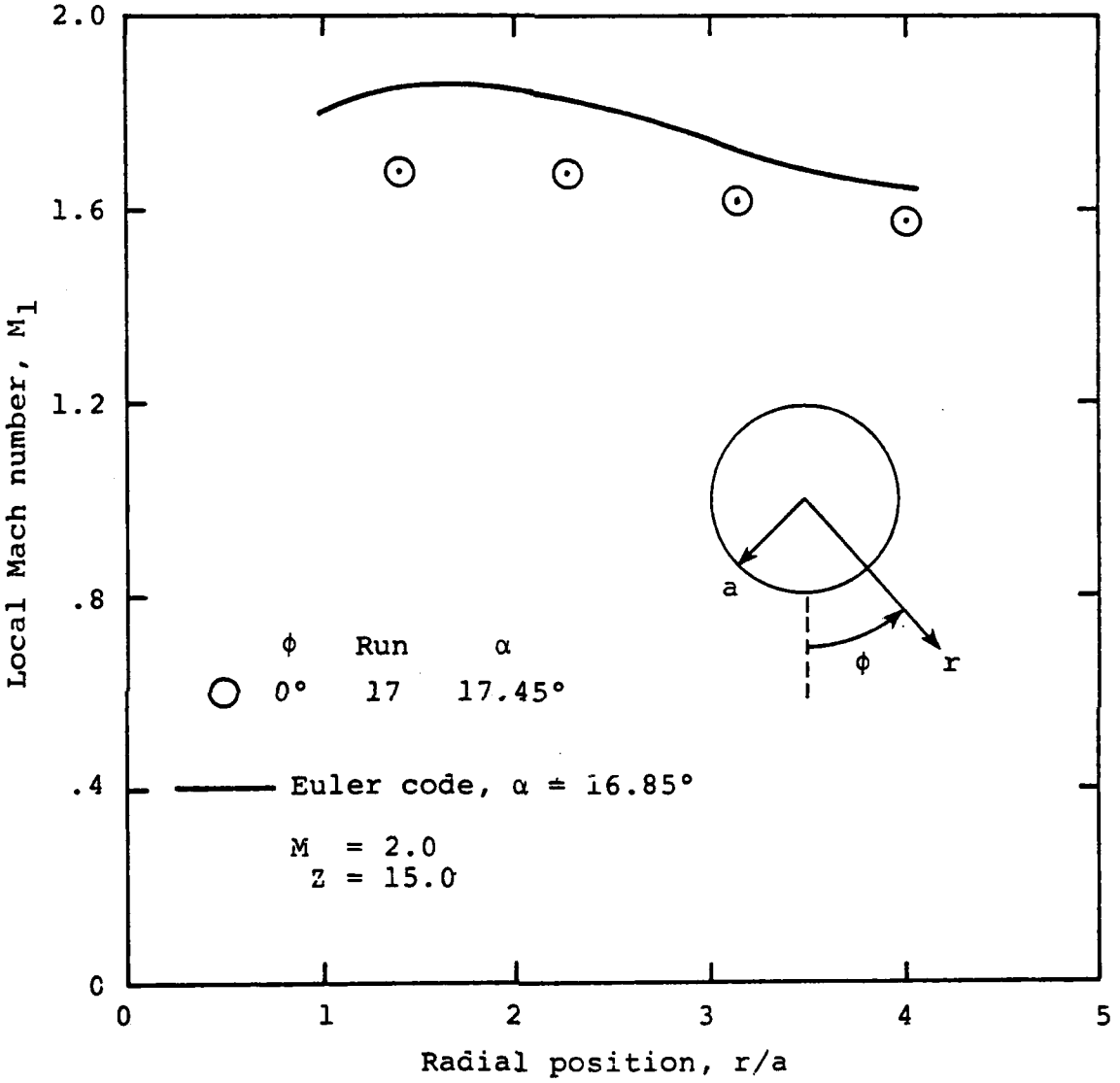

(a) $\phi = 0°$

Figure 23.- Comparison of local Mach number as measured and as calculated from Euler code for flow behind wing of wing-body combination.

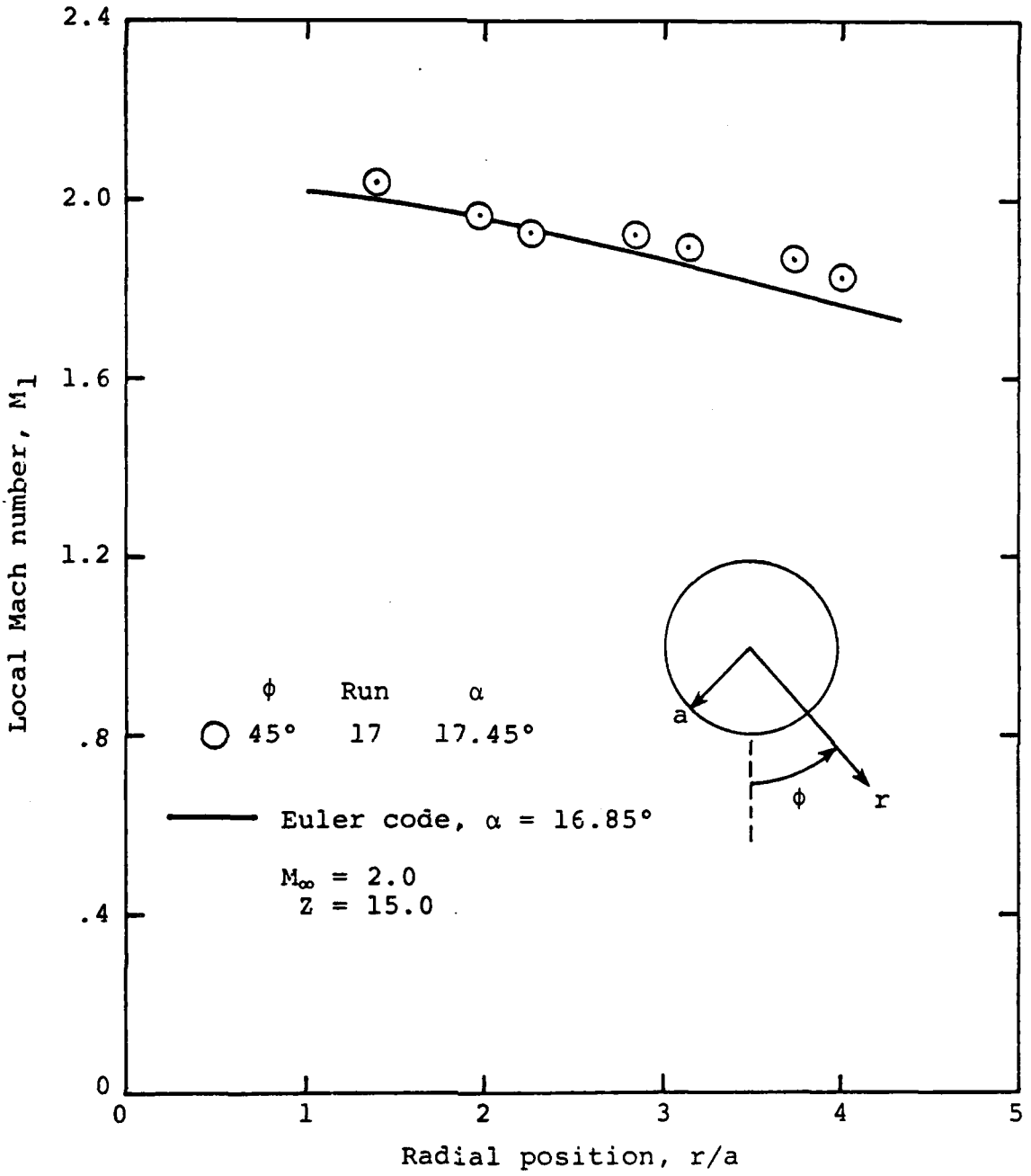

(b) $\phi = 45°$

Figure 23.- Continued.

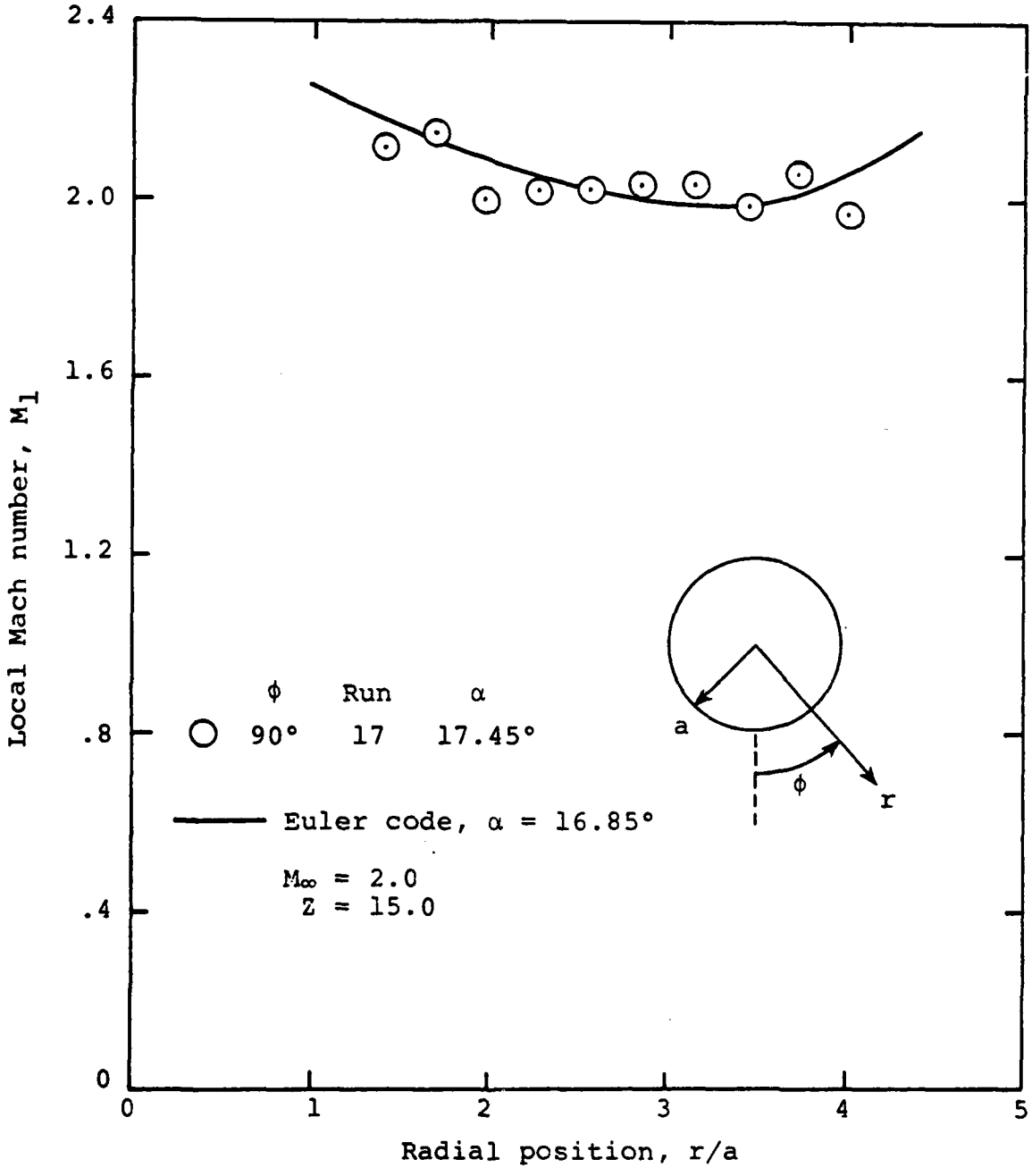

(c) $\phi = 90°$

Figure 23.- Continued.

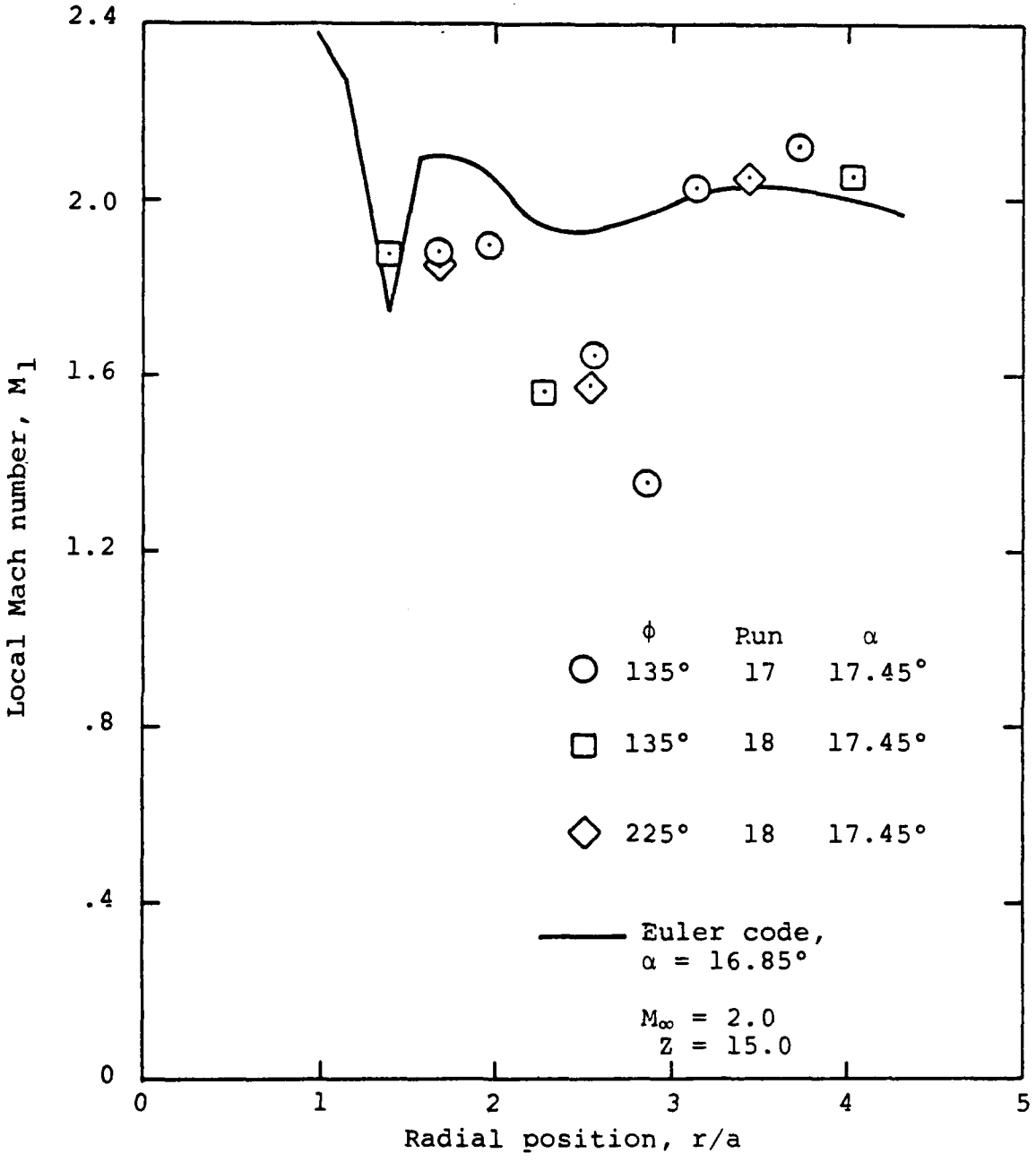

(d) $\phi = 135°$ and $225°$

Figure 23.- Continued.

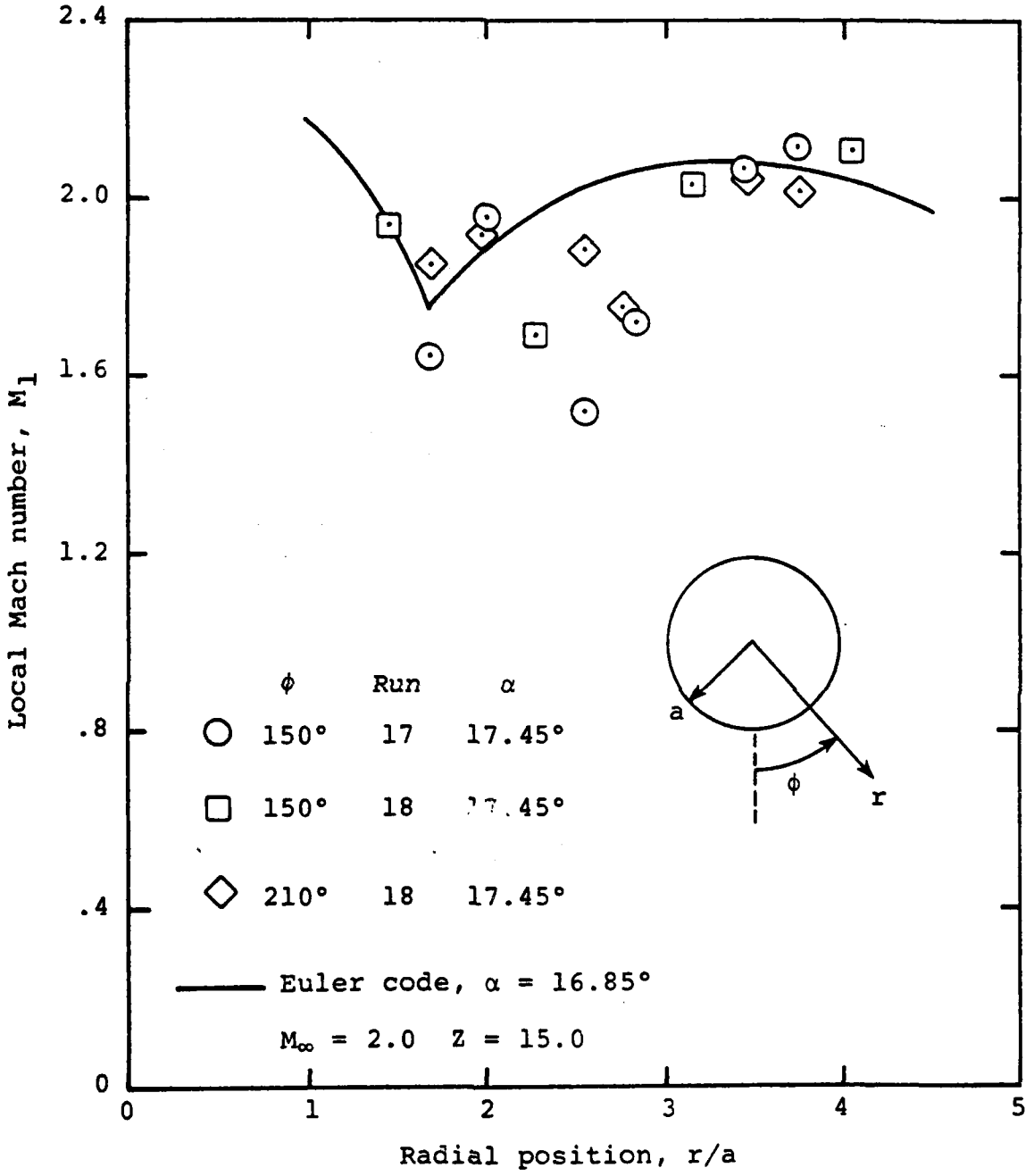

(e) ϕ = 150° and 210°

Figure 23.- Continued.

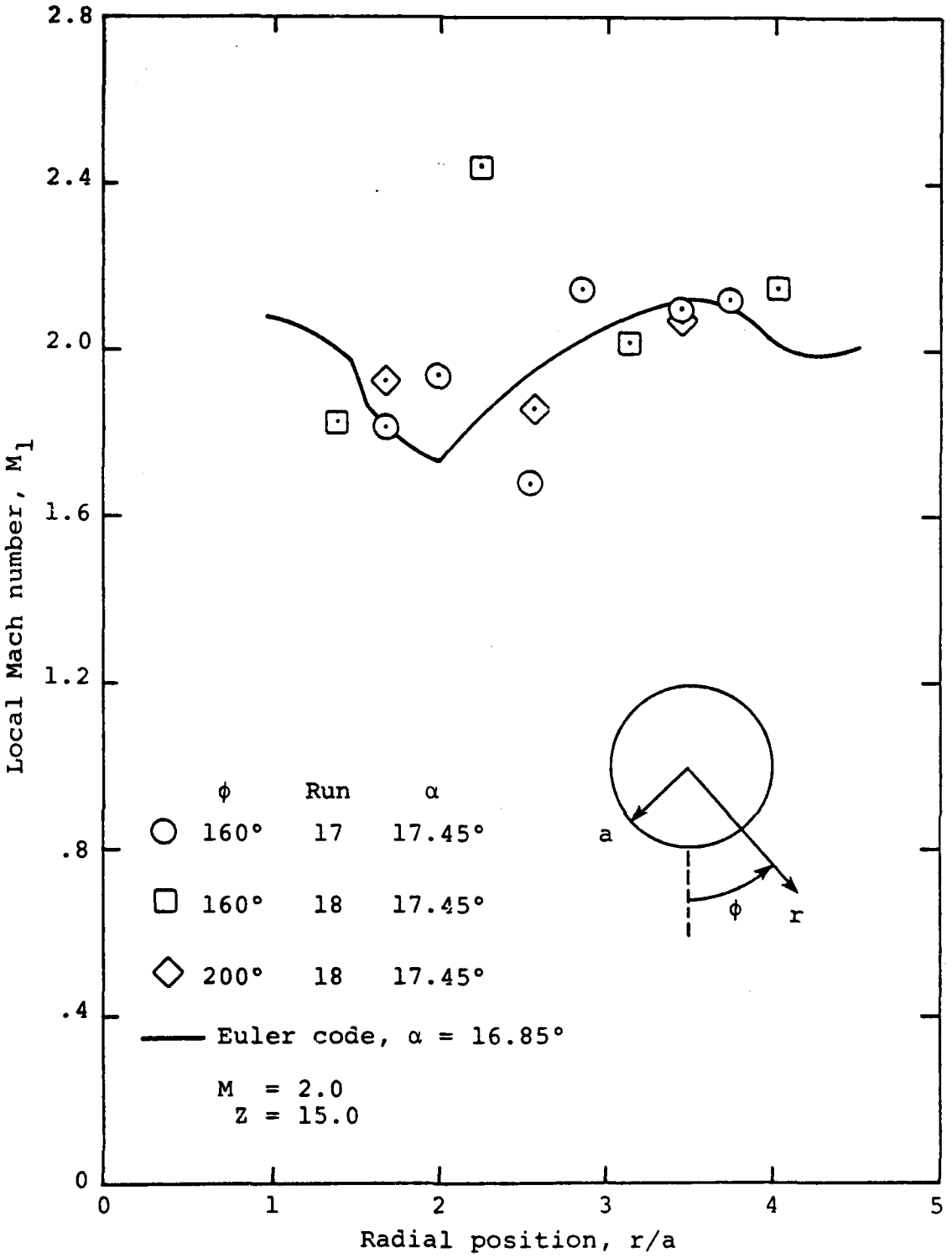

(f) ϕ = 160° and 200°

Figure 23.- Continued.

AD-A135 118 STUDIES AND VORTICITY EFFECTS BY THE EULER EQUATIONS WITH EMPHASIS ON SUP.. (U) NIELSEN ENGINEERING AND RESEARCH INC MOUNTAIN VIEW CA J N NIELSEN ET AL. 2/2

UNCLASSIFIED OCT 83 NEAR-TR-310 N00014-82-C-0391 F/G 20/4 NL

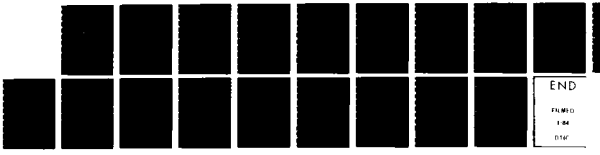

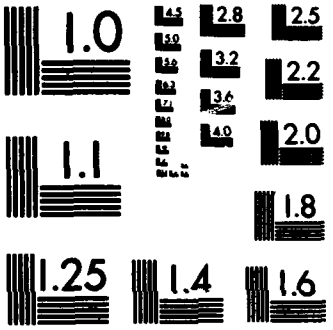

MICROCOPY RESOLUTION TEST CHART
NATIONAL BUREAU OF STANDARDS-1963-A

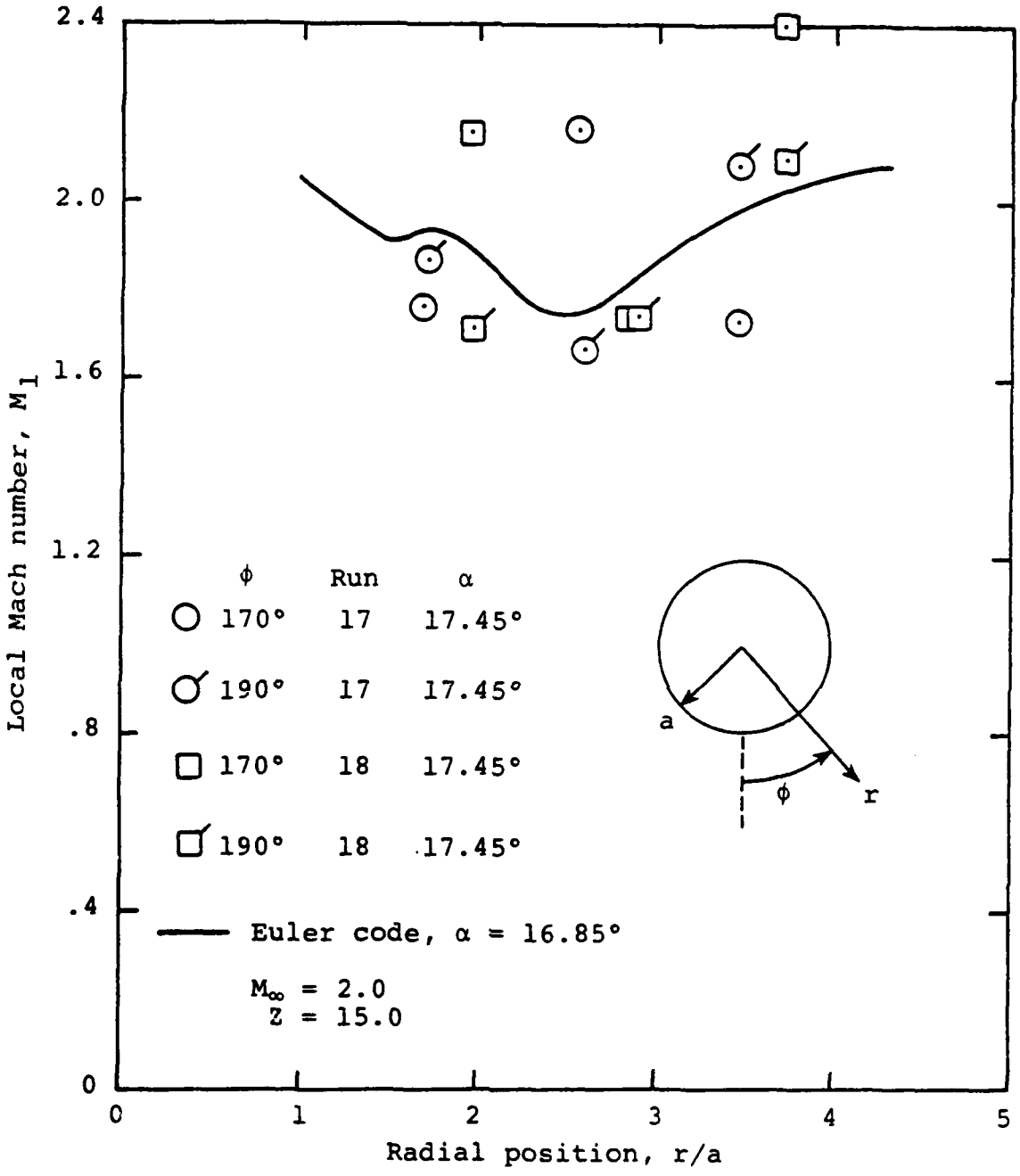

(g) ϕ = 170° and 190°

Figure 23.- Continued.

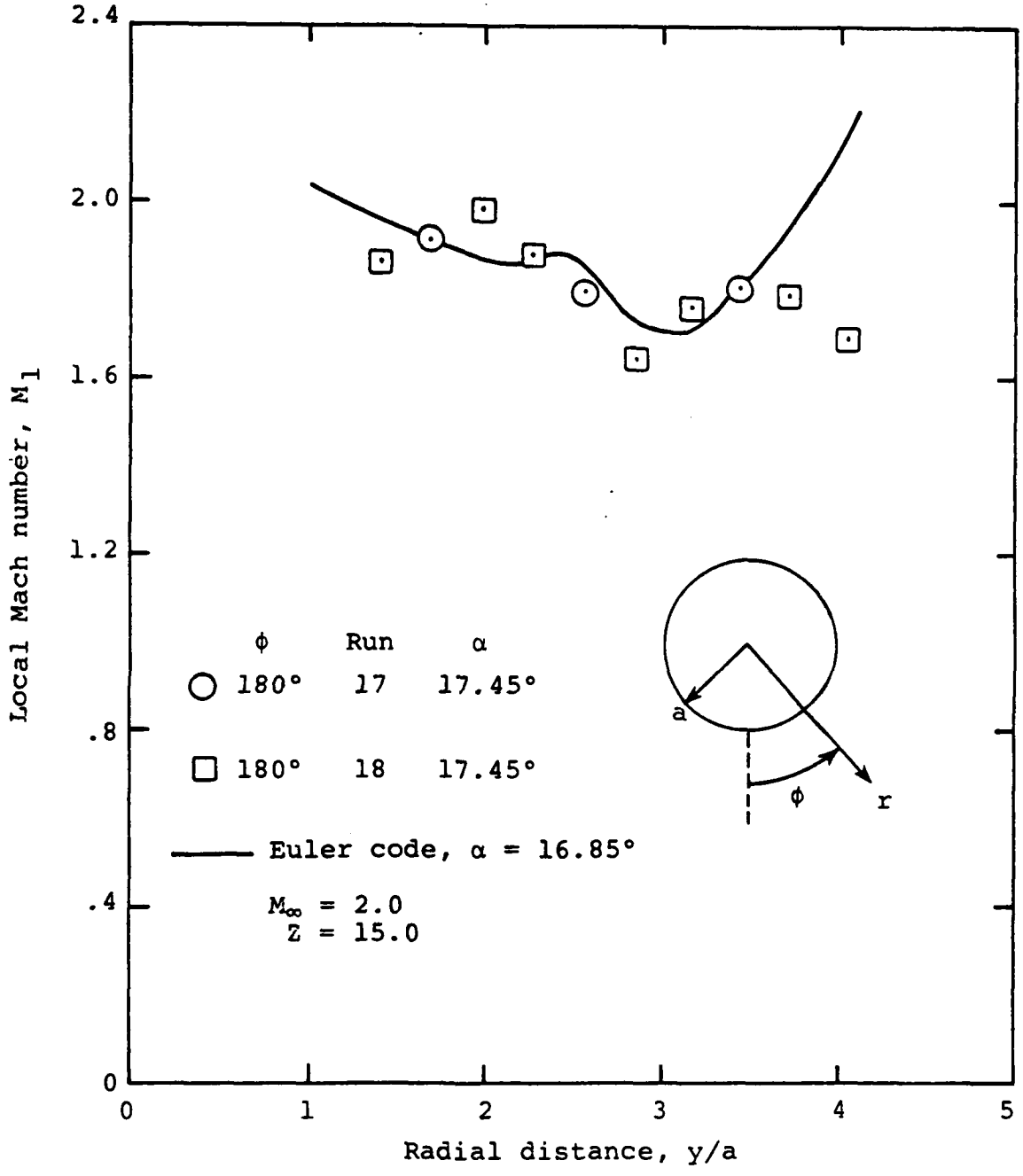

(h) $\phi = 180°$

Figure 23.- Concluded.

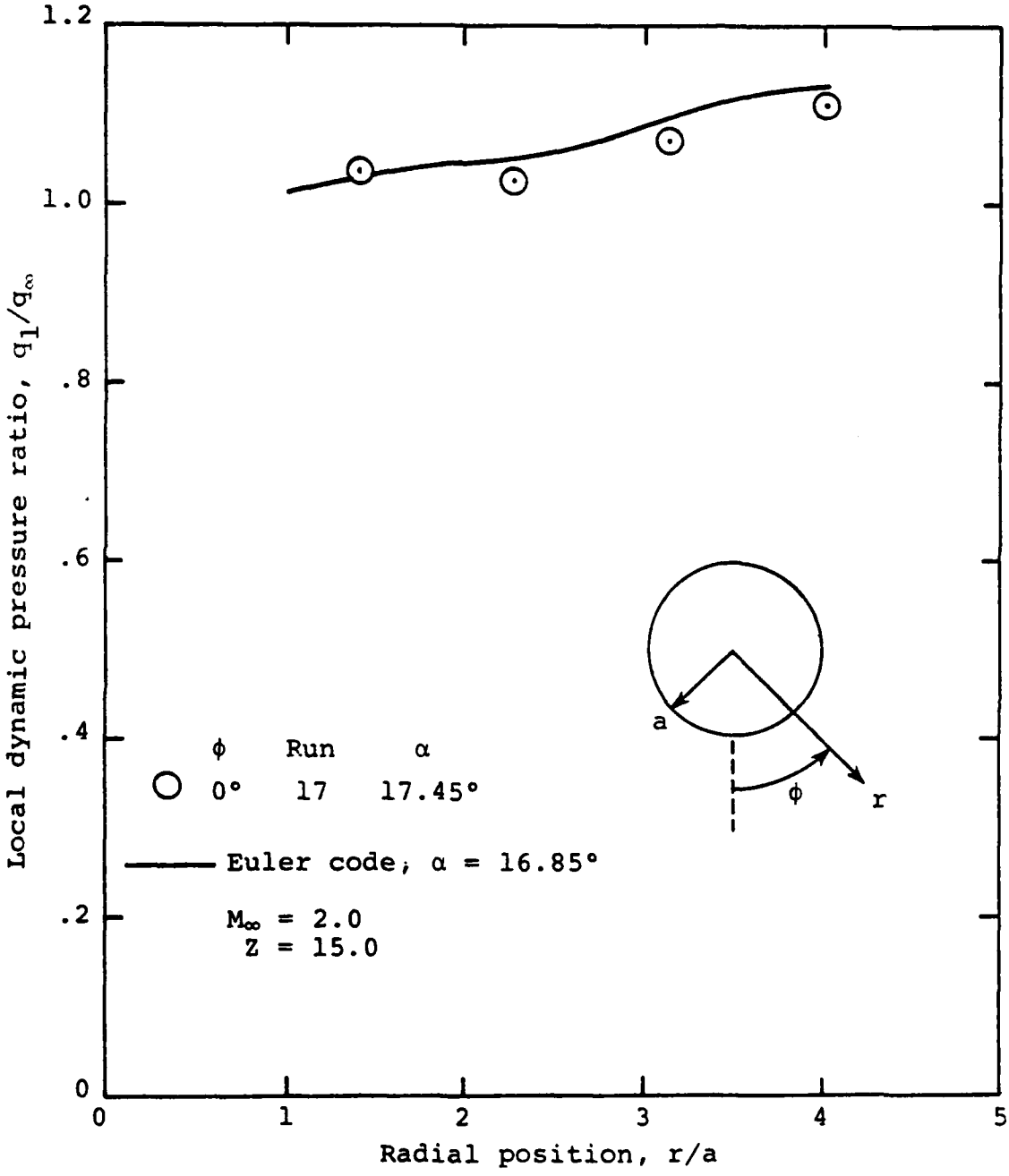

(a) $\phi = 0°$

Figure 24.- Comparison of local dynamic pressure ratio as measured and as calculated from Euler code for flow behind wing of wing-body combination.

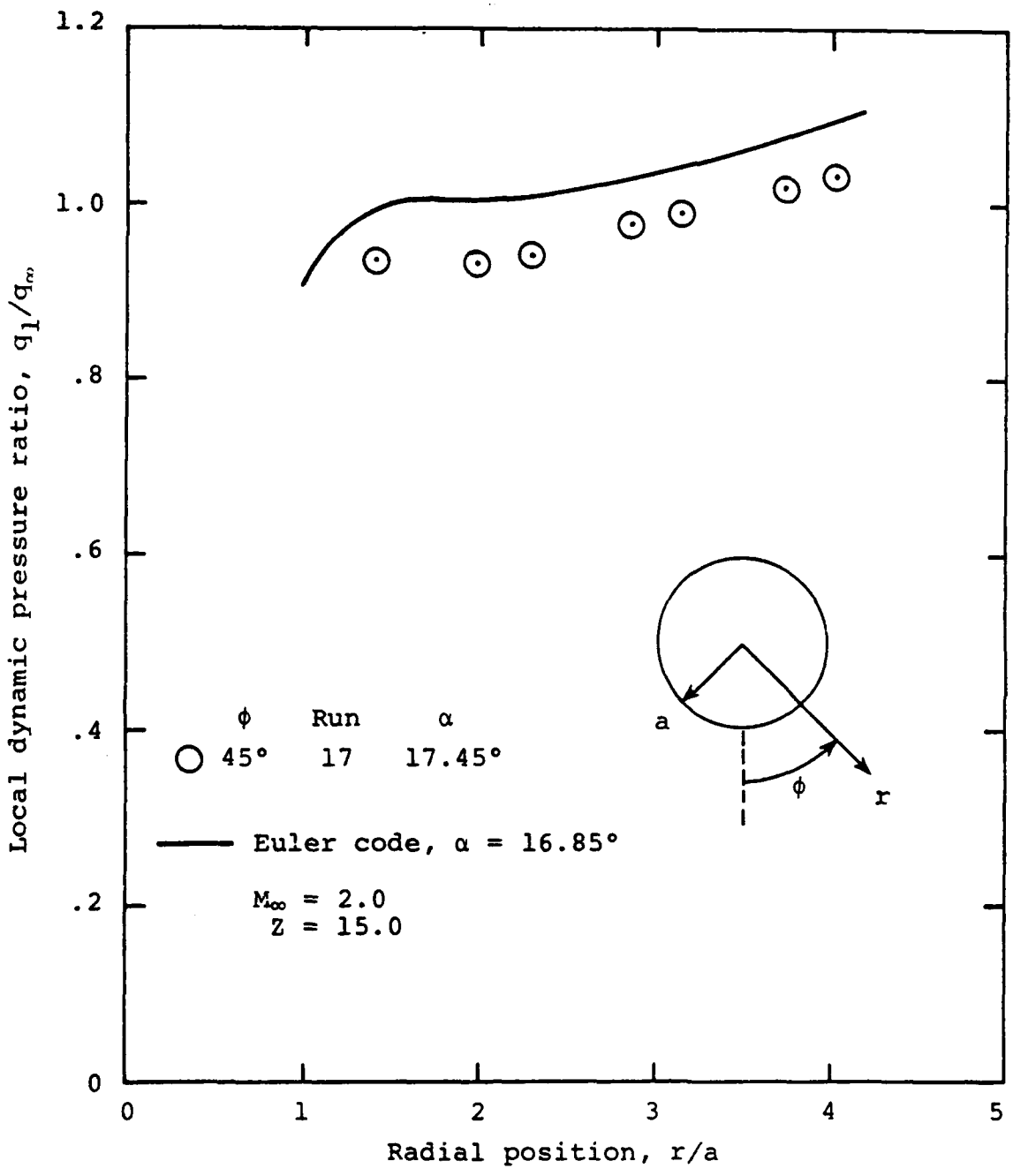

(b) $\phi = 45°$

Figure 24.- Continued.

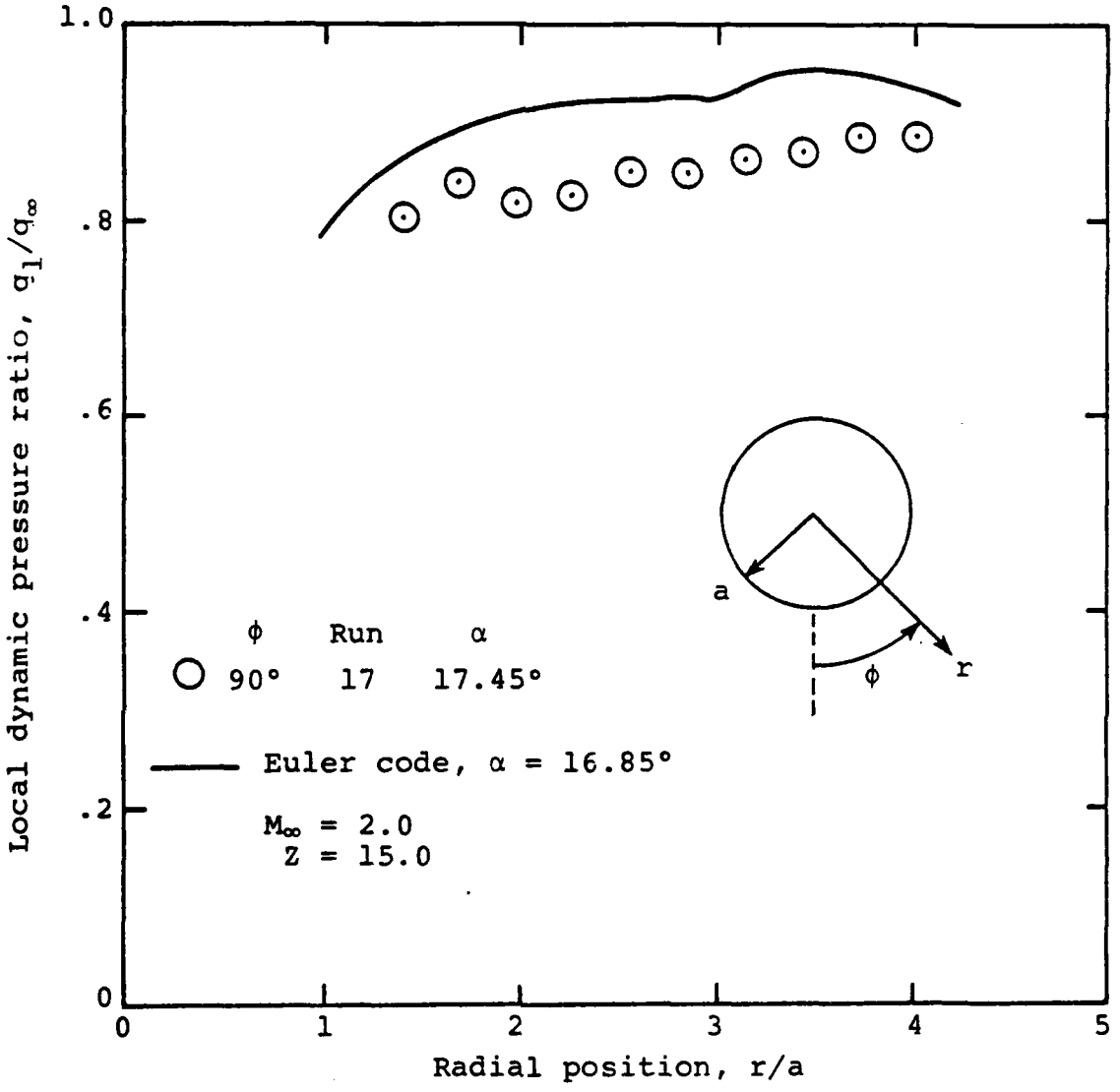

(c) $\phi = 90°$

Figure 24.- Continued.

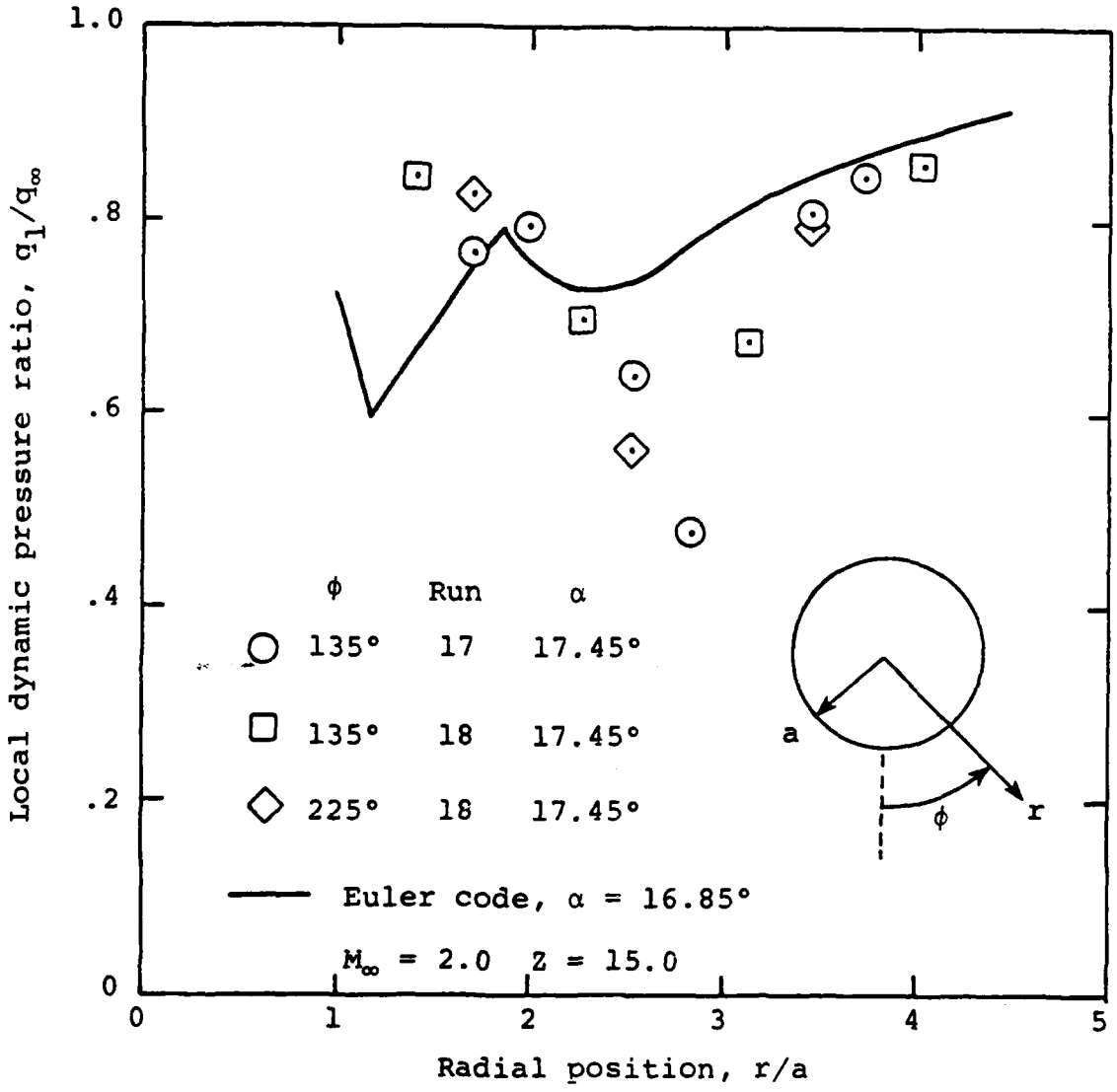

(d) ϕ = 135° and 225°

Figure 24.- Continued.

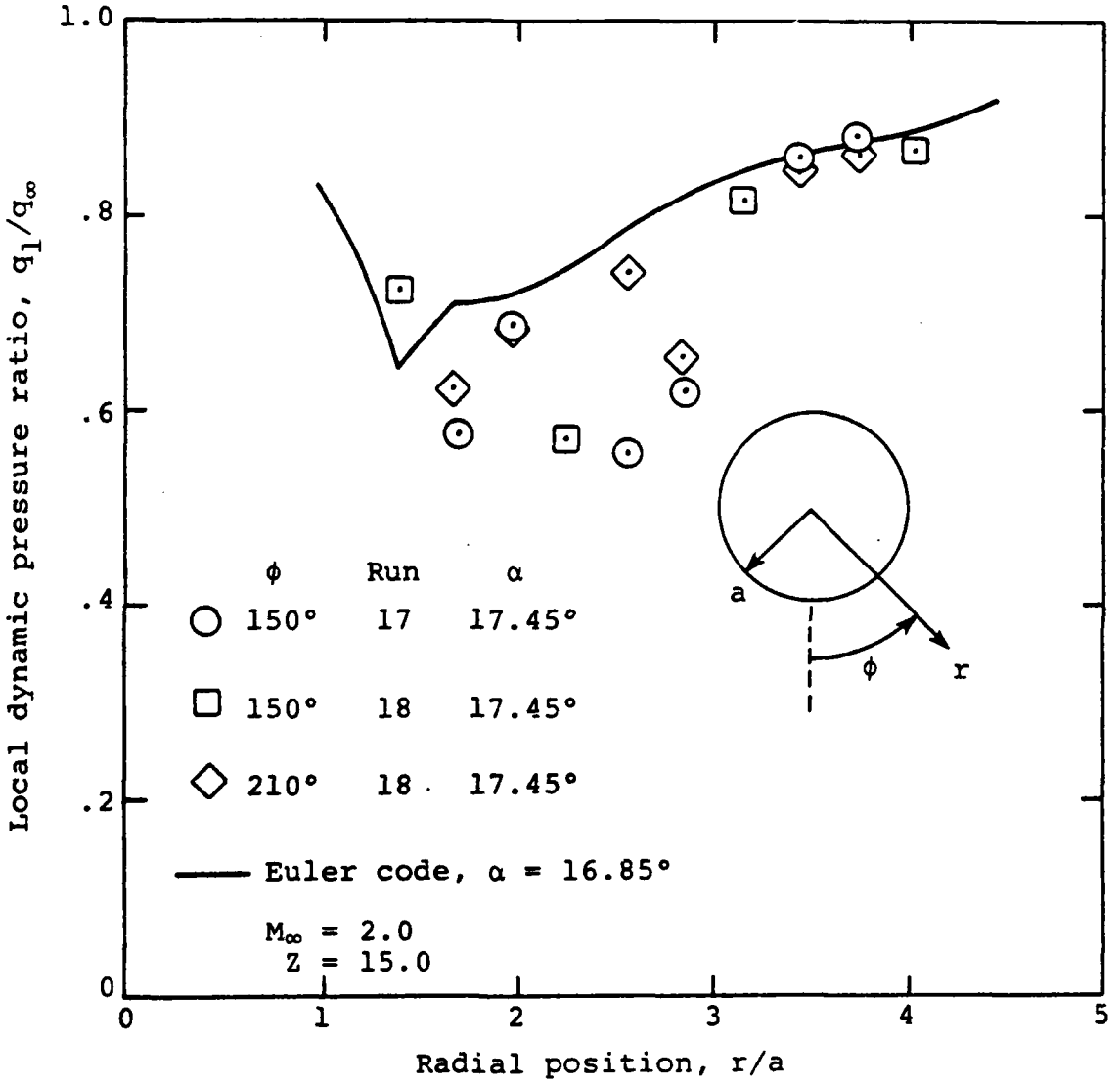

(e) ϕ = 150° and 210°

Figure 24.- Continued.

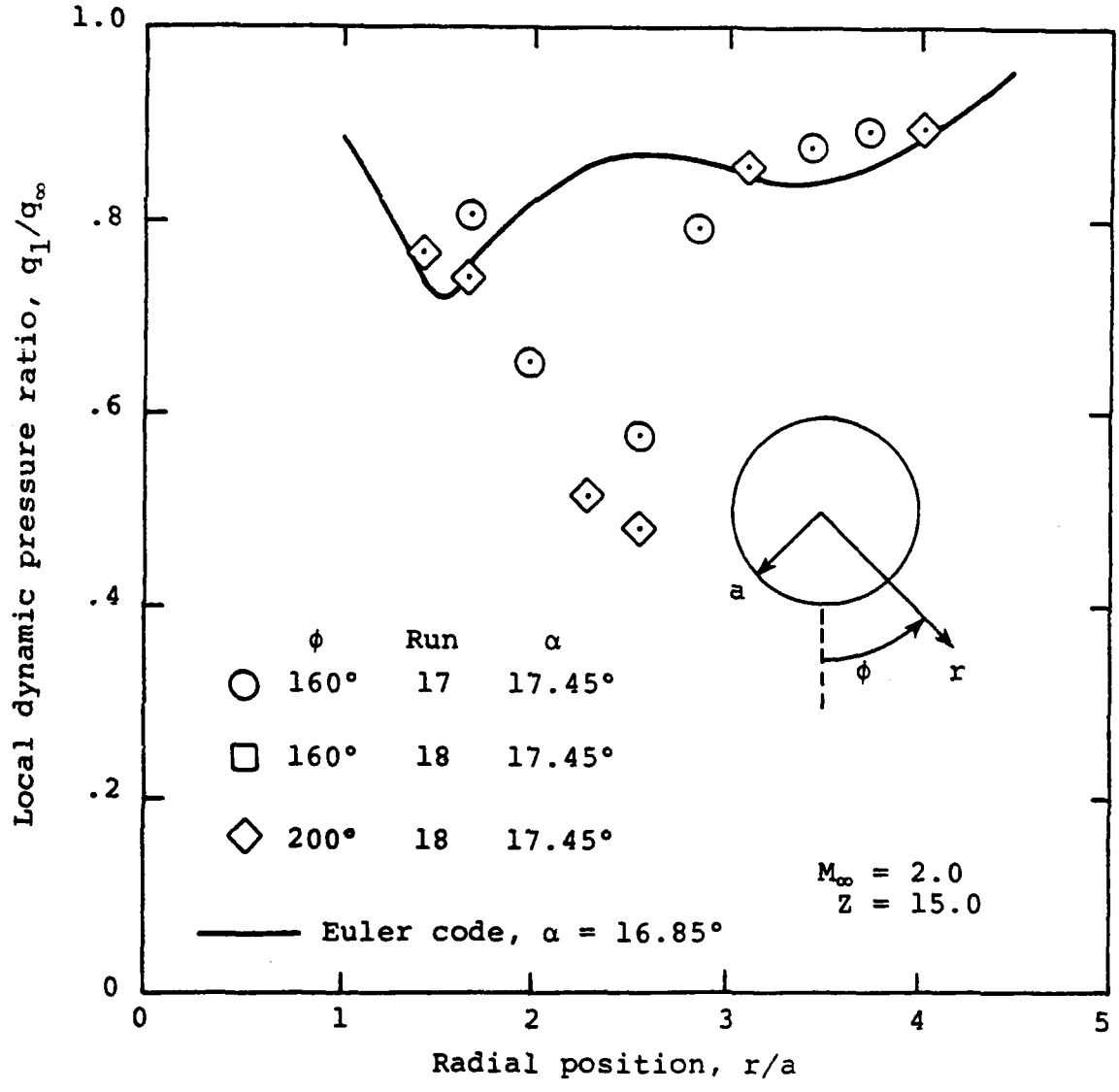

(f) ϕ = 160° and 200°

Figure 24.- Continued.

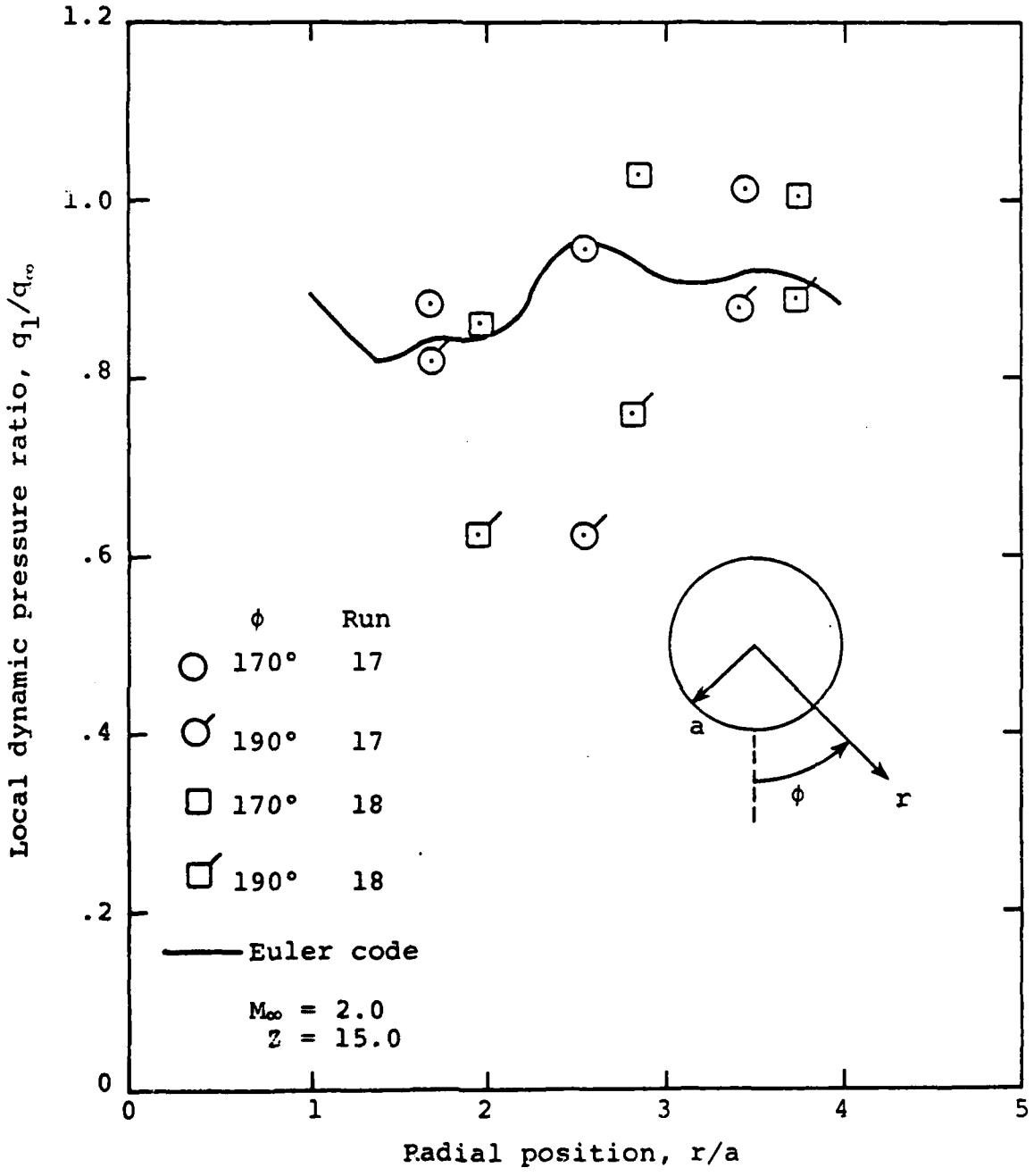

(g) ϕ = 170° and 190°

Figure 24.- Continued.

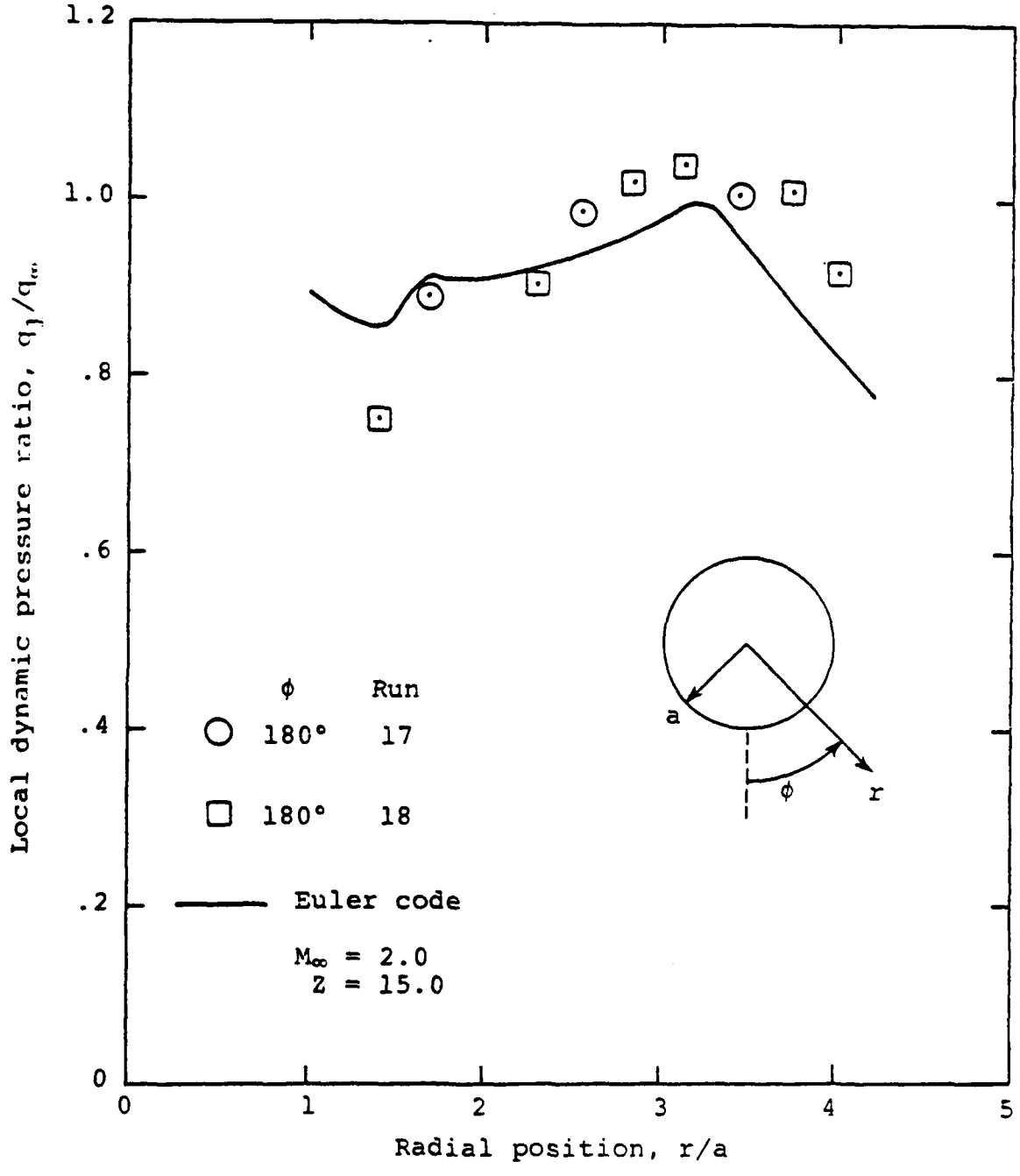

(h) $\phi = 180°$

Figure 24.- Concluded.

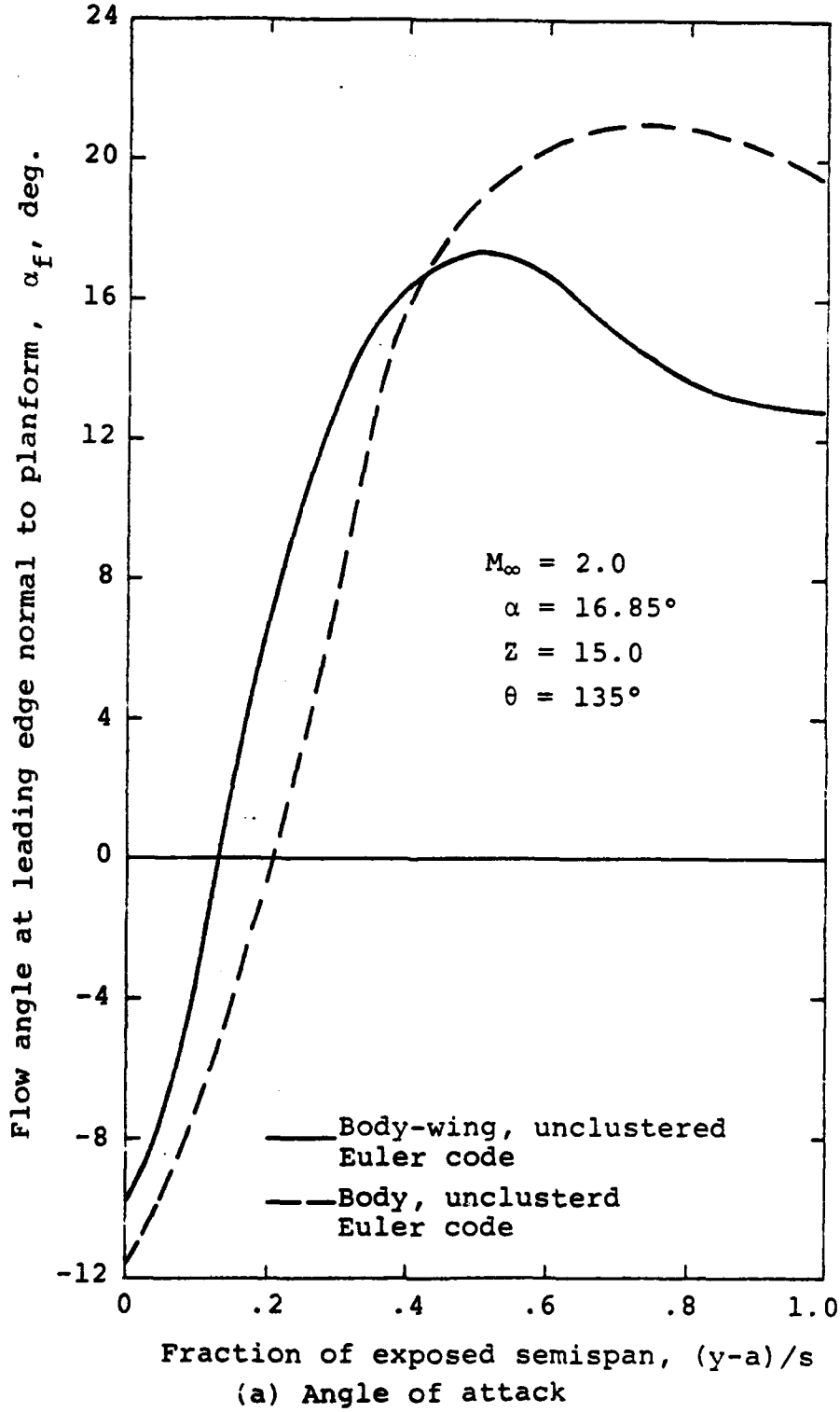

(a) Angle of attack

Figure 25.- Variation of flow parameters along fin leading-edge location for body-alone and body-wing flow fields as calculated by an Euler code.

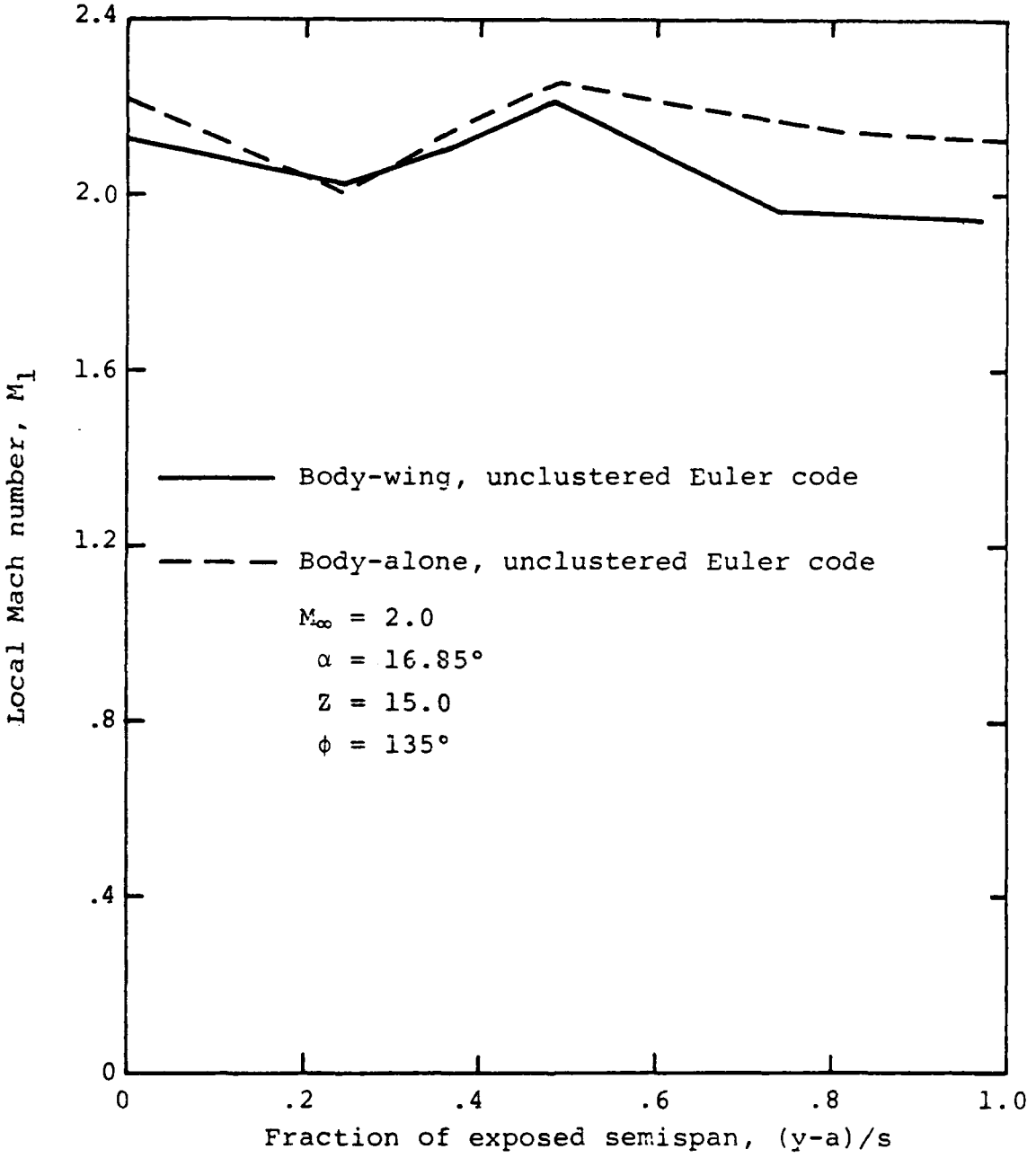

(b) Local Mach number

Figure 25.- Continued.

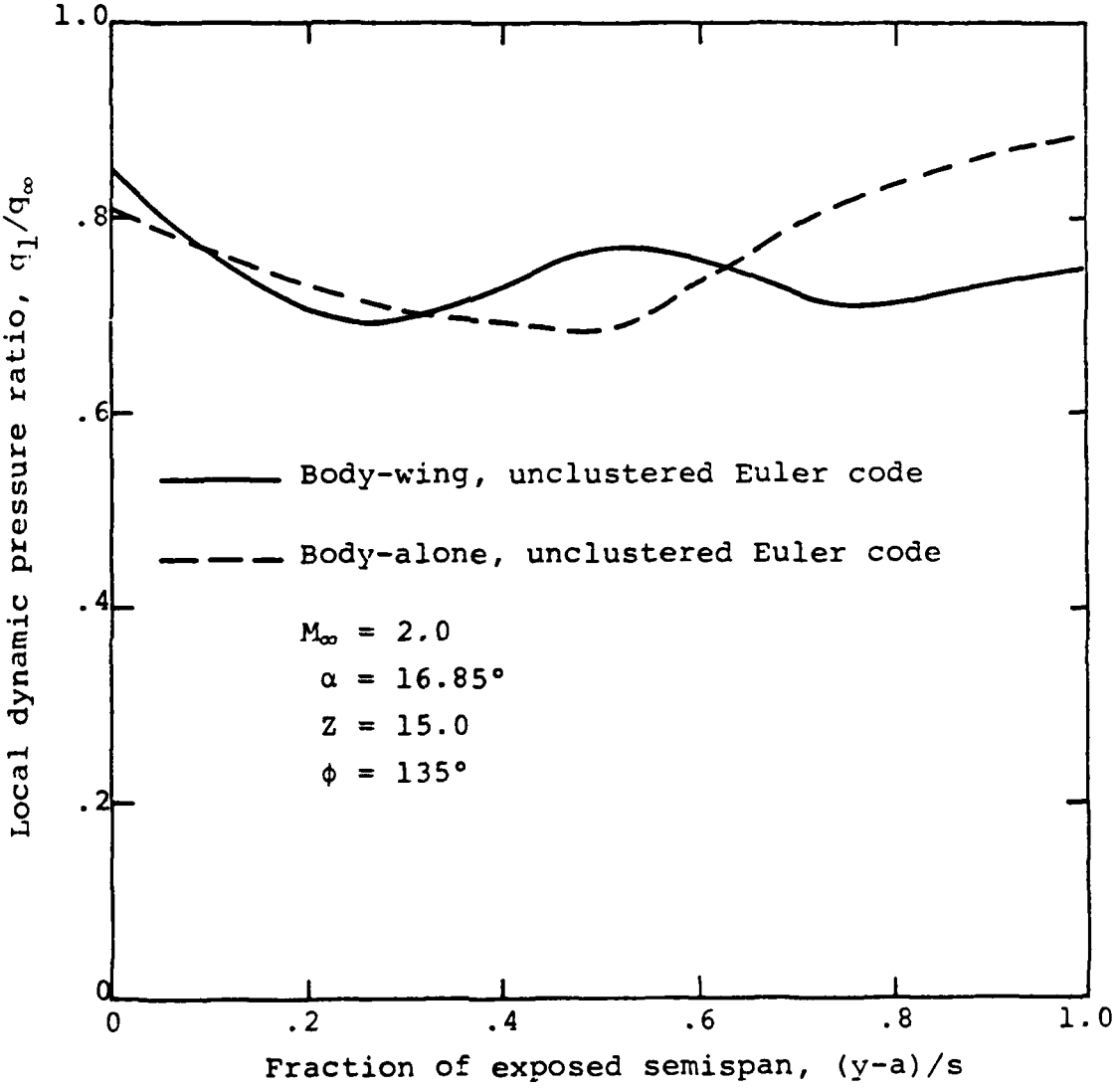

(c) Local dynamic pressure

Figure 25.- Concluded.

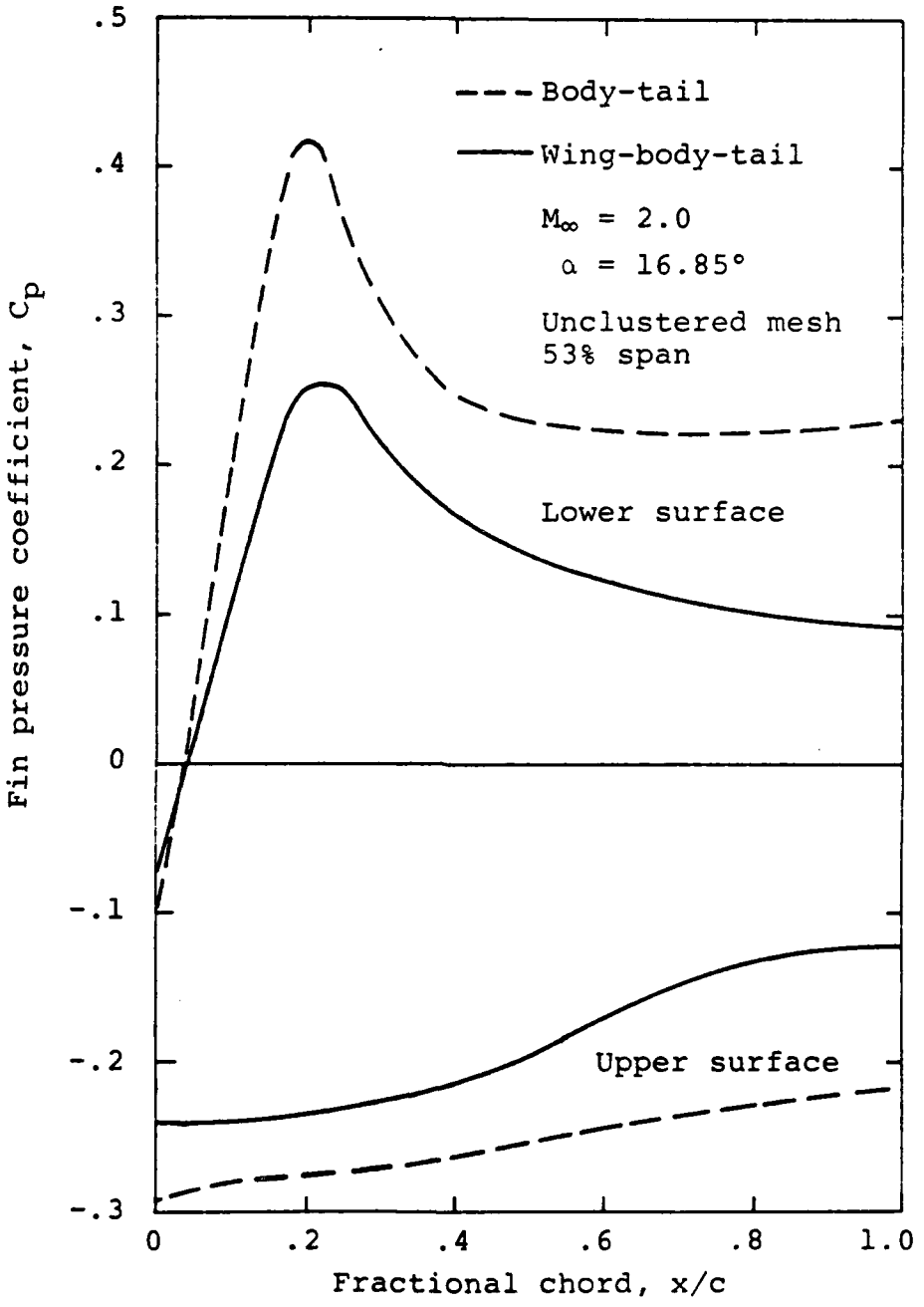

Figure 26.- Chordwise pressure distributions on upper and lower surfaces of interdigitated tail of body-tail and body-wing-tail as calculated by an Euler code.

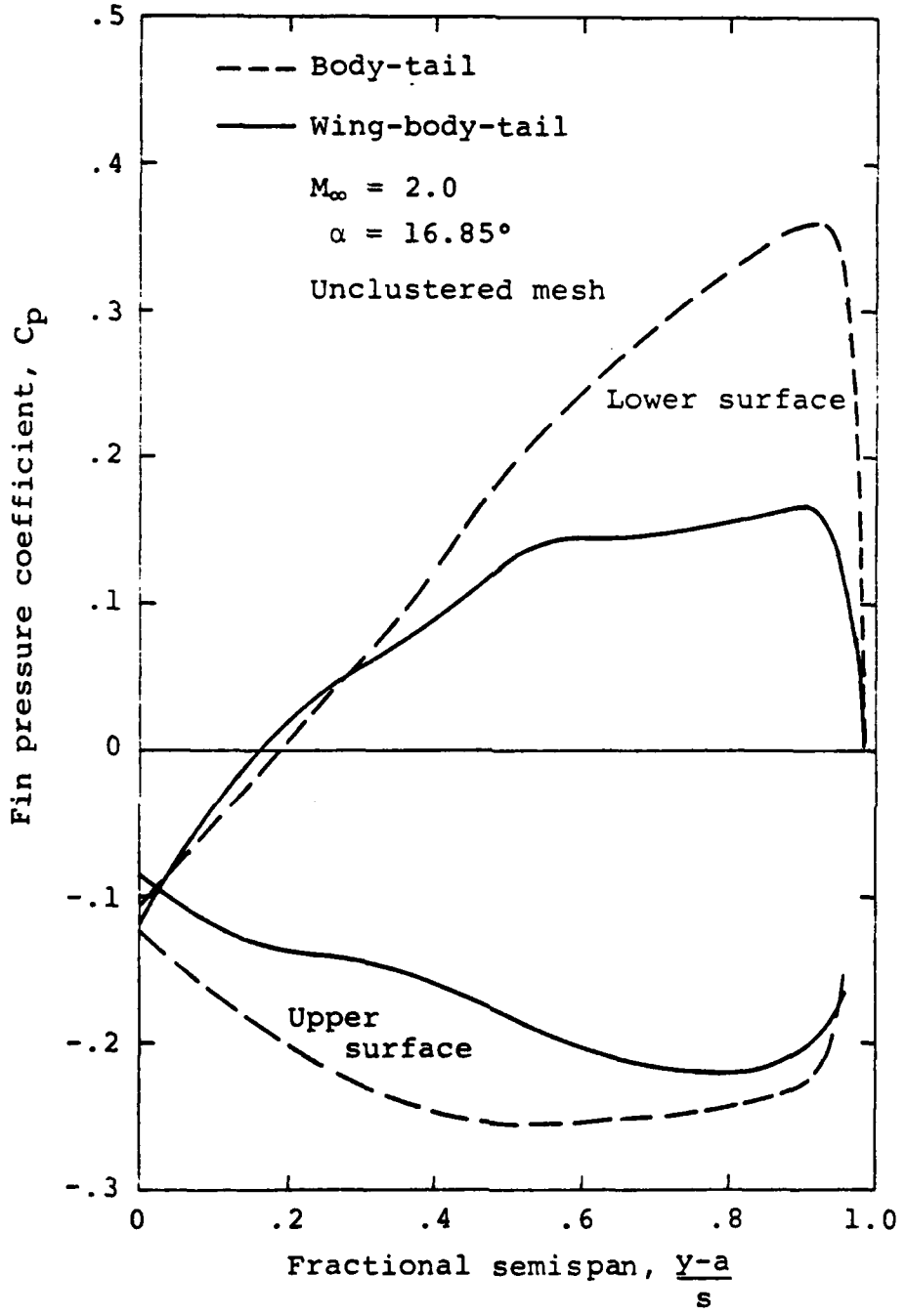

Figure 27.- Spanwise pressure distribution on upper and lower surface near midchord of interdigitated tail of body-wing and body-wing-tail as calculated by an Euler equation.

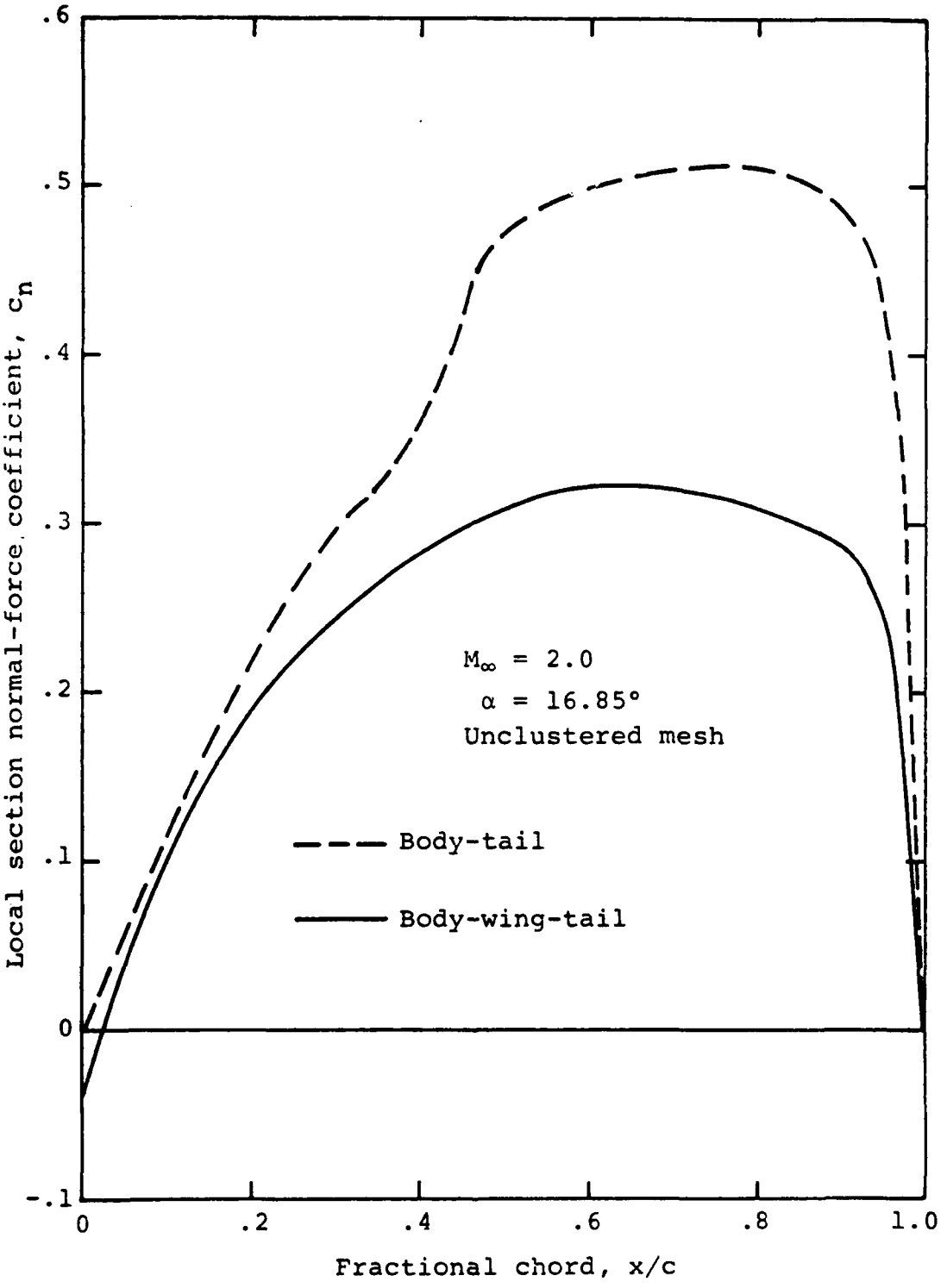

Figure 28.- Section normal-force coefficients (span loading) for upper fin of interdigitated tail for body-tail and body-wing-tail combinations as calculated by Euler code.

REFERENCES

1. Klopfer, G. H. and Nielsen, J. N.: Basic Studies of Wing-Body Interference at High Angles of Attack and Supersonic Speeds. ONR Report ONR-CR215-263-1, Oct. 1979.

2. Klopfer, G. H. and Nielsen, J. N.: Basic Studies of Body Vortices at High Angles of Attack and Supersonic Speeds. Nielsen Engineering & Research, Inc. TR 226, Oct. 1980 (work performed under ONR Contract N00014-780-C-0490).

3. Nielsen, J. N., Kuhn, G. D., and Klopfer, Goetz, H.: Euler Solutions of Supersonic Wing-Body Interference at High Incidence Including Vortex Effects. Nielsen Engineering & Research, Inc. TR 263, Aug. 1982.

4. Stallings, R. L., Jr. and Lamb, M.: Wing-Alone Aerodynamic Characteristics for High Angles of Attack at Supersonic Speed. NASA Technical Paper 1889, July 1981.

5. Dillenius, M. F. E. and Nielsen, J. N.: Computer Programs for Calculating Pressure Distributions Including Vortex Effects on Supersonic Monoplane or Cruciform Wing-Body-Tail Combinations with Round or Elliptical Bodies. NASA CR-3122, Apr. 1979.

6. Barnes, G. A. and Cronvich, L. L.: Bumblebee Program - Aerodynamic Data. Part I - Supersonic Flow Field, Pressure Fields, and Panel Load Data for Validation of Computational Methods. NASA CR-3114, Mar. 1979.

7. Barnes, G. A. and Cronvich, L. L.: Bumblebee Program - Aerodynamic Data. Part II - Flow Fields at Mach Number 2.0. NASA CR-3115, Apr. 1979.

8. Barnes, G. A. and Cronvich, L. L.: Bumblebee Program - Aerodynamic Data. Part III - Pressure Fields at Mach Numbers 1.5 and 2.0. NASA CR-3116, Apr. 1979.

9. Barnes, G. A. and Cronvich, L. L.: Bumblebee Program - Aerodynamic Data. Part IV - Wing Loads at Mach Numbers 1.5 and 2.0. NASA CR-3117, Apr. 1979.

10. Wardlaw, A. B., Jr., Solomon, J. M., and Baltakis, F. P.: Supersonic Inviscid Flow Field Computations of Missile Type Bodies. AIAA Paper No. 80-0271, presented at AIAA 18th Aerospace Sciences Meeting, Pasadena, CA, Jan. 1980.

11. Dillenius, M.F. E.: Program LRCDM2, Improved Aerodynamic Prediction Program for Supersonic Canard-Tail Missiles with Axisymmetric Bodies. Nielsen Engineering & Research, Inc. TR 287, Oct. 1983.

12. Glauert, H.: The Elements of Aerofoil and Airscrew Theory. Chpt. X, Cambridge University Press, 1943.

13. Landrum, E. J. and Babb, C. D.: Wind-Tunnel Force and Flow Visualization at Mach Numbers from 1.6 to 4.65 for a Series of Bodies of Revolution at Angles of Attack from -4° to 60°. NASA Tech. Memo. 78813, Mar. 1979.

14. Mello, J. F.: Investigation of Normal-Force Distributions and Wake Vortex Characteristics of Bodies of Revolution at Supersonic Speeds. Jour. of Aero. Sciences, Vol. 26, No. 3, Mar. 1959, pp. 155-168.

15. Ames Research Staff: Equations, Tables and Charts for Compressible Flow. NASA TR 1135, 1953.

16. Nielsen, J. N. and Smith, C. A.: Prediction of Aerodynamic Characteristics of Cruciform Missiles to High Angles of Attack Utilizing a Distributed Vortex Wake. Nielsen Engineering & Research, Inc. TR 208, 1979.

SYMBOLS

a	radius of cylindrical body
AR	wing aspect ratio
b	span of rectangular wing
c	chord of rectangular wing
c_n	two-dimensional normal-force coefficient; also section normal-force coefficient for a wing; also local normal-force coefficient in cross-sectional plane of body
C_{N_F}	normal-force coefficient of fin based on fin planform area
C_p	pressure coefficient, $(p - p_\infty)/q_\infty$
C_V	specific heat of air at constant volume
D	body diameter
K	constant of proportionality, Eq. (7)
M	Mach number
M_l	local Mach number
M_∞	free-stream Mach number
N	normal force
p	static pressure
p_l	local static pressure
p_∞	free-stream static pressure
p_n	new value of p, Eq. (1)
p_p	predicted value of p, Eq. (1)
p_t	total pressure
p_{t_l}	local total pressure

p_{t_∞}	free-stream total pressure
q	dynamic pressure
q_l	local dynamic pressure
q_∞	free-stream dynamic pressure
r	radial distance from axis of body
r_r	value of r at body bow wave
R, ϕ	polar coordinate system, Figure 10
R_G	gas constant for air
s	exposed semispan of a wing or a fin
S	entropy of air
T_t	total temperature
u_n, v_n, w_n	velocity components at mode n, Eq. (2)
U,V,W	velocity components in ϕ, R, and Z directions, respectively, Fig. 10
V_t	fluid velocity at wing tip
V_∞	free-stream velocity
x,y	coordinates in chord plane of rectangular wing, x measured positive downstream from leading edge and y measured from root chord positive to right facing upstream
X,Y,Z	coordinates used in Euler calculations for rectangular wing, Figure 10
S_F	planform area of fin
S_R	reference entropy of air
α	angle of attack
α_f	flow angle normal to radius vector, positive upward, referenced to body axial direction, Figure 10

β_f	flow angle along radial direction referenced to axial direction, Figure 10
γ	ratio of specific heats for air
θ_n	flow angle at node n interpolated between the leading-edge angle and the flow angle at node n-1
λ	wing taper ratio
ρ_n, ρ_p	new and predicted value of ρ in Eq. (1)
ϕ	polar angle in R,ϕ polar system, Figure 10
ϕ_{s_1}	angular position of primary separation angle on cone or cylinder measured from plane of windward meridian
ξ_u	$(r-a)/(r_s-a)$, radial spacing parameter for unclustered mesh
ξ_c	radial spacing parameter for clustered mesh

END

FILMED

1-84

DTIC